

VERY LOW FREQUENCY RADIO SIGNATURES OF
TRANSIENT LUMINOUS EVENTS ABOVE THUNDERSTORMS

A DISSERTATION
SUBMITTED TO THE DEPARTMENT OF ELECTRICAL ENGINEERING
AND THE COMMITTEE ON GRADUATE STUDIES
OF STANFORD UNIVERSITY
IN PARTIAL FULFILLMENT OF THE REQUIREMENTS
FOR THE DEGREE OF
DOCTOR OF PHILOSOPHY

Robert Andrew Marshall

May 2009

© Copyright by Robert Andrew Marshall 2009
All Rights Reserved

I certify that I have read this dissertation and that, in my opinion, it is fully adequate in scope and quality as a dissertation for the degree of Doctor of Philosophy.

(Umran S. Inan) Principal Adviser

I certify that I have read this dissertation and that, in my opinion, it is fully adequate in scope and quality as a dissertation for the degree of Doctor of Philosophy.

(Victor P. Pasko
The Pennsylvania State University)

I certify that I have read this dissertation and that, in my opinion, it is fully adequate in scope and quality as a dissertation for the degree of Doctor of Philosophy.

(Jelena Vučković)

Approved for the University Committee on Graduate Studies.

*This dissertation is dedicated to my parents,
Who inspired me to become a doctor
(sort of).*

Abstract

Lightning discharges emit intense optical and acoustic energy, in the form of lightning and thunder, respectively, but a large amount of energy is emitted as radio-frequency electromagnetic pulses (EMP). These pulses can be detected thousands of kilometers away, thanks to efficient propagation in the waveguide formed by the conducting Earth and the overlying ionosphere. In addition, intense discharges interact with the overlying ionosphere at 80-100 km altitude. The EMP-ionosphere interaction is directly observed in one manifestation as the bright transient optical emissions known as “elves”, but in addition, the interaction can directly modify the free electron density in the nighttime lower ionosphere.

Modifications of the ionospheric electron density can be detected via subionospheric Very Low Frequency (VLF) remote sensing. In this method, coherent signals from powerful VLF transmitters, built for submarine communication and operated by the Navy, are monitored and their amplitude and phase are tracked in time. The variations of these signals are used to sense ionospheric modifications through rapid changes in the received amplitude and/or phase when the transmitted signal propagates through an ionospheric perturbation. When these perturbations are caused by lightning, they are known as “Early VLF” perturbations, due to the negligible delay between the lightning discharge and the appearance of the VLF signal change, whereas lightning-induced electron precipitation (LEP) events have a delay of 1–2 seconds.

In this work, correlations between VLF signatures and optical events are used to show that these Early VLF events may be the signature of ionospheric modification by in-cloud (IC) lightning discharges. While the more impressive cloud-to-ground

(CG) lightning discharges are more commonly observed and better understood, they are outnumbered in occurrence 3:1 by IC discharges, whose effects may be relatively stronger in the overlying ionosphere. We use a 3D time-domain model of the lightning EMP-ionosphere interaction to calculate expected ionospheric density changes from IC discharges. We find that bursts of IC-EMPs can significantly modify the lower ionosphere, with both increases and decreases in electron density. We then use a frequency-domain model of the VLF transmitter signal propagation in the Earth-ionosphere waveguide to a VLF receiver to show that these density changes are consistent with measurements. Our results demonstrate that these Early VLF events, which are ubiquitous in VLF data, are signatures of the effects of in-cloud lightning, and that they can be used to quantify the effects of IC lightning on the ionosphere during an intense thunderstorm.

Acknowledgements

First and foremost, I am forever indebted to my principal advisor, Professor Umran Inan. Umran has been a devoted mentor and motivator, and has provided seemingly endless support and research opportunities. Thanks to Umran, I have been lucky enough to do field work on all seven continents, design and build instruments, analyze data, and dabble a little in modeling.

I feel very privileged to have Professor Victor Pasko serve as my second advisor. Apart from being a great friend, Victor has also been an unlimited source of knowledge and advice. He enthusiastically came out to Stanford from Pennsylvania to serve on my defense committee, as well as serving as a reader of this dissertation.

I want to thank Professor Jelena Vučković for serving on both my defense committee and my reading committee, and Professor Ron Hanson in Mechanical Engineering for serving as the Chair on my defense committee.

The VLF Group at Stanford has been a constant source of support over the years. Whether it be a question of modeling, fixing a computer, designing a circuit, or figuring out how to make it waterproof, there's always someone in the group who knows the answer. I would especially like to acknowledge Dr. Tim Chevalier; in addition to being the architect of the frequency-domain model in Chapter 4, Tim essentially taught me the time-domain method and helped to get the model in Chapter 3 working. I am further grateful to Drs. Maria Spasojevic and Nikolai Lehtinen, whose expertise and advice on a variety of topics have helped shape my research.

The students in the VLF group have provided everything from motivation, commiseration over failures, celebration of successes, coffee breaks, political discussions, and other forms of procrastination. I especially want to thank Dr. Marek Gołkowski,

Dr. Praj Kulkarni, Ryan Said, Ben Cotts, Morris Cohen, and in particular Robert Newsome, whose skills in software development probably saved me years of work. I would also like to thank Shaolan Min and Helen Niu, Dan Musetescu and Jeff Chang for the many ways that they make our jobs as students much easier.

I am grateful to many of the former students of the VLF Group, in particular Dr. Elizabeth Kendall, my mentor in the early years, and Dr. Slava Glukhov, the original author of the time-domain model. I have also been lucky to have had assistance from a wide variety of collaborators; in particular I want to thank Dr. Francois Lefeuvre (LPCE-CNRS, Orléans, France), Profs. Hans Stenbaek-Nielsen and Dave Sentman (University of Alaska, Fairbanks), Dr. Geoff McHarg (U.S. Air Force Academy, Colorado Springs, CO), Drs. Torsten Neubert and Olivier Chanrion (Danish National Space Center, Copenhagen, Denmark), Dr. Agnes Mika and Prof. Christos Haldoupis (University of Crete), Dr. Walter Lyons (FMA Research, Fort Collins, CO), and Prof. Yukihiro Takahashi (Tohoku University, Sendai, Japan).

I want to thank the Stanford Triathlon Team, who over the past four years have been a fantastic group of friends, and have shown me that there are things in life more painful than doing a Ph.D.

Last but most certainly not least, I want to thank my unbelievably supportive family – my parents, my sister Kathleen, and my brothers Pete and Tom, who are always good for an Ironman or a 1000 mile bike ride on short notice.

Robert Andrew Marshall

Stanford, CA

May 22, 2009

This work has been supported at various times by a Texas Instruments Stanford Graduate Fellowship; Office of Naval Research Grant N00014-03-1-0333; National Science Foundation Grant ATM-0551174; and by a Stanford Lieberman Fellowship.

Contents

Abstract	v
Acknowledgements	vii
1 Introduction	1
1.1 The Terrestrial Ionosphere	2
1.2 Lightning	3
1.3 The Earth-Ionosphere Waveguide	6
1.4 Transient Luminous Events	9
1.5 VLF Signatures of Lightning	13
1.6 Early VLF Perturbations	17
1.7 Scientific Contributions	21
2 Sprites, Early VLF Events, and Sferic Bursts	24
2.1 History of Early VLF Research	25
2.2 Sprites and Early VLF	29
2.2.1 Case Studies	31
2.2.2 Discussion and Interpretation	41
2.2.3 Summary	47
2.3 Sprites and Sferic Bursts	48
2.3.1 Description of the VLF Data	49
2.3.2 Results: Sprite Correlations	50
2.3.3 In-cloud sources of VLF bursts	54
2.3.4 Summary	63

2.4	Sferic Bursts and Early VLF	65
2.5	Early VLF Caused by In-cloud EMP pulses	66
3	Modeling the Lightning EMP	69
3.1	Previous Work	69
3.2	The 3D EMP Model	70
3.2.1	Update Equations	72
3.2.2	Collision Frequency	74
3.2.3	Ionization and Attachment	76
3.2.4	Optical Emissions	80
3.2.5	Determination of IC Amplitudes	82
3.3	Results	85
3.3.1	Single Vertical Discharge	85
3.3.2	Horizontal Discharge	91
3.3.3	Parameter Variations for Horizontal Discharges	94
3.3.4	Repeated Pulses	104
3.4	Summary	107
4	Modeling the VLF Transmitter Signal	109
4.1	VLF Wave Propagation in the Earth-Ionosphere Waveguide	109
4.2	Previous Work	112
4.3	The FDFD Propagation Model	113
4.3.1	Simulation of Ionospheric Disturbances	118
4.4	Simulation Results	121
4.4.1	Perturbations from a Single CG Discharge	121
4.4.2	Effects of Perturbation Location	122
4.4.3	Effects of Transmitter Frequency	126
4.4.4	Perturbations from Sequences of IC discharges	128
4.5	Discussion and Conclusions	133
4.5.1	Polarity of Early VLF Events	133

5	Summary and Suggestions for Future Research	136
5.1	Summary of Results	136
5.2	Suggestions for Future Research	138
5.2.1	Improving the EMP model	138
5.2.2	Use of the EMP Model for Transionospheric Propagation	141
5.2.3	Early VLF and TLEs with Photometric Imaging	142
A	EMP Model Formulation	143
A.1	Input Fields	143
A.2	Magnetic field Update Equations	145
A.3	Collision Frequency	145
A.4	Current J Update Equations	147
A.5	Ionization and Attachment	150
A.6	Electric field Update Equations	151

List of Tables

1.1	Typical parameters for cloud-to-ground lightning discharges	4
1.2	List of VLF transmitters	18
2.1	Sprite / VLF data for July 2000	40
3.1	Optical coefficients	82

List of Figures

1.1	Typical ionospheric electron density and neutral density profiles	3
1.2	Example of spider lightning	6
1.3	Sketch of the Earth-ionosphere waveguide system	7
1.4	Ionospheric reflection: frequency versus altitude	9
1.5	Example sprites and quasi-electrostatic field	11
1.6	Some example elves	12
1.7	Some example jets	14
1.8	Example sferic in time series and spectrogram	16
1.9	VLF transmitters and Stanford VLF receivers	19
1.10	Summary of ionospheric effects of lightning	23
2.1	Map of transmitter paths and VLF data from 15 July 1995	32
2.2	Zoomed-in view of six early/fast events from 1995	34
2.3	Map of HAIL array and 18 August 1999 lightning activity	36
2.4	VLF Narrowband data from 18 August 1999	37
2.5	Zoomed-in view of one prominent early/fast event from 1999	38
2.6	Histogram of 1999 early/fast perturbation amplitudes	39
2.7	Map of HAIL array and lightning activity for 22 July 2000	41
2.8	VLF Narrowband data from 22 July 2000	42
2.9	Large sprites observed on 02 July 2000	42
2.10	Sprite Brightness versus VLF perturbation amplitude	45
2.11	Examples of sprite/halo/VLF combinations	46
2.12	Distributions of peak currents and distances to the receiver for NLDN data	51

2.13	Examples of sferic bursts	52
2.14	Distributions of sferic and burst energy for each year	53
2.15	Distributions of sferic bursts durations	54
2.16	Example of VLF, NLDN and LMA data together for a sprite case	58
2.17	A second example of VLF, NLDN and LMA data together for a sprite case	59
2.18	Cross-correlations between VLF burst data and LMA data	60
2.19	An example of LMA and VLF burst data demonstrating the tendrils in in-cloud lightning	61
2.20	Sferic burst average power versus burst duration	62
2.21	Peak currents versus sferic and sferic burst energy	64
2.22	Correlations between Early/fast events and sferic bursts	66
2.23	Summary of correlations between sprites, Early VLF events, and sferic bursts	67
3.1	Simulation space used in the EMP model	73
3.2	Typical ionospheric electron density and neutral density profiles.	75
3.3	Electron mobility in air as a function of reduced electric field	77
3.4	Ionization and attachment rates in air	79
3.5	Optical excitation rates used in this work	81
3.6	Measurement of relative sferic and burst amplitudes	83
3.7	Histogram of E_{100} values from NLDN, and ratios of sferic-to-burst amplitudes.	84
3.8	Simulated sferics received 600–1000 km away	86
3.9	Electric field amplitudes of input vertical and horizontal pulses	87
3.10	Example simulation of an elve from a vertical discharge	89
3.11	Simulation of elves from vertical discharges, varying amplitude	90
3.12	Results for 7 V-m^{-1} horizontal discharge at 5 km altitude	92
3.13	Amplitude variation for horizontal discharges at 5 km altitude	93
3.14	N_2 1P to 2P intensity ratios for vertical and horizontal discharges	95
3.15	Effect of variation in the dipole altitude: Analytical calculations	97

3.16	Simulation results for horizontal dipoles of $7 \text{ V}\cdot\text{m}^{-1}$ amplitude located at 1–8 km altitude	98
3.17	Variation with the ionospheric density profile	100
3.18	Variation in horizontal dipole orientation angle	101
3.19	Variation in magnetic field dip angle	103
3.20	Effects of multiple pulses on the ionosphere	105
3.21	Parameters of pulses for random sequence in Figure 3.20	106
4.1	Sketch of the VLF propagation model	116
4.2	Example field outputs from FDFD model	117
4.3	Example perturbation result from the propagation model	119
4.4	VLF propagation simulation with CG inputs	123
4.5	Effect of perturbation location on received amplitude	125
4.6	FDFD simulations for varied transmitter frequencies	127
4.7	Effect of transmitter frequency on received amplitude	129
4.8	VLF propagation simulation with EMP multi-pulse inputs	131
4.9	VLF propagation simulation with EMP multi-pulse inputs; realistic HAIL path	132
4.10	Histogram of dB perturbation amplitudes of early VLF events	135
5.1	Electric Field magnitude snapshot from the EMP model	139

Chapter 1

Introduction

This work describes the interaction of the lightning electromagnetic pulse (EMP) with the Earth's lower nighttime ionosphere. In addition to bright optical emissions in the discharge channel (lightning) and strong shock and acoustic waves (thunder), lightning discharges emit intense radio waves, from a few Hz in frequency all the way up to about 10 GHz [*Rakov and Uman, 2003*, p. 6]. The peak of this radiation is in the 5–10 kHz range, in the Very-Low-Frequency (VLF) band of the electromagnetic spectrum.

VLF frequencies propagate efficiently over great distances in the Earth-ionosphere waveguide; for this reason, VLF signatures of lightning can be observed at locations thousands of kilometers distant, in many cases all the way around the globe. While most of the radio energy of lightning propagates in this way to great distances, some of the energy is deposited directly above the discharge in the lower ionosphere. The ionosphere is the region of the Earth's upper atmosphere from 60 km to 1000 km in altitude, characterized by appreciable densities of free electrons and ions. This free ionization is created by incident solar radiation and cosmic rays; for this reason, the ionosphere is considerably more dense in daytime, as shown in Figure 1.1. The portion of the lightning energy deposited in the lower ionosphere (60–100 km) causes intense transient optical emissions known as sprites and elves, as well as electron heating and generation of new ionization, which is the primary topic of this thesis.

This chapter introduces the Earth’s ionosphere in Section 1.1, and some important properties of lightning in Section 1.2. VLF propagation in the Earth-ionosphere waveguide is discussed in Section 1.3. In Section 1.4, so-called Transient Luminous Events (TLEs), i.e., the optical signatures of lightning that occur at high altitudes above the thundercloud, are introduced. In Section 1.5 VLF signatures of lightning known as “sferics” are discussed, and Section 1.6 describes narrowband VLF transmitters and Early VLF perturbations, which are the primary subject of this work.

1.1 The Terrestrial Ionosphere

Solar radiation incident on the Earth’s atmosphere causes photoionization of neutral molecules and leads to layers of appreciable electron and ion densities. This occurs at altitudes where the air is thin enough so that the rate of new ionization exceeds the rate of loss of ionization through recombination and attachment. These layers collectively make up what is known as the ionosphere, which is typically broken up into the *D*- (60–100 km altitude), *E*- (100–150 km), and *F*-regions (150–400 km) as well as the topside (400–1000 km) ionosphere, demarcated where obvious changes in the electron density profile occur. This work is primarily concerned with the *D*-region ionosphere, where the majority of lightning energy is deposited, leading to significant ionospheric modification. The lower ionosphere is a weakly ionized (i.e., N_e , the electron density, is much less than N , the neutral density), collisional (i.e., significant electron–neutral collisions occur), and cold (electron temperature $T_e \ll 1$ eV) plasma.

Figure 1.1 shows typical day and night electron density as a function of altitude, along with neutral densities for the primary constituents of the atmosphere. Below 120 km, the neutral atmosphere is about 79% N_2 , 20% O_2 , and 1% Argon, with small amounts of Helium. Above 120 km, photo-dissociation of O_2 leads to an increase in atomic oxygen (O), which becomes the dominant neutral species above 200 km. The electron density is orders of magnitude lower than the neutral density below 120 km; above 120 km during the day (or 180 km at night), the ionosphere becomes strongly ionized. While not shown here, the ionosphere also contains a wide variety of positive

and negative ions, including N_2^+ , O_2^+ , O^- , and many others. Collisions occur between electrons and neutrals with an effective frequency ν_e (s^{-1}). In the lower ionosphere where $N_e \ll N$, electron–electron collisions can be ignored, and the electron–neutral collision frequency ν_e is primarily controlled by the neutral density N (as shown in Section 3.2.2, it increases in the presence of an applied electric field).

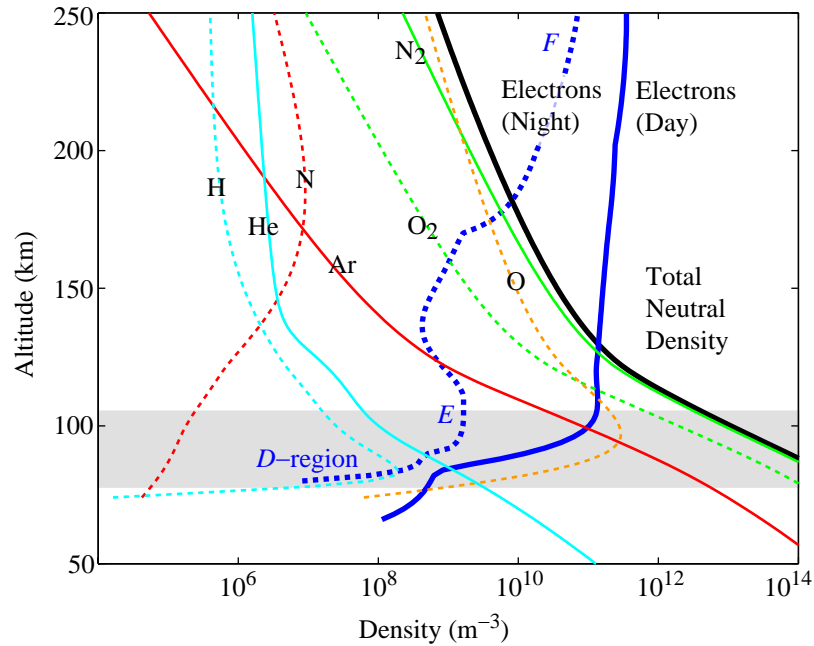


Figure 1.1: Typical ionospheric electron density and neutral density profiles. The gray swath marks the altitudes of greatest interest in this work. Neutral density curves generated from the MSIS-E-90 Atmospheric Model; electron densities from the IRI-2007 Model, both available at <http://omniweb.gsfc.nasa.gov>.

1.2 Lightning

Lightning discharges are manifested in three main varieties. Negative cloud-to-ground ($-CG$) lightning, which makes up about 90% of cloud-to-ground (CG) strokes [Rakov and Uman, 2003, p. 4], moves negative charge from the cloud to the ground, as the name suggests. Positive cloud-to-ground ($+CG$) lightning is thus said to move positive charge from the cloud to the ground (although in reality, it is negatively

Table 1.1: Typical parameters for cloud-to-ground lightning discharges, summarized from Chapters 4 and 5 of *Rakov and Uman* [2003]. The 5%, 50% and 95% columns represent percentile values.

Parameter	−CG			+CG		
	5%	50%	95%	5%	50%	95%
1st stroke Peak Current (kA)	14	30	80	4.6	35	250
1st stroke Total Charge (C)	1.1	5.2	24	20	80	350
1st stroke Duration (μ s)	30	75	200	25	230	2000
Interstroke interval (ms)	7	33	150		102	
Flash Duration (ms)	0.15	13	1100	14	85	500
Strokes per flash (multiplicity)	1		25		1	

charged electrons which move from the ground to the cloud). The third category, in-cloud lightning (sometimes referred to as cloud discharges), refers to those lightning flashes that never reach the ground. It is estimated that lightning strikes on average around the globe about 40 times per second [*Christian et al.*, 2003]; in terms of flashes to ground, this flash rate implies that any given square kilometer area of the Earth’s surface is hit, on average, 1.5 times per year. Of course, the rate is much higher in certain areas (i.e., the Congo basin, with a rate of ~ 80 per km^2 per year), while other areas have almost zero lightning activity (i.e., Antarctica).

Disparity exists not only between the rates of the different types of lightning, but also with the magnitudes, durations, and multiplicity of these discharges. The most common −CG strokes have peak currents of 10–100 kA, with a median of 30 kA, and durations (the time from when the pulse exceeds 2 kA to half its peak on the tail) of 30–200 μ s, with a median of 75 μ s [*Berger et al.*, 1975]. Negative CGs also far more commonly (about 80% of the time) have a multiplicity greater than 1; that is, more than one “stroke” in a “flash”. *Rakov and Uman* [1990] and *Kitagawa et al.* [1962] report −CG flashes with anywhere from 1–25 strokes. +CGs, on the other hand, have peak currents from 5 to 300 kA, with a median of 35 kA; durations of 25 μ s to 2 ms, with a median of 230 μ s [*Berger et al.*, 1975]; and multiplicity of 1 for over 99% of flashes [*Lyons et al.*, 1998]. These and other important characteristics of +CG and −CG lightning are summarized in Table 1.1.

The third category of lightning, in-cloud lightning, occurs about 3 times more

frequently than the total of CG strokes, and itself contains a great variety, including intracloud, intercloud or cloud-to-cloud, and cloud-to-air discharges [*Rakov and Uman, 2003*, p. 321]. The common acronym “IC lightning” is typically used to refer to intracloud discharges, but in this work it is used to refer to all forms of in-cloud lightning flashes.

IC lightning is relatively less understood than CG lightning, because i) photography of IC channels is more difficult due to the presence of the cloud, ii) currents and charges cannot be measured directly as they can on the ground, and iii) there is a relative lack of interest, on account of their insignificance to ground objects and humans [*Rakov and Uman, 2003*, p. 321]. Nonetheless, a great amount of research has led to a better understanding of IC discharges and some measurements of their characteristics. Typically, the measured parameters are for the stepped leaders within IC flashes. These pulses occur at altitudes from 1 to 12 km, with thousands to millions of pulses per second, and each pulse is about 60–300 m in length [*Proctor, 1997*].

The in-cloud lightning above refers only to those flashes that never reach the ground; however, in many cases CG flashes contain large components of in-cloud activity. When these combined flashes are visually extensive they are referred to as “spider lightning”, as shown in Figure 1.2. The extensive in-cloud channels connected to the main CG discharge serve to tap the thundercloud of charge, providing continuing current to the ground and increasing the total charge removal.

In the past decade, understanding of IC lightning has grown with the development of Lightning Mapping Arrays (LMAs) [i.e., *Thomas et al., 2000*]. These are arrays of VHF receivers capable of locating individual pulses in 3-dimensional space and time. By measuring the arrival time of individual pulses at four or more receivers, the 3D location (and time) can be inferred from a solution of 4 equations with 4 unknowns. Usually, six or more receivers are used for redundancy and to give a measure of uncertainty. By locating each constituent pulse in a developing flash, LMAs can provide a full 3D “map” of the evolution of the flash in time and space. LMA data and related examples are discussed further in Section 2.3.



Figure 1.2: Example of spider lightning; used with permission from Tom Warner, <http://www.atmosphericwildlife.com/chases/2002/020624.htm>.

1.3 The Earth-Ionosphere Waveguide

As mentioned above, lightning radiation is strongest at frequencies around 5–10 kHz, in the VLF range. These frequencies propagate particularly well over long distances along the Earth’s surface, due to the waveguiding effect of the lower ionosphere. In essence, the conducting Earth’s surface and the conducting lower ionosphere form a waveguide of about 70–85 km thickness over the entire surface of the Earth. Treating it as a perfectly-conducting parallel plate waveguide with cutoff frequencies [Inan and Inan, 2000, p. 264] of $f_{c_m} = mv_p/2a$, where v_p is the phase velocity of light, m is the mode order for both Transverse Electric (TE) and Transverse Magnetic (TM) modes, and a is the 70–85 km waveguide thickness, cutoff frequencies are found to be multiples of about 1700–2100 Hz.

In reality, the ionosphere is anisotropic, frequency-dependent, and highly variable, and neither the ionosphere nor the ground are perfect conductors. For a given electron density N_e , collision frequency ν_e (related to the neutral density N), and magnetic field amplitude B_0 , the complex index of refraction for VLF waves is described by the

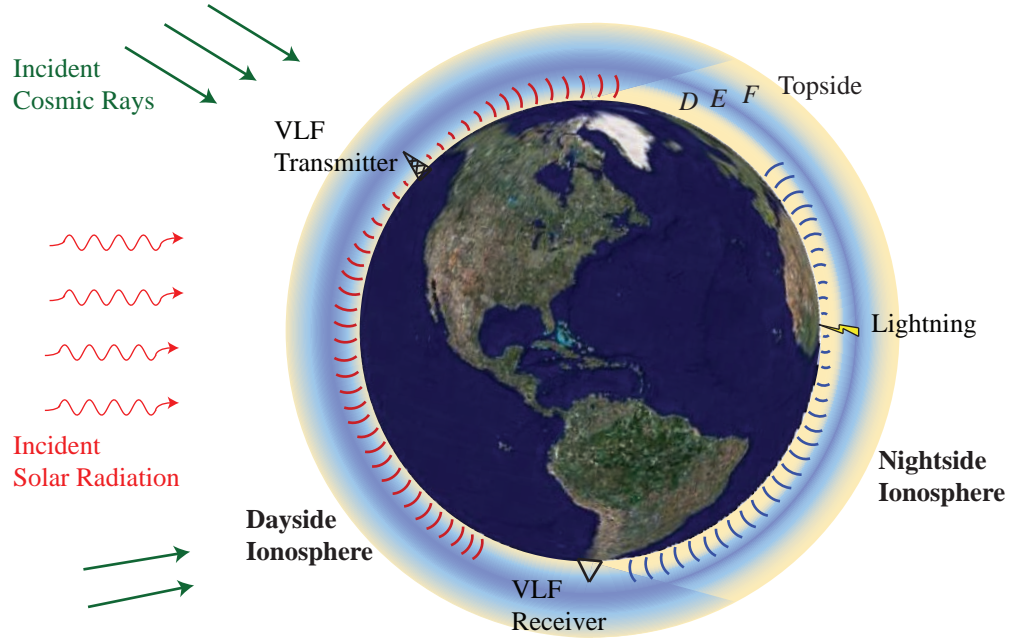


Figure 1.3: Sketch of the Earth-Ionosphere Waveguide system. The ionosphere is created by incident solar radiation and cosmic rays, and hence is more dense in those regions illuminated by the sun. VLF emissions from lightning and transmitters propagate around the globe in the waveguide. Note that the thickness of the ionosphere is exaggerated here; typically the F-region ionosphere extends to about 300 km, still only 1/20th the radius of the Earth.

Appleton-Hartree Equation [e.g., [Ratcliffe, 1959](#), p. 19]:

$$n^2 = 1 - \frac{X}{1 - iZ - \left(\frac{Y^2 \sin^2 \theta}{2(1 - X - iZ)} \right) \pm \sqrt{\frac{Y^4 \sin^4 \theta}{4(1 - X - iZ)^2} + Y^2 \cos^2 \theta}} \quad (1.1)$$

where

$$X = \frac{\omega_p^2}{\omega^2} \quad \text{and} \quad \omega_p^2 = \frac{q_e^2 N_e}{m_e \epsilon_0} \quad (1.2)$$

$$Y = \frac{\omega_b}{\omega} \quad \text{and} \quad \omega_b = \frac{q_e B_0}{m_e} \quad (1.3)$$

$$Z = \frac{\nu_e}{\omega} \quad (1.4)$$

where ω_p is the electron plasma frequency with an electron density N_e ; ω_b is the electron gyrofrequency about a static magnetic field of intensity B_0 ; and ν_e is the effective electron collision frequency. The above equations consider electrons only; a more general version of the Appleton-Hartree Equation includes effects of ions. The appearance of electron-neutral collisions through ν_e leads to a complex index of refraction and thus absorption (or attenuation) of the VLF wave. In a non-collisional, non-magnetized plasma, $n^2 = 1 - \omega_p^2/\omega^2$, and waves reflect at frequencies below the plasma frequency ω_p , where the index of refraction is imaginary. In the D -region ionosphere at 90 km with $N_e \simeq 10^2 \text{ cm}^{-3}$, this would occur for all frequencies below about 300 kHz. However, the presence of collisions prevents the index of refraction from going to zero, and lowers the frequency of reflection. Ignoring the contribution of the magnetic field (i.e., $Y = 0$), when $\nu_e \gg \omega$, the index of refraction reduces to

$$n^2 \simeq 1 - \frac{X}{iZ} \quad (1.5)$$

[[Ratcliffe, 1959](#), p. 110] shows that under those conditions reflection occurs when $X = Z$, i.e., when the real and imaginary parts of n are equal, or where $\omega = \omega_p^2/\nu_e$. For frequencies in the VLF range from ~ 100 Hz to 30 kHz, this condition occurs at altitudes of ~ 80 – 85 km, as shown in [Figure 1.4](#).

The Earth-ionosphere waveguide further deviates from the parallel-plate model due to the curvature of the Earth and the anisotropy of the ionosphere, caused by the presence of the Earth's magnetic field. These two factors lead to propagating modes that are not purely TE, TM, or TEM (the zero-order mode), but which rather have small components in the direction of propagation. For this reason, modes in the Earth-ionosphere waveguide are typically referred to as Quasi-TEM (QTEM), QTE, and QTM [[Budden, 1961](#), p. 151]. Further discussion of wave propagation in the Earth-ionosphere waveguide is provided in [Section 4.1](#).

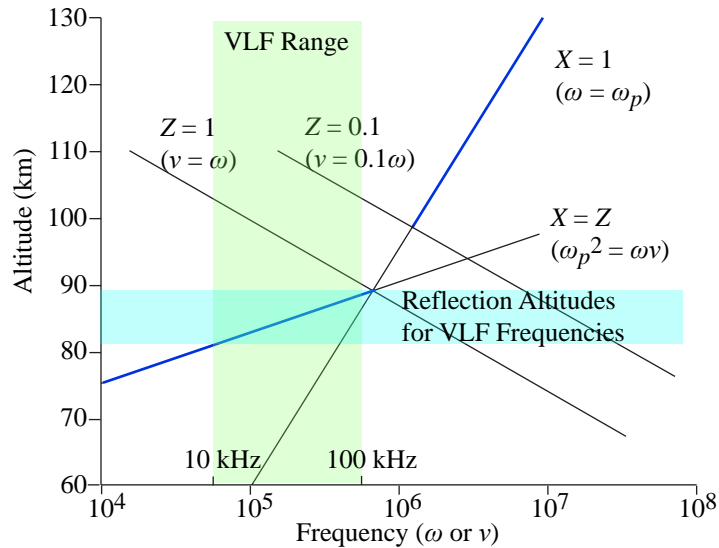


Figure 1.4: Altitudes of ionospheric reflection based on wave frequency; adapted from [Ratcliffe, 1959, p. 110]. The green swath roughly covers the VLF frequency range used by VLF transmitters; the intersecting blue swath shows the corresponding reflection altitudes where $X = Z$.

1.4 Transient Luminous Events

In only the last 20 years, a number of direct effects of lightning on the overlying ionosphere have been discovered and studied extensively. Many of these events have been discovered optically, and the overall class has recently been termed “Transient Luminous Events” or TLEs, of which the most prominent examples are the so-called sprites, elves, blue jets, and gigantic jets.

In 1989, the first serendipitous recording was made of a large optical flash between the top of the thundercloud and the ionosphere [Franz *et al.*, 1990]. These events, known as sprites [Sentman *et al.*, 1995], are the signature of heating and electrical breakdown in the upper atmosphere, due to the intense electric field produced at high altitudes by the removal of charge in CG discharges. Figure 1.5 shows two example sprites and the electric field structure above a thundercloud following an intense cloud-to-ground discharge. Sprites are typically initiated around 75 km altitude, where the electrostatic field crosses the threshold for conventional breakdown. They can have spatial extents anywhere from 10–50 km vertically, in the

altitude range from 40–90 km, and up to 50 km laterally. They are almost always associated with positive cloud-to-ground (+CG) discharges [Lyons, 1995; Sentman *et al.*, 1995; Lyons, 1996], typically those with large charge moments [Cummer and Inan, 2000; Lyons *et al.*, 2003; Cummer and Lyons, 2005]. Since the first recording, sprites have been observed from the Space Shuttle [Boeck *et al.*, 1992; Yair *et al.*, 2004], from satellites [e.g., Mende *et al.*, 2005a], and extensively from the ground [e.g., Sentman *et al.*, 1995; Lyons, 1996]. These bright, primarily red flashes last only a few milliseconds [Marshall and Inan, 2006]. Recent high-speed video measurements have indicated that the predominant features of sprites are downward and upward-propagating streamer discharges [Stanley *et al.*, 1999; Cummer *et al.*, 2006; McHarg *et al.*, 2007]. Sprites are often observed with associated diffuse optical regions at their upper altitudes (85–90 km), termed “sprite halos”; however, sprite halos can also occur without an associated sprite.

Sprites are the signature of the quasi-electrostatic (QE) field causing heating and ionization in the upper atmosphere, as shown in Figure 1.5. The intensity of the lightning-induced quasi-electrostatic field is directly related to the quantity Q and the altitude h of the charge removed from the cloud by lightning, and hence the charge moment $M_q = Qh$ of a causative lightning discharge is thought to be the dominant factor in sprite initiation [Pasko *et al.*, 1997]. This QE field is “electrostatic” in that it is due to the charge removed from the thundercloud by a CG, but is “static” only on time scales of a few milliseconds to seconds, varying with altitude. Sprites have also been exclusively (except for a handful of cases) associated with +CG lightning [Williams, 1998]; this is almost certainly due to the fact that +CG discharges are far more commonly followed by long continuing currents of up to hundreds of ms [Rust *et al.*, 1981, 1985; Beasley *et al.*, 1983], resulting in charge removal in +CG of 20–350 C (median of 80 C) compared to 1–25 C (median 5 C) for –CGs [Berger *et al.*, 1975].

Shortly following the discovery of sprites, a prediction was made that the electromagnetic pulse from lightning could cause optical emissions in the lower ionosphere [Inan *et al.*, 1991], which would later come to be known as “elves” (singularly known as an “elven”, to avoid confusion with the ELF frequency range). In addition to optical emissions, these electromagnetic pulses (EMPs) may cause appreciable changes in the

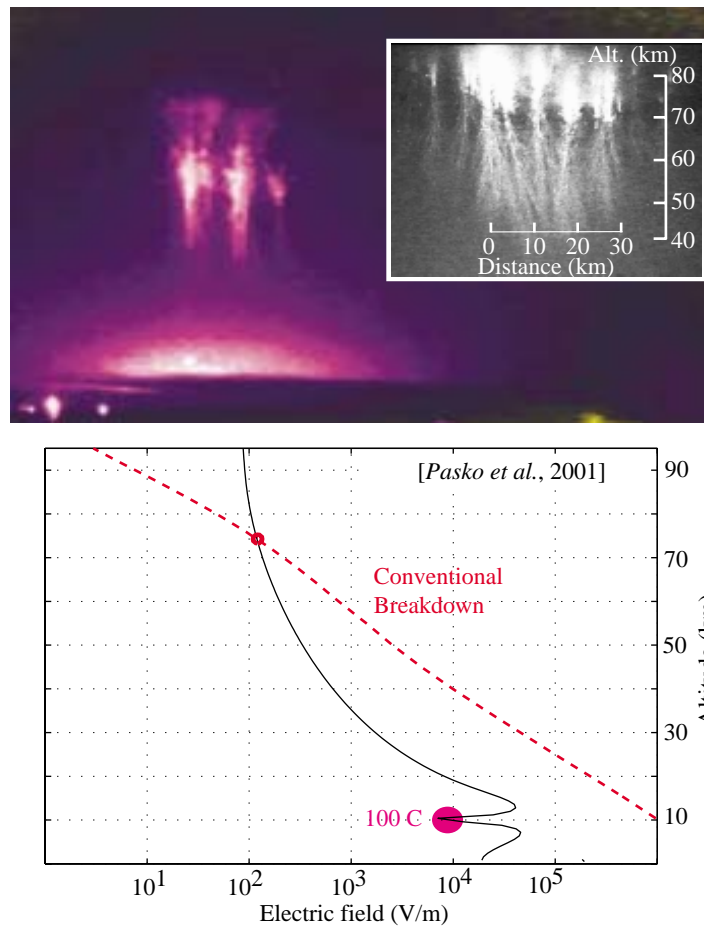


Figure 1.5: Top: two examples of sprites. The left image is false-colored from black-and-white. Bottom: the quasi-electrostatic field structure that leads to sprite initiation [Pasko *et al.*, 2001].

local ionospheric electron density, through impact ionization and dissociative attachment of heated electrons. These effects are discussed in great detail in Chapter 3. Elves were first observed from the Space Shuttle as an “airglow brightening” [Boeck *et al.*, 1992], and the first targeted observations from the ground were made by Fukushima *et al.* [1996]. Measurements with high-speed sensitive photometric instruments have confirmed the expected geometry of elves [Inan *et al.*, 1997], with a signature “doughnut hole” and rapidly expanding ring structure due to the radiation pattern of a cloud-to-ground discharge (Barrington-Leigh *et al.* [2001] and references therein).

Recently, the ISUAL experiment onboard the FORMOSAT-2 satellite [Chern *et al.*, 2003] became the first satellite instrument dedicated to observations of TLEs from space. This experiment has shown that elves are about six times more common than sprites, and occur primarily over oceans (despite the relative lack of lightning over oceans) and at equatorial latitudes [Chen *et al.*, 2008]. Furthermore, Mende *et al.* [2005a] used the ISUAL observations to show the presence of lightning-induced ionization enhancements associated with elves, while Kuo *et al.* [2007] made model comparisons with the ISUAL observations for optical emissions over the 185–800 nm wavelength range.

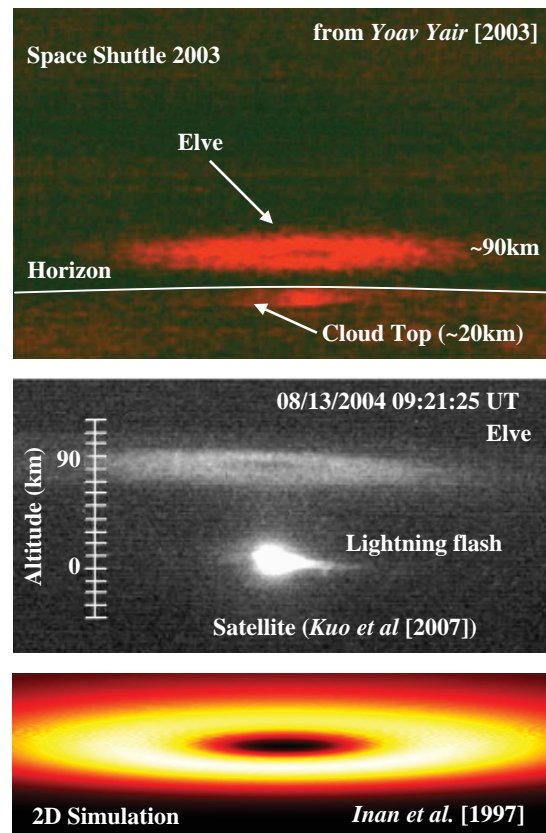


Figure 1.6: Examples of elves. Top: observed from the Space Shuttle in 2003 [Yair *et al.*, 2003]. Middle: observed from the FORMOSAT-2 satellite in 2004 [Kuo *et al.*, 2007]. Bottom: the ring-structure of elves was predicted by Inan *et al.* [1997] long before it was observed experimentally.

“Blue jets” are another class of TLEs, first observed by [Wescott et al. \[1995\]](#). These emissions are, as the name suggests, primarily blue (whereas sprites and elves are predominantly red), and are seen to propagate directly from the cloud top up to about 40–50 km altitude. Their propagation/expansion is typically slow compared to sprites (10^5 m-s⁻¹ compared to 10^7 m-s⁻¹ for sprites), and their observations have been relatively rare, due primarily to the need for airborne platforms (since blue light is scattered in air).

In the past few years, a new phenomenon has been discovered over oceanic thunderstorms near Puerto Rico [[Pasko et al., 2002](#)] and Taiwan [[Su et al., 2003](#)] known as a “gigantic jet”. The name comes from the fact that these events are also blue and propagate at speeds of $\sim 10^5$ m-s⁻¹, hence the relationship with blue jets, yet they continue to propagate and appear to connect to the ionosphere at 90 km altitude. Gigantic jets have not been associated with specific lightning discharges, but do occur only over large thunderstorms. A mechanism has been proposed for these gigantic jets by [Krehbiel et al. \[2008\]](#) which does not require a causative CG discharge. The fact that these events seem to be the first evidence of a direct connection between the thundercloud and the ionosphere (sprites terminate at 40–50 km altitude) has sparked great interest among the atmospheric electricity community. To date, only a handful of gigantic jets have been observed, and associated VLF and radio signatures have been documented only in a few cases [[Su et al., 2003](#); [Pasko, 2008](#)], but without evidence for causative CG lightning discharges.

1.5 VLF Signatures of Lightning

As mentioned above, the EMP from lightning radiates primarily in the 5–10 kHz range, in the middle of the VLF band. VLF frequencies propagate with very low loss (~ 2 dB/Mm after the first Mm; [[Crary, 1961](#)]) in the waveguide formed by the Earth and the lower ionosphere, within which VLF waves reflect at about 85 km altitude at nighttime. The EMP from lightning discharges can thus be observed at great distances; for example, lightning signatures are regularly observed from all over the globe with the Stanford VLF receiver at Palmer Station, Antarctica. These

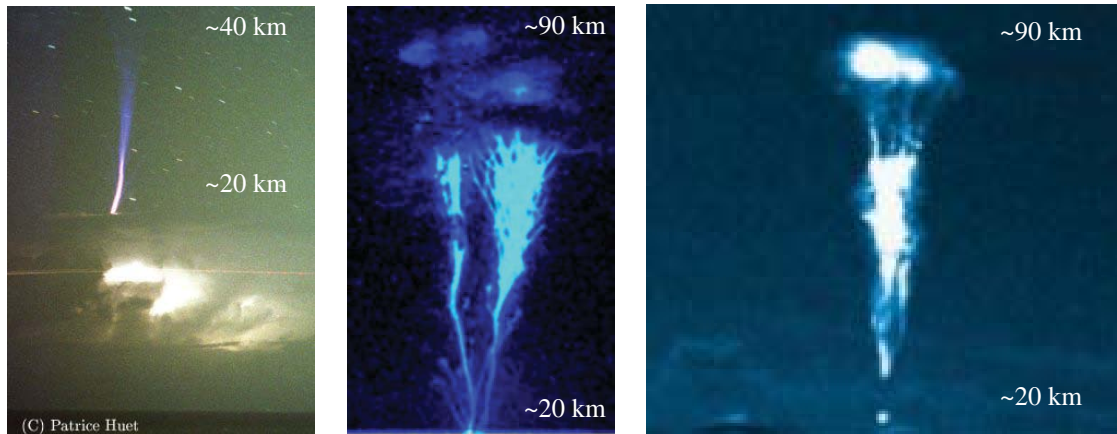


Figure 1.7: Examples of jets. Left: Blue jet observed from the ground [*Wescott et al.*, 1995]. Middle: gigantic jet observed by *Pasko et al.* [2002] from Arecibo Observatory, Puerto Rico. Right: Gigantic jet observed by *Su et al.* [2003] from Taiwan. The two gigantic jets here are recorded in black & white video and false-colored.

impulsive signatures are known as “radio atmospheric” or just “sferics” (intentionally misspelled to prevent any “spherical” connotations).

Quantitative analysis of VLF propagation in the Earth-ionosphere waveguide can become very complicated when one takes into account the losses in the Earth and the ionosphere, as well as the curvature of both [Section 1.3 herein; *Budden*, 1961; *Davies*, 1990]. To first order, the boundary conditions of the waveguide imply that modes with a vertical component of the electric field and transverse component of the magnetic field (TM modes) propagate with lower loss than those modes with a transverse electric field component (TE modes). Cloud-to-ground lightning preferentially excites low-order TM modes, since the current (and thus the resulting electric field) is vertical. On the other hand, in-cloud lightning preferentially excites high-order TE modes, due to the primarily horizontal current. As such, the signatures of CG lightning are far more easily observed at large distances than IC lightning, except in cases where the IC discharges have a significant vertical component.

At distances of greater than a few km from the discharge, the peak current of CG lightning can be inferred from the electric field amplitude measured. Analysis in

Uman and McLain [1970] was used by *Orville* [1991] to derive the simple formula:

$$E_{100} = \frac{I_p v}{2\pi d \epsilon_0 c^2} \quad (1.6)$$

where E_{100} is the peak electric field in $\text{V}\cdot\text{m}^{-1}$ observed at 100 km range along the ground from the discharge; I_p is the peak current in kA; and the constants v and d are the channel propagation speed and distance from the discharge, respectively, and take the values $1.5 \times 10^8 \text{ m}\cdot\text{s}^{-1}$ and 10^5 m . Hence, E_{100} (in $\text{V}\cdot\text{m}^{-1}$) = $0.3 I_p$ (in kA) and to first order, the two are directly proportional. A peak current of 90 kA, then, would be measured at 100 km as $E_{100} = 27 \text{ V}\cdot\text{m}^{-1}$. This nomenclature of E_{100} values for the amplitude of the lightning pulse is used throughout this work.

The sferic waveform measured at a VLF receiver depends on the source waveform as well as the distance from the source, since different waveguide modes propagate at different speeds, decay at different rates, and couple into and interfere with one another along the propagation path. Figure 1.8 shows an example sferic received 700 km from the source and 12,000 km from the source. The top panels present VLF data in “spectrogram” form, where the y -axes are frequency in kHz and the x -axes are time in milliseconds, and the color scale denotes field intensity in units of nanoTesla-per-root-Hertz ($\text{nT}\cdot\text{Hz}^{-1/2}$); The lower panels show the Magnetic field amplitude in nT as a function of time. A number of effects of waveguide propagation can be deduced from these sferics:

- At 700 km, the complete sferic duration is about 10 ms, but high-frequency components (above ~ 5 kHz) are primarily contained in the first 2 ms. Below 5 kHz, low-order modes have slow propagation velocities near their cutoff frequencies, which extend the sferic in time, and also show evidence of the cutoffs referred to as “tweeks” [*Helliwell*, 1965, p. 122]. In this example 3 tweeks are observed.
- At 12,000 km, the sferic lasts for over 20 ms, but again the high frequencies are contained in the first 2 ms. The portion below 1.5 kHz (the QTEM mode), referred to as the “ELF slow tail”, has very low attenuation over distance, but

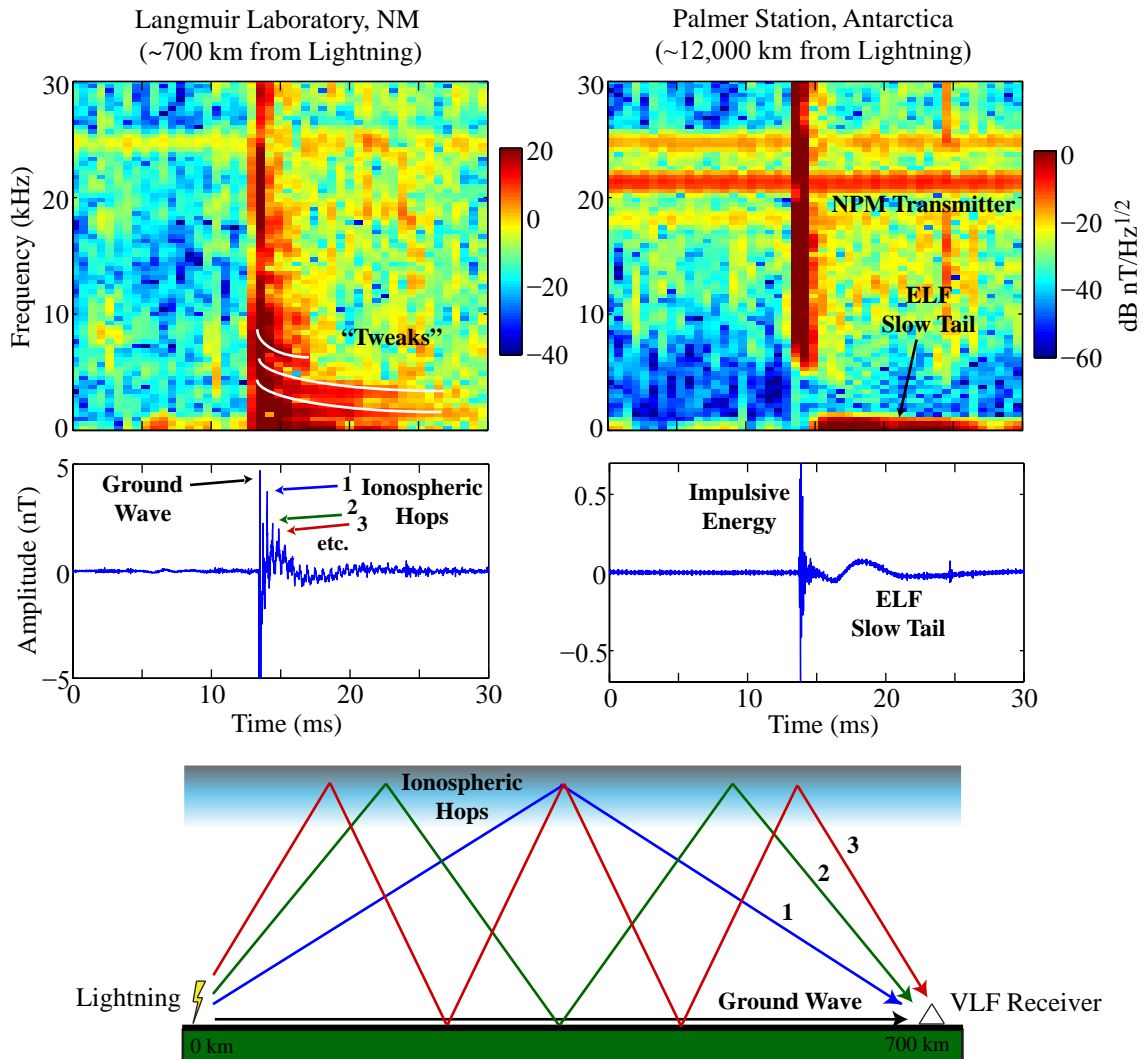


Figure 1.8: Example sferic event, observed at 700 km (Langmuir Laboratory, New Mexico) and 12,000 km (Palmer Station, Antarctica) in spectrogram and time-series formats. Below: illustration of ray-path ionospheric hop concept.

significant dispersion, leading to its 20 ms duration. There is almost no energy between 1.5 kHz and 5 kHz; the low-order modes suffer high attenuation, along with the dispersion seen at short range, and are almost completely attenuated at this great distance.

- At 700 km, a number of closely-spaced “spikes” are seen following the initial

pulse in the time-series data. These are the signatures of ray paths of different modes arriving at the receiver at different times due to the extended propagation distances. The initial sferic pulse propagates along the ground directly to the receiver; the 1st “sky wave”, in the ray picture, reflects from the ionosphere once before reaching the receiver; the 2nd sky wave reflects twice (including once off the ground); and so forth. Using these multiple bounces, the effective reflection height from the ionosphere can be easily deduced. These spikes become more spread out at larger distances of 1000–2000 km from the source: each mode propagates in the waveguide with a different speed, and so as the distance increases, the time difference between them also increases.

- At 12,000 km these reflections are no longer observed, as only the lowest order modes propagate such great distances.

The horizontal lines in the spectra around 20 kHz are VLF transmitter signals, which are discussed in the next section.

1.6 Early VLF Perturbations

VLF transmitters operate at a variety of locations in the United States and other countries, and are primarily used for long-range communications. In particular, the U.S. Navy uses VLF transmitters to communicate with submarines and surface ships, taking advantage of the low-loss, long-range propagation of VLF frequencies, as well as the penetration of VLF into seawater. These transmitters typically operate at frequencies around 20 kHz, though some operate up to 40 kHz or higher. They have radiated powers that range from tens of kW up to 1 MW. Most transmitters operate with minimum-shift keying (MSK), a particularly spectrally efficient form of coherent frequency-shift keying (FSK). Table 1.2 lists some of the most prominent VLF transmitters around the world. Figure 1.9 shows the location of the known VLF transmitters, as well as the current (2008–2009) locations of Stanford VLF receivers.

In recent decades, a direct correlation between lightning and perturbations to VLF transmitter signals has been observed [*Armstrong, 1983; Inan et al., 1988*]. These

Table 1.2: Representative VLF transmitters around the globe, listed in order of frequency.

Call sign	Location	Coordinates	f (kHz)	Power (kW)
NST	SE Australia	38.5 S, 146.9 E	18.6	Unknown
GQD	England	52.9 N, 3.3 W	19.6	100
NWC	NW Australia	21.8 S, 114.2 E	19.8	1000
HWV	France	48.5 N, 2.6 E	20.9	400
NPM	Hawaii, USA	21.4 N, 158.2 W	21.4	424
NSS ¹	Maryland, USA	38.9 N, 76.4 W	21.4	1000
JJI	Japan	32.0 N, 130.8 E	22.2	200
DHO	Germany	53.1 N, 7.6 E	23.4	800
NAA	Maine, USA	44.6 N, 67.3 W	24.0	1000
NLK	Washington, USA	48.2 N, 121.9 W	24.8	192
NLM	North Dakota, USA	46.4 N, 98.3 W	25.2	Unknown
NRK	Iceland	63.9 N, 22.5 W	37.5	Unknown
NAU	Puerto Rico	18.4 N, 67.2 W	40.75	100

¹Operated until 1999.

direct perturbations due to lightning, termed “Early/fast” events in the literature, manifest themselves as amplitude perturbations of anywhere from 0.2 to 3 dB, and/or phase perturbations of a few to tens of degrees. The name refers to their short delay from the lightning stroke (<20 ms) and fast rise to full perturbation (also <20 ms, constrained by the 50 Hz data sampling rate used to classify them), and is used to distinguish them from lightning-induced electron precipitation (LEP) events. In LEP events, lightning-generated whistler waves propagate into and are guided and dispersed by the Earth’s magnetosphere; when these waves reach the equatorial region, they can cause pitch-angle scattering of relativistic electrons, forcing some of these electrons to precipitate in the ionosphere in their subsequent magnetospheric bounce period. The secondary ionization produced by this precipitation, and its effect on subionospheric VLF transmitter signals, is what is known as an LEP event [*Peter, 2007*, and references therein]. Due to the propagation time of the whistler waves and the bounce period of the relativistic electrons, LEP events have a ~ 1



Figure 1.9: Map showing locations of VLF transmitters around the globe (blue), as well as 2008 array of Stanford VLF receivers (red). Note that this distribution of receivers is representative but not comprehensive.

second delay following the causative lightning stroke, and due to the whistler-wave dispersion they have a ~ 1 second rise time, and hence are both “late” and “slow” [Inan and Rodriguez, 1993].

In recent years, a subset of Early/fast events have been observed with no delay, but a rise time of 0.5–2.0 seconds, and have thus been termed “Early/slow” events [Haldoupis *et al.*, 2006]. The lack of delay suggests that these are direct effects on the ionosphere, and so are more closely related to Early/fast events than to LEP events. This observation has prompted the reclassification of all such direct perturbation events as “Early VLF perturbations”.

The cause of Early VLF perturbations (hereafter simply “Early events”) has been under debate almost since their discovery, and the lack of a definitive cause has provided the primary motivation for this work. Their association with sprites [Inan

et al., 1995] has led some researchers to suggest scattering of the VLF transmitter signal from the sprite body itself [Dowden *et al.*, 1996]; however, correlations described in Chapter 2 show that such scattering occurs in only a few rare cases. A number of alternative mechanisms for Early events have been suggested. Inan *et al.* [1996b] suggested that the ionosphere above a thunderstorm is held in a state of “sustained heating”, perturbed regularly by the charge removal of CG lightning discharges. However, model results resulted in perturbations much smaller than those observed. Barrington-Leigh *et al.* [2001] and Moore *et al.* [2003] instead suggested scattering associated with “sprite halos” and thus heating of the ionosphere due to the lightning QE field. However, this model is not able to explain particular correlations between sprites, halos, and Early events, nor the observation of Early/slow events, as discussed in greater detail later in this work.

Figure 1.10 summarizes the problem addressed in this work.

- a) An intense lightning discharge emits an electromagnetic pulse (EMP) due to the rapidly-varying current, and can also establish a quasi-electrostatic (QE) field due to charge removal. Sprites are the optical signature of the QE field exceeding the conventional breakdown threshold, while elves are the signature of the EMP impinging on the lower ionosphere and heating electrons.
- b) The EMP and QE fields due to CG and IC lightning may, in addition to producing elves and sprites, modify the lower ionospheric conductivity temporarily through heating (ΔT_e) and/or ionization, i.e., changes in electron density (ΔN_e). A VLF transmitter signal propagating in the Earth-ionosphere waveguide between the conducting ground and the conducting lower ionosphere may be perturbed by these changes in conductivity; in essence, the modified ΔT_e and ΔN_e have modified the waveguide itself.
- c) A VLF receiver some thousands of km away from the perturbation can detect these conductivity changes as changes in the amplitude and/or phase received.

The goal of this work is to understand the detailed physical mechanism (i.e., EMP versus QE fields, heating versus ionization, etc.) that causes Early events through

this sequence of processes. Chapter 2 presents detailed analysis of many years' data on sprites and associated VLF signatures. The correlations between the various phenomena lead to a hypothesis, presented at the end of the chapter, for a new mechanism for Early event production, namely that bursts of EMP pulses from in-cloud lightning discharges modify the lower ionosphere enough to create measurable conductivity changes. Chapter 3 describes a 3D Finite-Difference Time-Domain model of the lightning EMP-ionosphere interaction, which is used to quantify the effect of realistic lightning EMPs on the lower ionosphere in terms of localized, transient changes in the electron density. Chapter 4 uses a Finite-Difference Frequency-Domain model of the subionospheric VLF transmitter signal propagation to measure the changes in amplitude and phase that result from the modified electron density. Chapter 5 summarizes the results and presents suggestions for future research.

1.7 Scientific Contributions

The major contributions of this dissertation are as follows:

1. Four years of sprite observations, narrowband VLF transmitter amplitude and phase data, and broadband VLF sferic data are used to establish correlations between sprites, Early events, and sferic bursts. Prior work [[Johnson and Inan, 2000](#)] established that Early/fast events are seen in one-to-one correlation with sferic bursts, i.e. for every observed Early/fast event, significant sferic burst activity was observed in the broadband data. In this work the study is extended to compare the observations of sprites with Early events and sferic bursts, and a strong, but not one-to-one, correlation is found. In addition, it is shown through direct quantitative correlations that sferic bursts are the VLF signature of in-cloud lightning bursts, a connection that was previously untested. These correlations are the primary topic of Chapter 2.
2. Using the correlations above, a hypothesis is established that bursts of in-cloud lightning EMPs modify the lower ionospheric conductivity through cumulative changes in electron density. This hypothesis is the first to explain the recent

observations of Early/slow events, and is also hypothesized to account for the predominance of positive polarity amplitude changes in Early events. The details of this hypothesis are outlined at the end of Chapter 2.

3. A 3D Finite-Difference Time-Domain (FDTD) model of the lightning EMP–ionosphere interaction is developed and used to quantify the effects of realistic cloud-to-ground and in-cloud lightning impulses on the overlying ionospheric electron density. This model is a 3D extension of the 1D model used in *Taranenko et al.* [1993a,b], but with updated ionization, attachment, and optical excitation rates. The model reproduces elves and shows that significant asymmetry in elve observations can be explained by the effect of the Earth’s magnetic field. The model also demonstrates that both in-cloud and cloud-to-ground lightning significantly affect the lower ionospheric electron density in a region 10 km thick and hundreds of km in radius. The EMP model and results are the topic of Chapter 3.
4. A 2D Finite-Difference Frequency-Domain model developed by *Chevalier et al.* [2008] is used to determine the effect of the EMP-induced electron density disturbances on the subionospheric VLF transmitter signal. This model calculates the three components of the wave electric field \vec{E}_w , and wave magnetic field \vec{H}_w , over a 2D region from 0–110 km in altitude and many thousands of km in length. This model is briefly introduced, and then results are presented in Chapter 4.

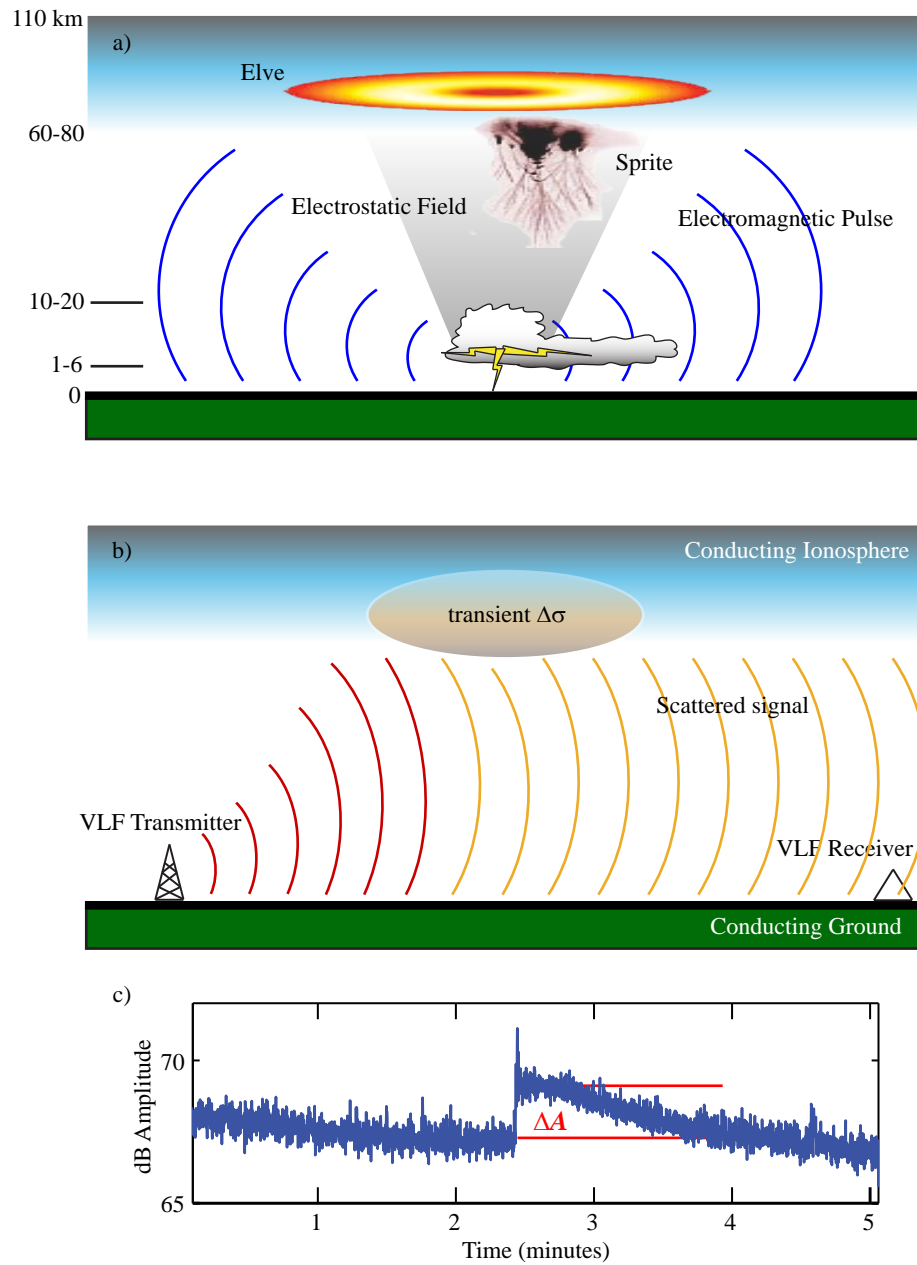


Figure 1.10: Ionospheric effects of lightning. a) Lightning emits EMP and establishes a QE field, which lead to sprites and elves; b) these QE and EMP fields interact directly with the ionosphere, causing changes in conductivity; c) these conductivity changes are detected via subionospheric VLF remote sensing as changes in the amplitude and/or phase of the transmitter signal.

Chapter 2

Sprites, Early VLF Events, and Sferic Bursts

This chapter presents analysis of data from four summers during which coordinated VLF and sprite observations were conducted in the mid-western United States. Observations in Europe [*Neubert et al.*, 2005; *Haldoupis et al.*, 2004], along with the sprite–Early/fast connections made by *Inan et al.* [1995], provide the motivation to revisit the many years of data collected in the United States in the 1990’s. Using this data, correlations between sprites and Early VLF events are reinterpreted in Section 2.2. Section 2.3 examines the connections between sprites and sferic bursts, and the correlations between Early VLF events and sferic bursts made by *Johnson and Inan* [2000] are summarized in Section 2.4. Section 2.5 summarizes these correlations and puts forth a new mechanism for Early VLF event production. We begin with a discussion of the short history of Early VLF studies.

Note that there is some discrepancy in the nomenclature of “Early/fast” versus “Early VLF” events. These events were initially labeled “Early/fast”, but have been renamed “Early VLF” in recent years in recognition of the recently discovered “Early/slow” events [*Haldoupis et al.*, 2006]. In the history that follows, the nomenclature has been kept consistent with the work at the time; in the remainder of this work these events will be referred to as “Early VLF” or simply “Early events” when discussing the entire class of events, and Early/fast and Early/slow only to describe

particular events.

2.1 History of Early VLF Research

Sudden amplitude and/or phase perturbations of subionospheric VLF signals were first associated with lightning by *Armstrong* [1983], and were studied extensively in the 1980's and 1990's [*Inan et al.*, 1988, 1993]. These events, initially referred to as “Early Trimpi”, were observed with no delay after the lightning stroke, in direct contrast to another class of events known as “lightning-induced electron precipitation” (LEP) events, which have a 1–2 second delay. LEP events are caused by large electron density changes in the lower ionosphere, due to relativistic electrons precipitated out of the magnetosphere by lightning-generated whistler waves [*Voss et al.*, 1984]. LEP events have been observed on satellites [*Voss et al.*, 1998; *Inan et al.*, 2007a] through direct particle measurements, and on the ground [*Peter and Inan*, 2007, and references therein] via subionospheric VLF remote sensing.

The possibility of direct heating of the lower ionosphere by lightning, as observed in “Early Trimpi” events, was first recognized by *Inan et al.* [1991]. Therein, the authors modeled electron heating through an enhanced thermal (i.e., Maxwellian) electron distribution and calculated heating by factors of 100–500, and electron density enhancements due to ionization of up to 400 electrons per cm^3 . *Taranenko et al.* [1993a] improved the 1D calculations of direct ionospheric heating to consider fully kinetic simulations of the evolving electron energy distribution. It was found that a stationary electron distribution could be used as long as the fields did not vary rapidly on time scales less than about $10 \mu\text{s}$. Later, *Glukhov and Inan* [1996] would show that the stationary assumption yields realistic results for time scales down to 1–2 μs . *Taranenko et al.* [1993a,b] calculated heating, ionization, dissociative attachment, and optical emissions for realistic lightning pulses and found appreciable electron density changes and observable optical emissions. These calculations of optical emissions stand as the first prediction of elves.

The observable differences between LEP events and these direct heating effects of lightning in the lower ionosphere were first cataloged in *Inan and Rodriguez* [1993].

The most obvious difference is the time delay from lightning: LEP events are delayed by the time it takes the VLF wave energy to propagate (as a “whistler”) to the equatorial region of the Earth’s magnetosphere, plus the time for scattered particles to reach the ionosphere. This time delay is typically 1–2 seconds; in contrast, direct heating requires, at minimum, only the few hundred μs it takes the electromagnetic pulse to reach the ionosphere.

It was observed that these direct heating effects, like LEP events, recover back to their ambient levels in tens of seconds up to 100 seconds, with very rare longer or shorter cases. These recovery times have been interpreted in terms of the chemical relaxation of the lower ionosphere through associative detachment and electron recombination [Pasko and Inan, 1994].

Beginning in 1995, the focus in studies of Early/fast events shifted toward sprites, whose observations had just started to become more common [Lyons, 1994]. Pasko *et al.* [1995] looked at the ionization effects related to sprites, caused by the quasi-electrostatic (QE) field, and calculated orders-of-magnitude increases in ionization at sprite altitudes. In a seminal paper, Inan *et al.* [1995] made the first association between Early/fast events and sprites, and suggested forward-scattering of the VLF signal from disturbed regions of the ionosphere of 100–150 km scale size as the cause of Early/fast events. Without directly implying the QE field as a mechanism, this association definitely propelled research in that direction. In a Comment-and-Reply sequence [Dowden, 1996; Inan *et al.*, 1996a], controversy over the source of these Early/fast events arose, Dowden [1996] suggesting VLF scattering from the sprite body.

1996 saw the first observation of elves [Fukunishi *et al.*, 1996], as well as a prediction of their space-time structure through the first 2D modeling of the EMP–ionosphere interaction [Inan *et al.*, 1996c, 1997]. The observation of rapid lateral expansion of elves with the novel Fly’s Eye photometric array confirmed the predictions and the EMP as the driving mechanism [Inan *et al.*, 1997]. Meanwhile, model results of Pasko *et al.* [1997] reinforced the idea that sprites are produced by the quasi-electrostatic field. At this time a new mechanism for Early/fast events was proposed [Inan *et al.*, 1996b], wherein the ionosphere is held in a state of “sustained

heating” by the unbalanced thundercloud charge, and that heating is perturbed by large lightning discharges. This mechanism, however, was only able to reproduce perturbations of less than 0.1 dB in amplitude.

Pasko et al. [1998] directly suggested that ionospheric effects as measured through Early/fast events could be caused by the QE field extending into the lower ionosphere, causing heating and thus conductivity changes at 80–90 km altitudes. At this time considerable research was undertaken to quantify the QE field and its relation to sprites, leading to the correlation between sprite occurrence and charge moment change in the causative lightning stroke [*Cummer and Inan*, 1997, 2000].

Veronis et al. [1999] extended the model of *Inan et al.* [1997] to include electrostatic field components, and calculated the effects in the ionosphere of the combined EMP/QE fields from lightning. This model was later used by *Barrington-Leigh et al.* [2001] to calculate time-resolved optical emissions in elves and led to the prediction and discovery of sprite halos. The model was also used by *Moore et al.* [2003] to calculate the perturbations to subionospheric VLF transmitter signals. While the amplitude changes received were small compared to measured values, this result theoretically connected Early/fast events and sprite halos.

Interest in Early/fast events began in earnest in Europe with the series of “EuroSprite” observational campaigns [*Neubert et al.*, 2001, 2005, 2008]. Using Stanford VLF receivers in France and Crete, *Haldoupis et al.* [2006] reported the observation of “Early/slow” events: these are perturbations that occur immediately following the lightning stroke (similar to Early/fast events), but may take 1–2 seconds to rise to their full amplitude change (i.e., “slow”, like LEP events). *Haldoupis et al.* [2006] suggested that Early/fast and Early/slow events formed a continuum of events, rather than distinct classes — prompting their renaming as simply “Early” VLF perturbations — and proposed a mechanism involving in-cloud lightning activity. In their mechanism, sprite initiation is key: the sprite produces “seed” electrons through ionization caused by the QE field, and these seed electrons are energized by subsequent EMP fields from IC discharges, and proceed to create secondary ionization.

In summary, over the years a number of mechanisms have been proposed to explain Early VLF events, which are repeated here along with their observational or

theoretical problems:

1. *Backscatter from sprite body.* The association between Early/fast events and sprites [Inan et al., 1995] has led some researchers to suggest scattering of the VLF transmitter signal from the sprite body itself [Dowden et al., 1996] as the mechanism for Early/fast events. However, this suggestion came before higher-resolution images of sprites revealed their streamer nature, with spatial scales of tens to hundreds of meters, far below the VLF transmitter wavelengths. Scattering from objects much smaller than a wavelength would suggest omnidirectional scattering; however, Early/fast events were later definitively observed to scatter predominantly in the forward direction [Johnson et al., 1999]. A small number of observations do suggest possible backscatter from sprites [Marshall et al., 2006], but only in a few rare cases.
2. *Sustained heating.* Inan et al. [1996b] suggested that the ionosphere above a thunderstorm is held in a state of “sustained heating”, perturbed regularly by the charge removal of CG lightning discharges. However, model results calculated perturbations much smaller than those observed. This result may have been due to the fact that the model used was restricted to altitudes below 80 km for computational reasons.
3. *QE heating.* The QE field as a cause of Early/fast events was suggested directly by Inan et al. [1996c] and Pasko et al. [1998] in response to the association between sprites (i.e., the QE field) and Early/fast events [Inan et al., 1995]. In this model, the QE field extends into the lower conducting ionosphere and directly heats electrons. However, heating alone cannot account for all Early/fast events, as the heating recovery time back to an ambient ionosphere is very rapid (a few seconds) at ionospheric altitudes; thus, the QE field must create ionization, which requires a threshold twice that of optical emissions (described in detail in Chapter 3). Furthermore, many Early/fast events are observed without sprites or halos; if the QE field is not strong enough to produce optical emissions it cannot produce ionization.

4. *EMP ionization.* The model results of [Taranenko et al. \[1993a\]](#) suggest the possibility that the lightning EMP may cause enough ionization to be observed as Early/fast events. Correlations between Early VLF events and elves were made by [Mika et al. \[2006\]](#); however, it is premature to conclude a direct cause in these events as one has no information about other processes occurring at the same time (i.e., in-cloud lightning components). Furthermore, it was recognized by [Inan et al. \[1996a\]](#) that EMP-induced ionization may occur above the VLF reflection height and would thus not be detected by subionospheric VLF propagation techniques. The possibility of EMP-triggered Early VLF events is investigated as part of this work in Chapters 3 and 4 where we simulate vertical (i.e., cloud-to-ground) lightning effects on the ionosphere.
5. *Combined QE/EMP heating and ionization.* [Moore et al. \[2003\]](#) used the association of sprite halos with the QE field from [Barrington-Leigh et al. \[2001\]](#) to suggest heating of the ionosphere due to the combined QE and EMP fields. The model used in that work cannot separately treat the two fields, except through particular choices of lightning parameters. Still, this model can only reproduce very small Early/fast perturbation amplitudes, and is not able to explain particular associations between sprites, halos, and Early events, as will be discussed in greater detail in Section 2.2.2.

In this chapter we take a closer look at the correlations between sprites, Early VLF events, and sferic bursts.

2.2 Sprites and Early VLF

In this section we compare observations of sprites with Early VLF events detected during the summers of 1995, 1999, and 2000. The work described in this section is a modified and updated version of [Marshall et al. \[2006\]](#).

It has been shown that sprite halos involve changes in ionospheric density commensurate with the VLF signal perturbations typically observed, leading to the conclusion that Early/fast VLF perturbations may be signatures of halos [[Moore et al., 2003](#)].

Such considerations are based on the experimentally verified forward-scattering of the VLF signal from a nearly Gaussian-shaped perturbation of lateral size 90 ± 30 km [Johnson *et al.*, 1999], and thus would only lead to signal perturbations if the causative lightning flash is within ~ 50 km of the signal path [Inan *et al.*, 1996d], consistent with most of the Early/fast VLF data reported to date [i.e., Inan *et al.*, 1996d; Johnson *et al.*, 1999].

On the other hand, as mentioned in Section 2.1, Dowden *et al.* [1996] attribute direct subionospheric VLF signal perturbations to a different mechanism. In cases reported by these authors, the causative lightning strikes are ~ 300 km from the signal path, and are associated with sprites, so that the VLF signal perturbation is attributed to scattering from ionization in the sprite body that persists well beyond the optical sprite lifetime of a few ms. This interpretation was further supported by Hardman *et al.* [1998] using an expanded data set. Furthermore, these authors suggest that such scattering occurs for nearly all sprites, so much so that observations of VLF perturbations can be used as a sprite detection method in the absence of optical data. Such scattering processes in the Earth-ionosphere waveguide have been modeled by Rodger *et al.* [1998], Rodger and Nunn [1999], and Rodger *et al.* [1999], although that work did not consider the 10–100 second recovery times or the possibility of sferic intrusion into the narrowband channel. Additionally, Corcuff [1998] observed VLF perturbations in Europe that could only be attributed to a particularly large (~ 350 km) perturbed region, or to wide-angle scattering, though sprites were not conjectured as the source.

In the summer of 2003, sprites were observed over France from a camera platform in the Pyrenées Mountains [Neubert *et al.*, 2005]. Simultaneously, VLF recordings were made at Nançay, France, and the University of Crete in Heraklion. Results of this experiment were reported in Haldoupis *et al.* [2004] and Mika *et al.* [2005]. In particular, Haldoupis *et al.* [2004] reported VLF perturbations in one-to-one association with sprites, while Mika *et al.* [2005] reported the possibility of rare examples of “backscatter” of VLF signals from the sprite body of the kind discussed by Dowden *et al.* [1996]. However, these events were observed ~ 150 – 200 km from the VLF receiver, and so it was concluded that they could be attributed to overlap of the

density-enhanced region (i.e., the sprite halo) over the VLF signal path. These recent results motivated us to revisit previously unpublished results, in order to better quantify the association between sprites and Early/fast events and to assess the conditions under which rare backscatter events may occur.

The following section investigates case studies of sprite and Early VLF observations during particularly active days in 1995, 1999, and 2000.

2.2.1 Case Studies

15 July 1995

During the summer of 1995, sprites were observed optically from Yucca Ridge Field Station (YRFS), near Fort Collins, CO; a Stanford VLF receiver was located near the observing platform. This receiver recorded broadband data continuously from ~ 30 Hz to 30 kHz, and in addition, the broadband signals were bandpass-filtered in real time with ~ 200 Hz bandwidth around known transmitter signal frequencies, including the NAA (Cutler, ME) signal at 24.0 kHz, NSS (Annapolis, MD) at 21.4 kHz, and NLK (Seattle, WA) at 24.8 kHz, to produce amplitude data with 20 ms time resolution. Furthermore, using real-time phase-coherent demodulation of the MSK-modulated signal, phase data is extracted from these signals at the same 20 ms resolution.

A total of 38 sprites were observed on July 15, 1995, between 05:40 and 07:40 UT, in a storm 300–500 km east of YRFS, as shown in Figure 2.1. For the purposes of VLF data comparison, these comprise 24 independent sprite “events”, since in many cases up to 4 sprites are observed within a short time span of each other (< 1 s) and cannot be distinguished in narrowband VLF data. Of these 24 optical events, 16 had corresponding VLF signal perturbations in amplitude and/or phase on the NAA and NSS great circle paths shown in Figure 2.1, based on a typical minimum detectable VLF event magnitude of 0.2 dB in amplitude and ~ 3 degrees in phase (sometimes lower, depending on the noise level).

In addition, during the time period of observations, 11 VLF perturbations were found on the NAA and NSS signal paths that were not accompanied with sprite

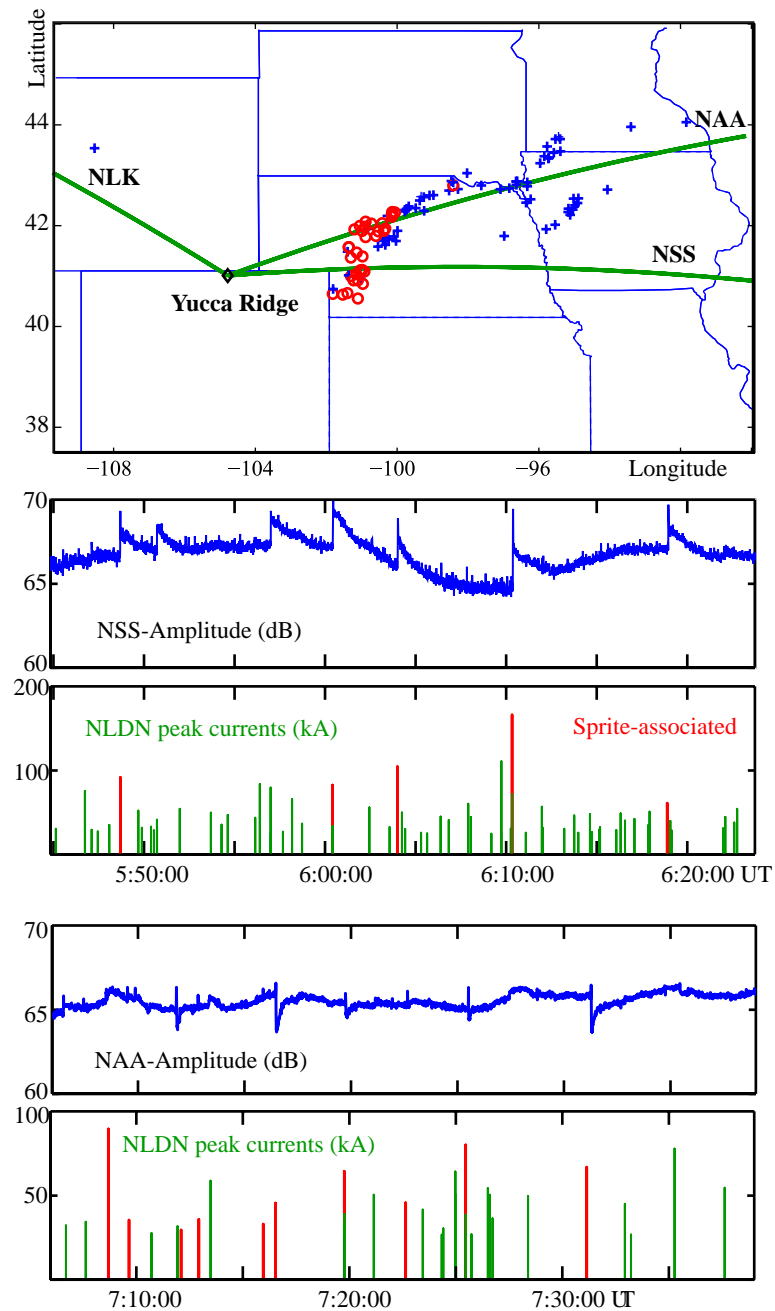


Figure 2.1: Top: Map of 15 July 1995 observations from 05:30 to 07:30 UT. The red circles indicate locations of sprite-inducing CGs; blue +’s indicate other +CGs > 50 kA. Below: Data from two time periods during this day. The earlier events correspond to more southern part of the storm, and hence occur on the NSS path; later events appear on NAA when +CGs occurred further north.

observations. These perturbations were all associated with lightning flashes reported by the National Lightning Detection Network (NLDN) to be in the same region as the sprite-producing flashes, within the 20 ms time-resolution of the narrowband VLF data. These events were tallied after eliminating those events for which the high altitude regions above the causative CG lay outside the camera field-of-view at the time. Any sprites present would thus be well within the field-of-view of the cameras, but yet no sprites were detected.

It is also important to note that sprite observations are frequently marred by clouds in the field-of-view, as was indeed the case for the July 1995 observations. In such cases, when sprite observations are ambiguous, VLF data are not used for the statistics.

Associated with 5 of the sprite events were VLF signal perturbations on the NLK path, arriving at YR from the west, and not passing through the ionospheric region above the causative CG flashes as shown in Figure 2.1. Most of these were very small perturbations (~ 0.3 dB), and are observed simultaneously with larger perturbations on the NAA and NSS paths. An example is shown in Figure 2.2 at left, where a 2.0 dB perturbation is seen on the NSS amplitude signal, 0.7 dB on the NAA amplitude, and 1.0 dB on the NLK path, this being the largest such event. This particular perturbation occurred simultaneously with a series of 4 sprites within 600 ms of each other, resulting from 4 consecutive +CG flashes. The consecutive sprites were displaced from each other horizontally within the camera FOV, i.e., along a north-south line, noting that any displacement along an east-west line cannot be determined. In each of the other four cases of perturbations on the NLK paths, the associated sprite events were each a series of 2–4 sprites, displaced from each other in the plane of the camera FOV (along a north-south line). This observation suggests the establishment of a “grid” of ionization extending along a distance greater than the VLF wavelength, perpendicular to the NAA-YR and NSS-YR paths.

Furthermore, note that for 4 of the 5 events described above, perturbations were also observed on the NSS and/or NAA paths. In all four of these cases, the recovery times τ_r (defined as the time for the perturbation to recover from 90% of its perturbed value back to 10%) were only about half as long on the NLK path than they were on

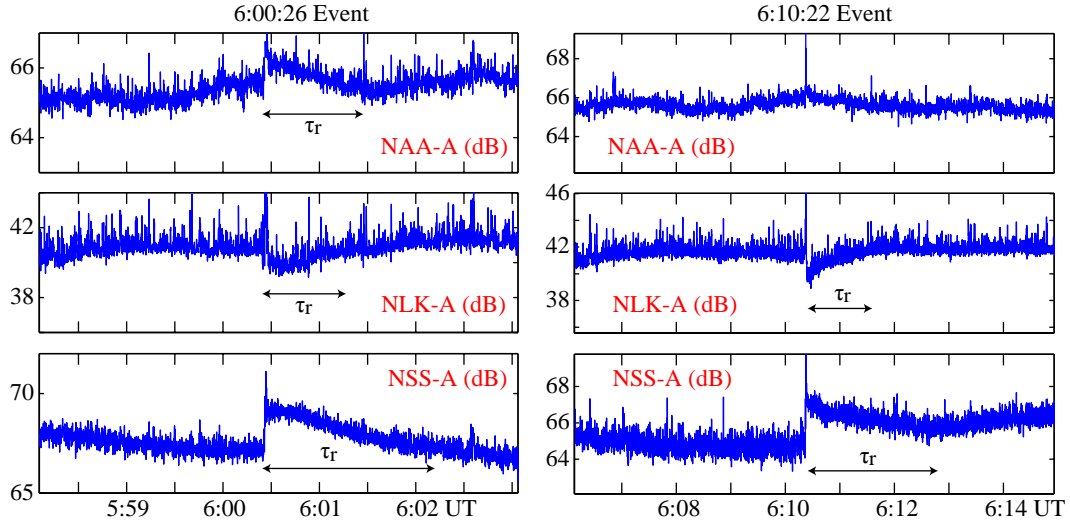


Figure 2.2: Example VLF perturbations from 15 July 1995, at 6:00:26 UT and at 6:10:22 UT. The first event followed a series of four +CGs located a minimum of 280 km east of YRFS, the largest of which was 91 kA. The strong perturbation on the NLK path is evidence of backscatter of VLF energy from the sprite body, and of persistence in the conductivity enhancement created by the sprite. The longer recovery times τ_r on the NSS and NAA paths show that scattering also occurs from halo altitudes.

the NSS or NAA paths (see Figure 2.2). Since the relaxation times for newly added secondary ionization drop rapidly with altitude [Pasko and Inan, 1994], this observation is consistent with the ionization that causes the perturbations on the NLK path being at lower altitude, providing further evidence that these particular perturbations may be caused by backscattering from the sprite body, while the perturbations on the NSS and the NAA paths may be dominated by the forward scatter from sprite halos [Moore *et al.*, 2003]. It thus appears that while some configurations of sprites can backscatter VLF energy, the forward scattering from higher altitude features (in the halo region) are typically dominant, as evidenced by the larger and longer lasting perturbations on the NAA-YR and NSS-YR paths.

Note that the data presented here contain many of the same sprites analyzed in Dowden *et al.* [1996]. In that work, most of the sprites were reported to have corresponding “backscatter” events (perturbations to the NLK signal path), contrary

to the findings presented here. The major observational differences are that VLF observations in [Dowden et al. \[1996\]](#) were made from near Boulder, CO, while data presented here were recorded at YRFS; and that [Dowden et al. \[1996\]](#) measurements were made with 400 ms time resolution, while data herein were recorded with 20 ms resolution.

18 August 1999

On August 18, 1999, over 100 sprites were observed between 02:30 UT and 07:30 UT above a large thunderstorm to the Northeast of YRFS. At this time, the Stanford Holographic Array for Ionospheric Lightning research (HAIL) was in use. The HAIL array is a north–south aligned array of VLF receivers from Cheyenne, WY to Las Vegas, NM, designed to image in space and time the disturbed regions due to LEP and QE heating events [[Johnson et al., 1999](#)]. The array monitors the amplitude and phase of VLF transmitter signals from NAA, NLK, NAU (Puerto Rico) at 40.75 kHz, and NPM (Lualuaei, HI) at 21.4 kHz (note that the NSS transmitter was no longer operating by this time). Figure 2.3 shows the HAIL array and the location of the storm and sprite-producing CGs for this date.

Figure 2.4 shows HAIL data from 05:00 to 06:00 UT for this day. Numerous large events are present, as well as a number of smaller events. It is evident upon comparison with the sprite times and NLDN data that many of these events correspond to sprite observations; however, once again, there are also many events do not have associated sprites.

The 100+ sprites observed on this day can be categorized into 87 independent sprite events, according to the same criteria as the 1995 case. Of these, 56 were associated with VLF signal perturbations. Given that the HAIL array was used to bound the size of typical perturbation regions to ~ 150 km in diameter [[Johnson et al., 1999](#)], it is evident that for this case study, the lack of events during sprite times cannot be attributed to the lack of VLF paths nearby, since no causative lightning flash was more than 32 km from any of the VLF paths being monitored. Another 71 VLF signal perturbations were observed that were not associated with sprites; 44 of those were verified to occur in association with lightning in the same region as

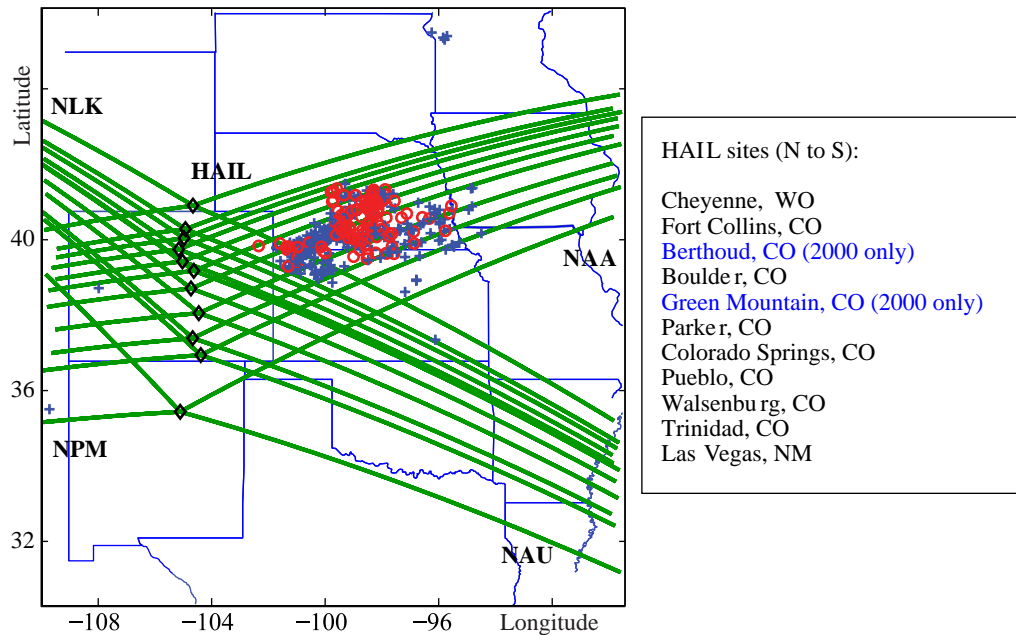


Figure 2.3: Map showing locations of sprites (\circ) and other $+CGs > 50$ kA ($+$) for the storm of 18 August 1999, from 02:30 to 07:30 UT. The HAIL paths from NLK, NAA, NAU and NPM are also shown.

the sprite-producing flashes, and within the camera field-of-view. Only 4 VLF signal perturbations were observed on the NLK paths; one example is shown in Figure 2.5. Of these 4 events, 2 events showed perturbations in amplitude and 3 showed phase perturbations (one event had both). However, the largest NLK signal amplitude and phase perturbations were only 0.4 dB and ~ 6 degrees, respectively; in comparison, large events on the NAA paths associated with sprites during this day exhibited changes of up to 2.0 dB in amplitude and 20 degrees in phase. Only a handful of events were seen on the NAU transmitter paths, all of which can be associated with forward-scattering based on their locations with respect to the HAIL paths. No VLF perturbation events were detected on any of the NPM signal paths.

Figure 2.6 shows a histogram of the VLF perturbation amplitudes for sprite-related and non-sprite-related VLF events. It is evident that sprite-related events are typically larger, and that the largest events always coincide with sprites. Overall,

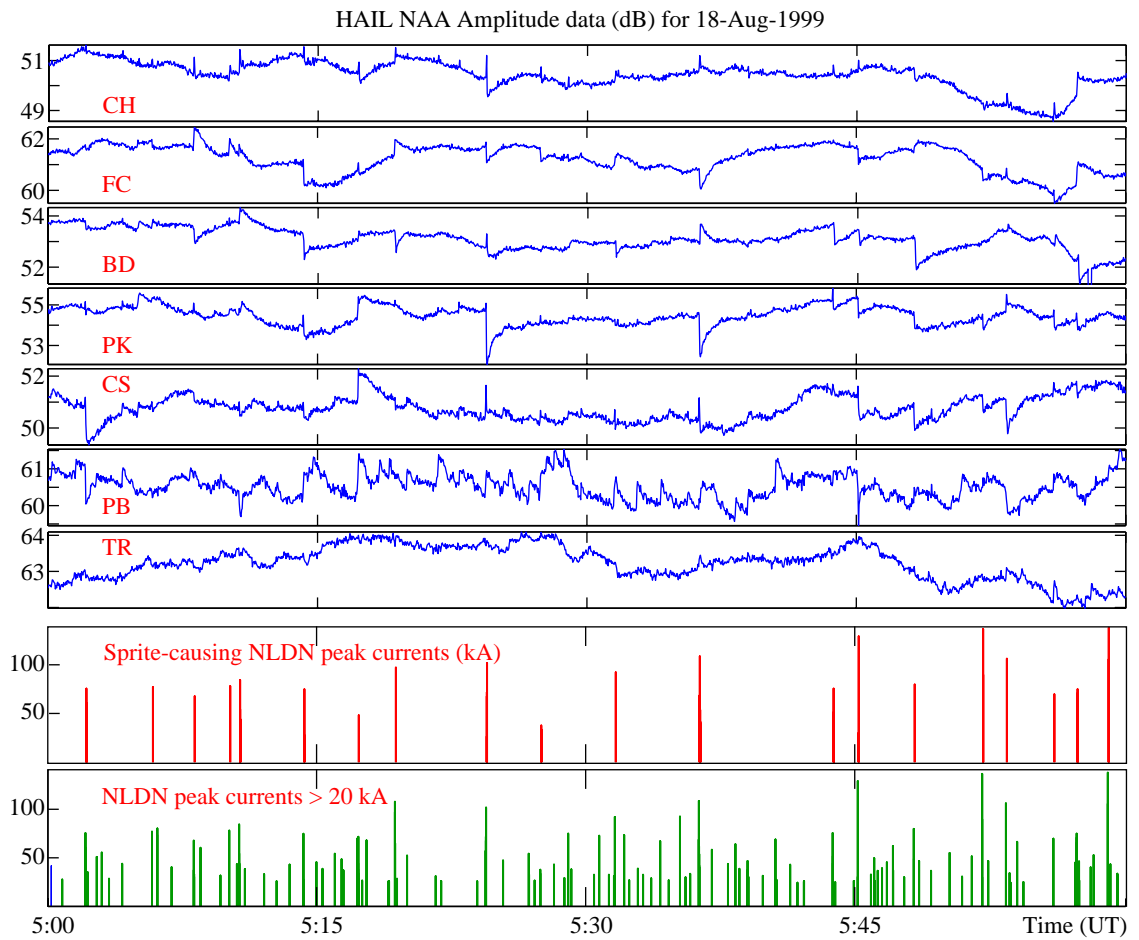


Figure 2.4: 18 August 1999 Narrowband VLF data from the HAIL array for a one-hour period starting at 5:00 UT. Plotted below the data are the lightning peak currents of sprite-causing CGs, and of all CGs > 20 kA. It is evident from this figure that most, but not all, of the VLF perturbations in this time period are associated with sprites.

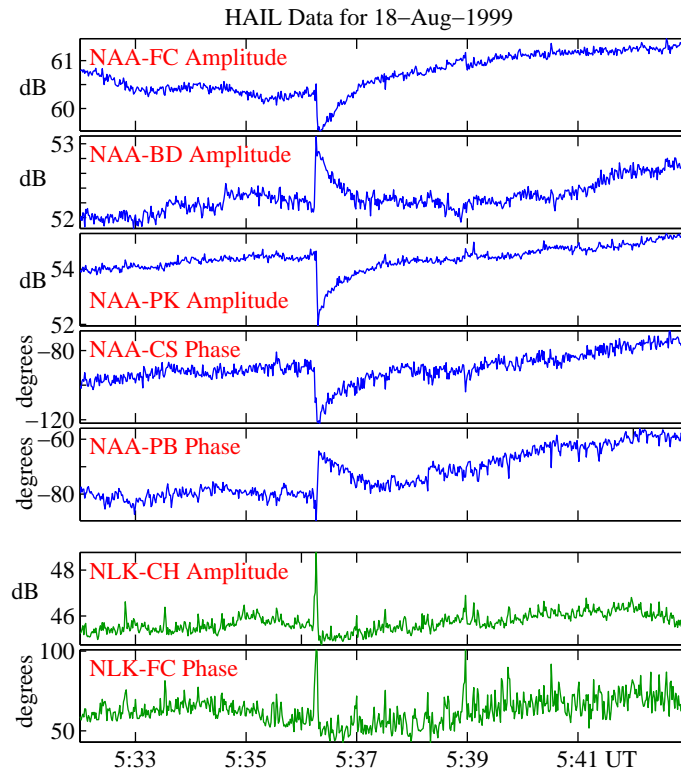


Figure 2.5: 18 August 1999 Narrowband VLF data for an event occurring at 05:36 UT, in association with a sequence of 5 sprites. Large perturbations are seen in phase and amplitude on the NAA paths, and small perturbations are evident on the north-most (CH and FC) NLK paths.

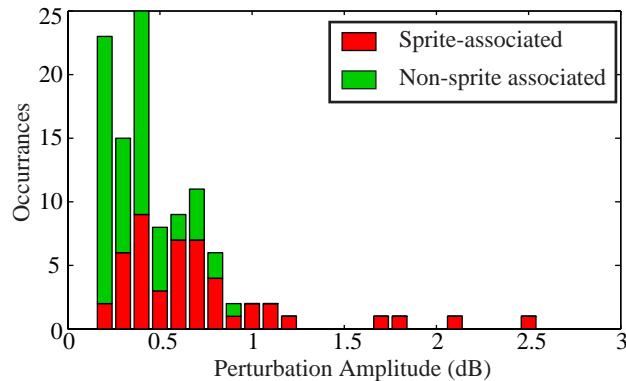


Figure 2.6: Perturbation amplitudes for sprite-associated and non-sprite-associated VLF perturbations of August 18, 1999. All of the largest perturbations are associated with sprites; the largest of the perturbations without sprites is 0.9 dB.

the sprite-related events have an average perturbation of 0.71 dB, while non-sprite-related events have an average of 0.37 dB. This finding may simply indicate that the same characteristics of the parent lightning that control sprite occurrence (i.e., charge moment or the QE field that leads to heating of ambient electrons; see *Cummer and Inan [2000]*) also leads to the ionospheric disturbances that are signified by Early VLF perturbations.

July 2000

Sprites were observed from YRFS on 9 nights in July 2000; this section presents data from 8 of those nights. This data set provides a range of storm conditions to monitor, including large mesoscale convective systems displaced from the HAIL paths (02 July, which is not used in this section) or overlapping the HAIL paths (04 July), as well as smaller, or more distributed storms on the HAIL paths (06 July; 22 July).

The locations of sprites and +CGs for 22 July 2000 relative to the HAIL array are shown in Figure 2.7. It is evident that most of the sprites occurred near the NAA-TR path; indeed, most of the VLF perturbations are seen on this path, as shown in Figure 2.8 for a two-hour period. The overall statistics of sprites and early/fast events for July 2000 are shown in Table 2.1; 02 July is not included, since the storm was far from the HAIL paths. Overall, of 151 sprites observed on the nights listed

Table 2.1: Sprite and VLF early/fast event occurrences for July 2000

Date	Sprites	Sprites with VLF	VLF without Sprites
3 Jul	25	1	0
4 Jul	43	26	8
6 Jul	5	2	4
11 Jul	4	0	0
18 Jul	14	7	0
19 Jul	15	3	2
22 Jul	45	14	11

in Table 2.1, 53 had corresponding VLF perturbations, typically on the NAA-HAIL paths. Only 25 other VLF perturbations were found within the region covered by the camera field-of-view. Once again, the data exhibits clear evidence of sprites with and without corresponding VLF perturbations, and vice versa.

On 02 July 2000, a large storm to the Northeast of YRFS produced a huge number of small sprites, as presented by *Gerken and Inan* [2004]. No perturbations were found on the NAA or NAU paths, as expected, since the storm was located more than 400 km (lateral distance) from the nearest HAIL path. However, 9 VLF perturbations were found on the NLK paths, 5 of which were coincident with sprite-causative +CGs. No CGs were found nearby in time for the other four VLF perturbation events, which could instead be attributed to lightning-induced electron precipitation events due to lightning in a storm near 31° N, 106° W to the southwest of the HAIL array, which coincidentally occurred within ~ 0.5 s of the sprite. Furthermore, upon comparison with sprite image data, it was found that these 5 events coincide with the largest sprites observed on this night, and that 4 of the 5 were composed of multiple sprites, extending laterally to tens of km. Figure 2.9 shows two of these sprites for comparison, along with a typical “reference” sprite for that night.

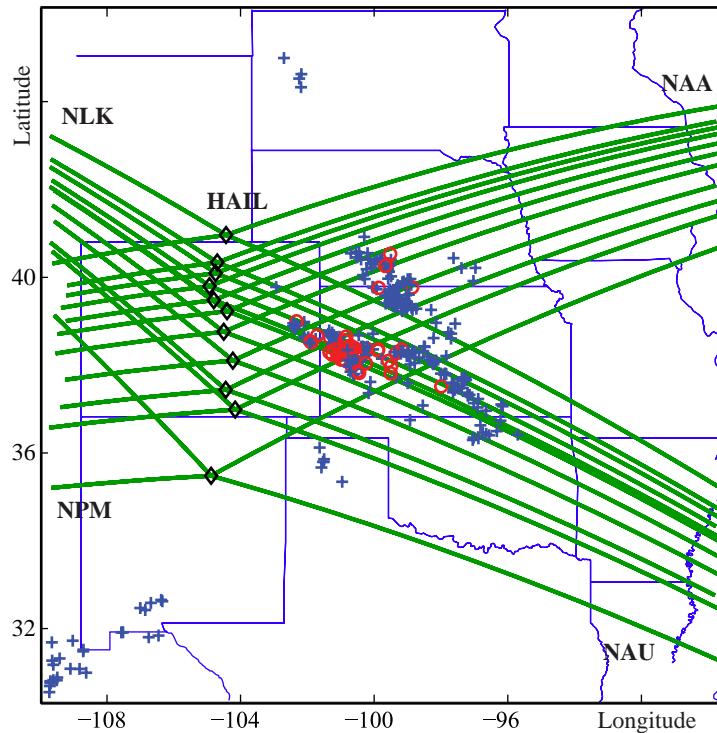


Figure 2.7: Map showing locations of sprites (\circ) and other +CGs > 50 kA ($+$) for storm of 22 July 2000, from 03:00 to 07:00 UT. The HAIL paths from NLK, NAA, NAU and NPM are also shown.

2.2.2 Discussion and Interpretation

VLF Backscatter from Sprites

The 5 NLK perturbations on 15 July 1995, and the 4 such events on 18 August 1999, are suggestive of the possibility of scattering of VLF energy from the sprite body. In the 1995 cases, the causative +CGs occurred 280–330 km from the receiver at YRFS, a distance too great for the perturbations to be attributed to the QE-heated region (e.g., the sprite halo) overlapping the VLF signal path, since this region has been constrained to a radius of <100 km [Johnson *et al.*, 1999]. There remains the possibility that these perturbations were associated with EMP-induced conductivity changes in the ionosphere, associated with elves (the brightnesses of which may have been below the camera sensitivity); since elves have observed radii extending to a

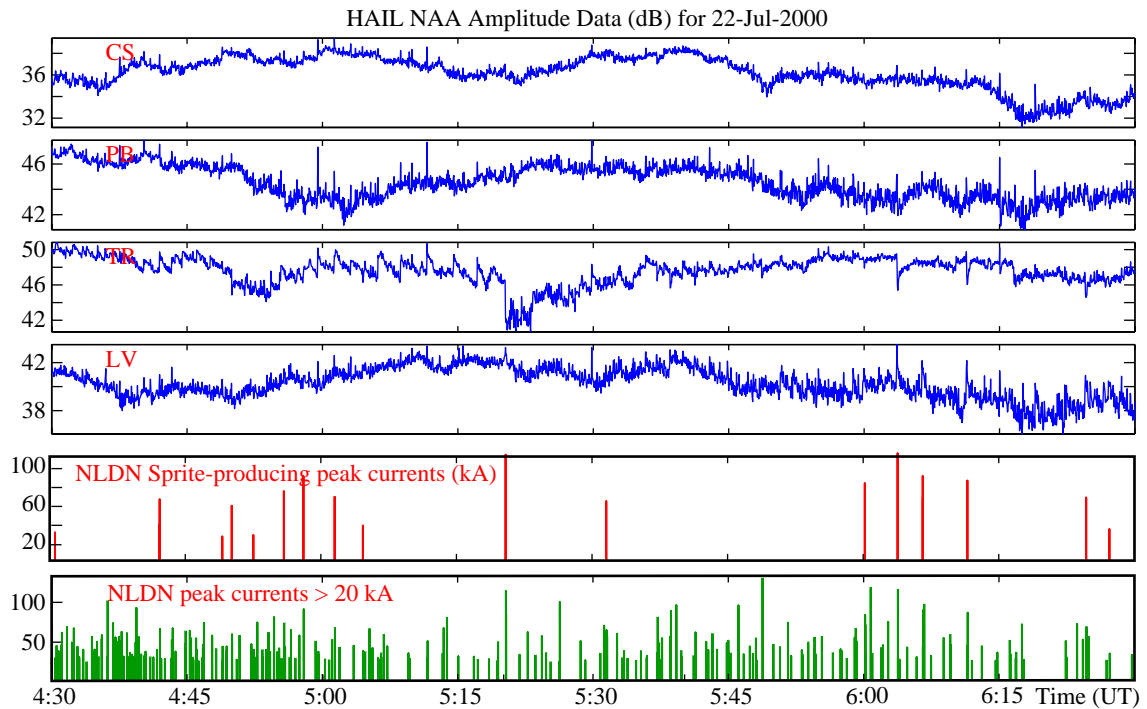


Figure 2.8: VLF narrowband data for a two-hour period on 22 July 2000. Lightning data is plotted for sprite-causing CGs and for all CGs > 20 kA. A large number of small VLF perturbations are evident, and many are associated with sprite-causing CGs.

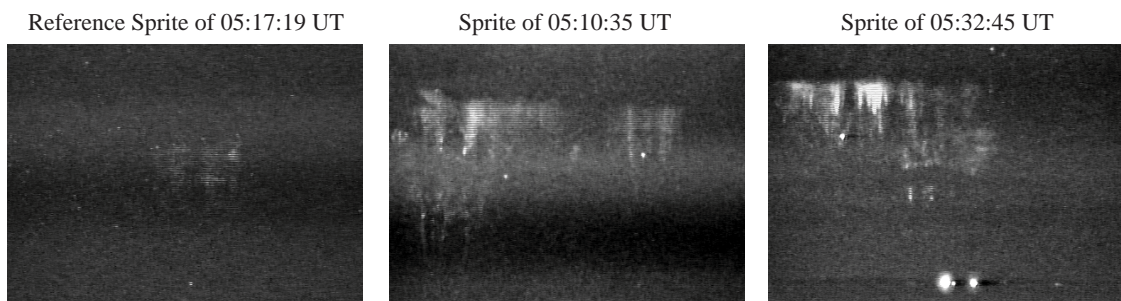


Figure 2.9: Large sprites observed on 2 July 2000. Left: a “typical” sprite for this night, at 5:17:19 UT; most sprites are even smaller than this one. Middle and Right: Sprite events for 5:10:32 and 5:32:45 UT. These events are image sums over a few sprites occurring within a few seconds of each other, to show the spatial extent over the entire sprite event.

maximum of 330 km [*Barrington-Leigh et al.*, 1999]. However, the 18 August 1999 NLK perturbations were all associated with +CGs 400–500 km from the receiver, and the 02 July 2000 events were >500 km distant. Furthermore, *Taranenko et al.* [1993a] predict ionization enhancements due to EMP at altitudes of 85–95 km, above the VLF reflection height, and in agreement with elve observations [*Fukunishi et al.*, 1996; *Barrington-Leigh et al.*, 2001]. In addition, recent studies have shown very few isolated elves (i.e., those without accompanying sprites) to be associated with VLF perturbations [*Mika et al.*, 2006]. The possible association of elves with VLF perturbations is investigated in more detail in Chapters 3 and 4.

The possibility remains, then, that at least some of the perturbations on the NLK signals are caused by scattering from the sprite features, as postulated by *Dowden et al.* [1996]. However, *Dowden et al.* [1996] claim that “essentially all red sprites are associated with VLF [perturbations] irrespective of their displacement from the Great Circle Path”, implying a one-to-one correspondence between sprites and VLF signal perturbations. The authors further claim that this fact can be used to detect the occurrence of sprites without optical data. However, the data presented here clearly show that this is not the case, that backscatter from sprites occurs very rarely, and that only very few sprites are associated with VLF perturbations when the sprite is over 100 km from the VLF transmitter path.

The fact that VLF backscatter events are extremely rare (9 such events out of more than 250 sprites analyzed) suggests that they might be associated with the largest sprites in terms of their horizontal extent, such that they create a large (compared to VLF wavelength) “conductive grid” for reflection of the VLF energy. In most of the backscatter cases reported here, the perturbations are associated with multiple sprites. In this way, the sprites occurring in close succession set up a conductive grid (columns of ionization that decay over time scales of a few to tens of seconds) that is much larger than their individual size. This hypothesis also agrees with the sprites observed for 02 July 2000 and presented in Figure 2.9, which are horizontally expansive and are composed of multiple sprites. It is interesting that these events involve perturbations of the NLK signals but not of the NAA transmitter; in this case, due to the storm location, NAA perturbations could in principle also be attributed

to wide-angle scattering from the sprite body and not forward-scattering from the halo. The lack of NAA perturbations may be due to directional scattering; modeling results by *Rodger and Nunn* [1999] of scattering from a real distribution of sprite features showed a complex series of nulls and peaks in the angular scattering pattern. In addition, *Rodger et al.* [1999] showed similar nulls and peaks, on the order of ~ 100 s of km, along the lateral direction from the transmitter to the receiver, attributed to interfering waveguide modes. These nulls and peaks and waveguide mode interference will be discussed in Chapter 4.

Figure 2.10 shows a correlation between sprite “brightness” and magnitude of VLF perturbation on the NAA or NSS signals. Since no forward-scatter perturbations were observed on 02 July 2000 due to the storm location, data is shown only for the 1995 and 1999 cases. In this figure the sprite “brightness” is defined by integrating the luminosity produced by the sprite over the entire pixel range of the image, where the pixel values range from 0 to 255, so that “brightness” is a factor of both luminosity and size. For the July 1995 and August 1999 cases, sprite brightness is weakly correlated with VLF perturbation amplitude. However, it is important to note that this analysis method suffers from the fact that larger lightning discharges will likely produce both larger sprites and larger Early VLF events whatever the physical mechanism is for these perturbations, so that correlation itself certainly does not provide evidence for scattering from the sprite body. Figure 2.10 also shows that the rare backscatter events are, in most cases, associated with the brightest sprites, though not always with the largest perturbations, as is also evident in the 02 July 2000 data. Thus, these “backscatter” events appear to be more closely linked to the sprite itself than to density enhancements at higher altitudes (e.g., sprite halo altitudes) in the ionosphere, which may be signified by the typical forward-scatter signature of the NAA and NSS signals.

Correlation of Sprites with VLF Perturbations

From the data presented above it is concluded that VLF perturbations are not observed in a one-to-one relationship with sprites, so that the perturbations cannot be attributed exclusively to scattering from the sprite body. In the data set presented

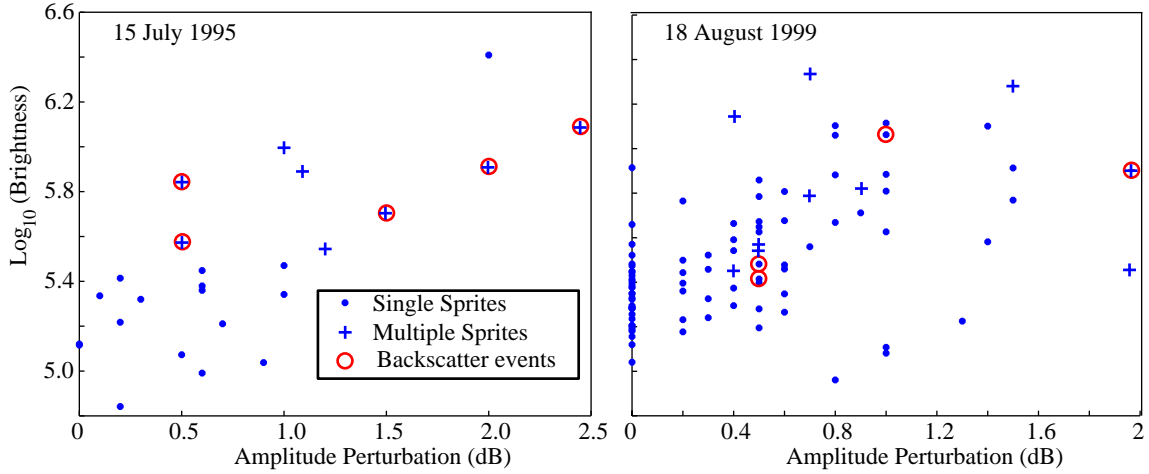


Figure 2.10: Sprite Brightness versus VLF perturbation amplitude for the 15 July 1995 and 18 August 1999 cases. The sprite “brightness” is the integrated luminosity of the image, and is thus a function of both intensity and size.

here, $\sim 48\%$ of sprites have associated VLF perturbations; or, when viewed conversely, $\sim 61\%$ of VLF perturbations are associated with sprites. This result may corroborate the hypothesis that VLF perturbations are associated with the mechanism of sprite halo production, and thus with the modeling results of *Moore et al.* [2003], since sprites are frequently observed with or without accompanying halos. Indeed, in the same data set, examples of sprite halos are observed without accompanying sprites, but with accompanying VLF perturbations. However, contrary to *Moore et al.* [2003], halos are also observed with and without associated VLF perturbations, and vice versa. The only exception is when sprites and halos are seen together; all such cases examined had associated VLF perturbations. Examples of each of the possible combinations are shown in Figure 2.11.

While the lack of a one-to-one association between sprites and Early VLF perturbations in this data set appears to be inconsistent with the findings of *Haldoupis et al.* [2004], the difference between these may well be due to the fact that the disturbed ionospheric regions in the cases studied by *Haldoupis et al.* [2004] were much closer to the VLF transmitter. When the signal propagation from transmitter to receiver is

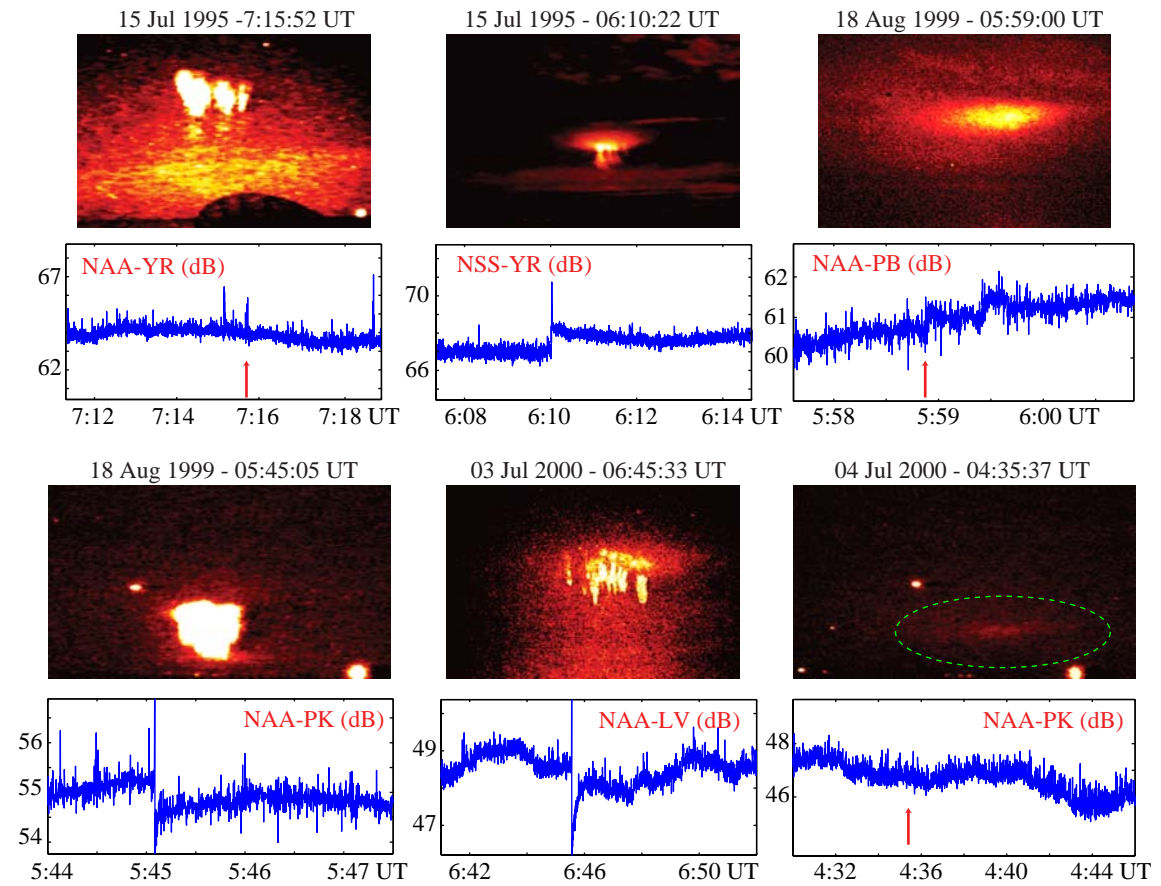


Figure 2.11: Examples of sprite/halo/VLF combinations. Clockwise from top left, a sprite with no halo and no VLF event; a sprite with halo and VLF event; a halo with no sprite, with a VLF event; a halo with no sprite and no VLF event; a sprite with halo and large VLF event; and a sprite with no halo and with a VLF event. The images have been color-contrasted to bring out the weak halos. Arrows in the VLF data point to the time of the sprite, except where obvious.

broken into waveguide modes, the forward-scattering of VLF energy from the ionospheric density perturbation may occur in one or only a few propagating modes. Over the length of the propagation path, energy may couple between modes, and over a long distance, the perturbation signature may be washed out through this coupling process. In the data presented in [Haldoupis et al. \[2004\]](#), the causative CGs were near the transmitter, and the receiver was some ~ 1000 s of km away, so that only the largest perturbations would survive to the receiver; and, these largest perturbations (caused by the largest CGs, in terms of peak current and/or charge moment) would likely coincide with sprites, as shown in the data set presented here. Conversely, in these observations the causative CGs are close to the receivers (~ 100 s of km away), so that even the smaller perturbations survive the distance to the receiver without being washed out in mode-coupling, and these smaller perturbations may not have associated sprites.

This scenario is contrary to the conclusions of [Haldoupis et al. \[2004\]](#), which related the one-to-one correspondence to the proximity of the perturbed region to the transmitter. Therein it was proposed that higher-order modes, which decay rapidly as they propagate away from the transmitter, could be more easily perturbed by the ionospheric density enhancement, and thus through mode-coupling into lower-order, better-propagating modes, the perturbation could survive to the VLF receiver some 1000s of km away. However, that postulate suggests that in data such as presented here, where the perturbed region is farther from the transmitter, smaller VLF events would not be seen, despite the occurrence with sprites, so that all VLF perturbations would be required to have corresponding sprites, although some sprites may not have detectable VLF events. The data presented here show clear examples of VLF perturbations without sprites, so that the rationale expressed by [Haldoupis et al. \[2004\]](#) is not likely to be the sole reason for the difference between the two data sets.

2.2.3 Summary

Data have been presented from three periods of sprite history that correlate with Early/fast VLF event observations. The data show that when the geometry allows

for the measurement of even the smallest density perturbations (i.e., when the receiver is $< \sim 500$ km from the perturbation), they do not occur in one-to-one correlation with sprites. It has been shown that many sprites occur without coincident VLF signal perturbations, while in other cases, such as Early/fast events are seen without coincident sprites. It has also been shown that only a very small subset of sprites show characteristics of VLF backscatter from the sprite body, and that all such cases correspond to multiple sprites or horizontally expansive sprites.

2.3 Sprites and Sferic Bursts

In this section, the correlation between sprites and sferic bursts is investigated using four summers of VLF and sprite data from 1995–2000. This section is modified from [Marshall et al. \[2007\]](#).

Recent observations have revealed the occurrence of burst-like VLF activity, lasting from tens of ms up to a few seconds, associated with the onset of many sprites. These “sferic bursts” are thought to be due to the horizontal in-cloud component of lightning activity, since they have been observed to only propagate short distances (a few hundred km) in the Earth-ionosphere waveguide and are generally not reported by lightning detection networks. The possible involvement of in-cloud lightning in sprite production has been previously suggested based on the observed long delays and spatial displacement between causative cloud-to-ground (CG) discharges and sprite events. This section compares the occurrence of sferic bursts in association with sprites for thousands of observations over many different dates and a variety of thunderstorms, and investigates the source of these bursts by comparing VLF data to Lightning Mapping Array (LMA) data of VHF pulses due to lightning.

While most sprites occur within a few to tens of ms after the causative +CG [[São Sabbas et al., 2003](#)], some have been seen to have delays up to 200 ms or more [[Bell et al., 1998](#); [Mika et al., 2005](#)]. It has been suggested [[Valdivia et al., 1997](#); [van der Velde et al., 2006](#)] that the contribution of the in-cloud component of a CG discharge to the production of sprites may explain these long-delayed sprites. [van der Velde et al. \[2006\]](#) showed that long-delayed sprites are often accompanied by bursts of

very-low-frequency (VLF) sferic activity, referred to as “sferic clusters” [*Johnson and Inan, 2000*] or “sferic bursts” herein (the latter nomenclature is chosen due to the fact that such bursts do not exhibit properties of a set of individual sferics; rather, they appear as a burst of continuous noise-like VLF activity). *Johnson and Inan [2000]* associated these sferic bursts with in-cloud lightning, based on the observations that i) they do not propagate to great distances in the Earth-ionosphere waveguide, typical of horizontal sources, and ii) they are not reported by the National Lightning Detection Network (NLDN), which, until April 2006, reported only CG discharges.

Johnson and Inan [2000] also showed a one-to-one correspondence between sferic bursts and Early/fast events. In prior publications on sferic bursts [*Johnson and Inan, 2000; Ohkubo et al., 2005; van der Velde et al., 2006*], the identification of sferic bursts as signatures of in-cloud lightning was based on the two observations stated above from *Johnson and Inan [2000]*. *van der Velde et al. [2006]* attempted to show a correlation between sferic bursts and VHF sources reported by a SAFIR 2D interferometric lightning mapping system, but did not find agreement in time. VHF sources are important in this context since *Stanley [2000]* showed that they were correlated in time with spider lightning lasting up to a few seconds. In this section, data is presented from hundreds of sprites that were observed near the New Mexico Tech Lightning Mapping Array (LMA) during its deployment in the summer of 2000; this deployment was part of the very productive STEPS program [*Lang et al., 2004*]. This study thus provides the most complete correlation of sprite, VLF, and LMA activity to date.

2.3.1 Description of the VLF Data

VLF data were recorded at Yucca Ridge Field Station during most summers from 1995–2000; this work focuses on data during 1995, 1996, 1998, and 2000, as these provided the best overlap in the optical sprite data and VLF data. VLF data were collected by two orthogonal 1-meter square magnetic loop antennas, oriented in the North–South and East–West directions. The VLF receiver had a flat frequency response from ~ 10 Hz up to 30 kHz. The data from the two antennas were originally

recorded on Betamax tapes with PCM coding on two data video channels, with IRIG-B timing from GPS on the audio channel. For this study the data were converted to DVD format, the process of which involves filtering the analog read-out from the Betamax channels with a 4-pole hardware low-pass filter with cutoff at 15 kHz, and redigitizing the data with a sampling rate of 33.3 kHz and 16-bit resolution.

In total, about 6000 sferics were analyzed for burst activity. About 2000 of these had associated sprites, optically confirmed from YRFS in 1995, 1996, 1998, and 2000. Sprite-associated sferics were located by searching through VLF broadband data for known, archived optical observation times of sprites. Non-sprite associated sferics were located by searching for all non-sprite associated +CGs greater than 50 kA, as reported by NLDN, within the periods of sprite observations and within 1000 km of YR. They are also confirmed to be within the field-of-view of the cameras while operating. While the choice of positive CGs only and the large 50 kA threshold unfortunately restricts the data set, it is necessary to reduce the number of cases, and limits us to the comparison of sprite-producing and non-sprite-producing large +CGs. In Figure 2.12, the peak currents of sprite-associated and non-sprite associated NLDN strokes are shown in histograms to show that there is no peak current bias in favor of sprite-associated sferics. Also in Figure 2.12, the distances of each NLDN stroke to YRFS is shown, again showing no bias. A few errors (shown in white) are due to the search algorithm occasionally finding the wrong NLDN stroke (often when no +CG was reported by NLDN, or where a larger +CG was found within 1 second of the sprite-causative CG).

2.3.2 Results: Sprite Correlations

Figure 2.13 shows three examples of VLF sferic bursts. Each of these examples occurred in association with a sprite, where the causative CG occurred at the time marked by the arrows. These examples demonstrate the wide variability in sferic bursts, and the fact that sprites can sometimes occur without any VLF burst activity at all, as in the first case. However, results below show that most sprites are found in association with at least some obvious sferic burst activity.

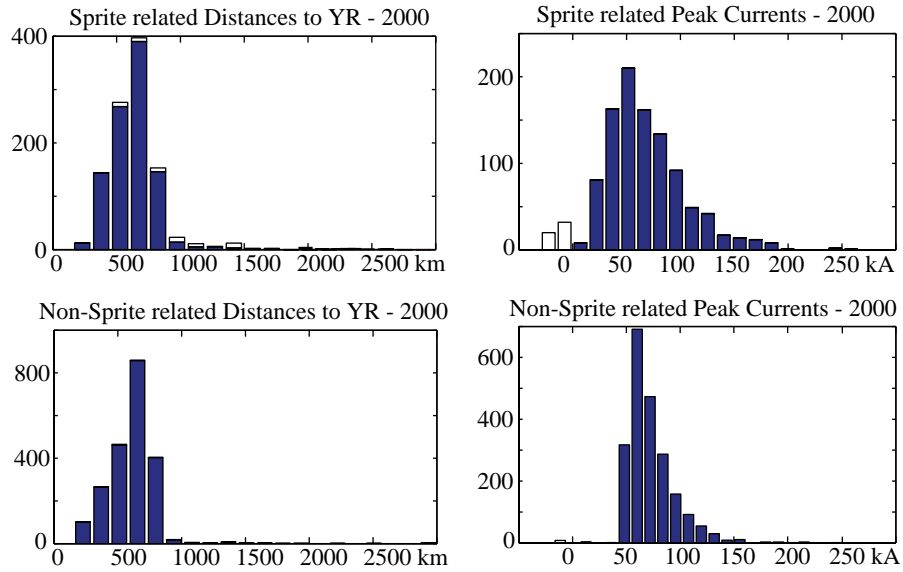


Figure 2.12: Distributions of peak currents and distances to the receiver for sprite and non-sprite NLDN CGs, showing no preference for sprite-related events.

In order to make a quantitative comparison of events, the energy in each sferic event is measured. Four time points are located on each event: i) the start of the sferic burst activity (which sometimes begins before the CG-induced sferic), ii) the start of the CG-induced sferic, iii) the end of the sferic, and iv) the end of the sferic burst. Note here that the “sferic” is defined as being only the return stroke component of the VLF signature, whereas the “sferic burst” refers to the long-duration activity seen in Figure 2.13. Within each of the three resulting sections, energy is calculated by evaluating the power spectral density (PSD) of a hamming-windowed periodogram. The total energy is then calculated by integrating the PSD over the frequency range of the data and the respective time intervals. To normalize the energy values and to allow comparison of events from different days and times, background noise is subtracted by taking average noise power samples every five minutes. The pre-CG (i→ii) and post-CG (iii→iv) energies are then added and the North–South and East–West component vectors are combined, a procedure which is equivalent to removing the CG-induced sferic itself from the calculation. The results are given below in Figure 2.14 by year.

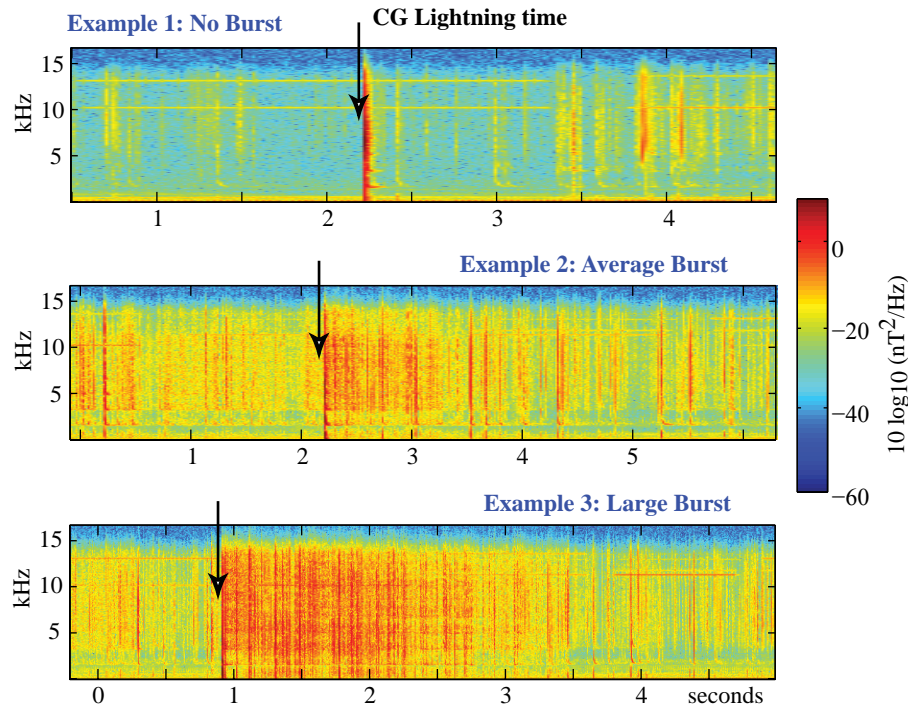


Figure 2.13: Examples of sferic bursts. The arrows show the time of the CG discharge. Each of these cases is associated with a sprite.

These results show a marked difference in energies, about a factor of 5, between sprite-related and non-sprite-related events (note the shift in the distributions, as marked by the green arrows). In comparison, the sferic energy (ii→iii) in each case shows little difference between sprite-related and non-sprite related events (vertical green arrows), indicating that the data are not biased by sferic intensity.

While *van der Velde et al.* [2006] reported no cases of sprite-associated sferic bursts that lasted longer than 250 ms, in this data set there are many such events, lasting up to 3 seconds in some cases, consistent with observations of in-cloud lightning using VHF time-of-arrival (TOA) techniques, as discussed later in this section. Figure 2.15 shows distributions of burst times leading up to and following the CG, for both sprite and non-sprite cases. It is evident that sprites are generally associated with much longer duration bursts, and that the burst activity following the CG is generally much

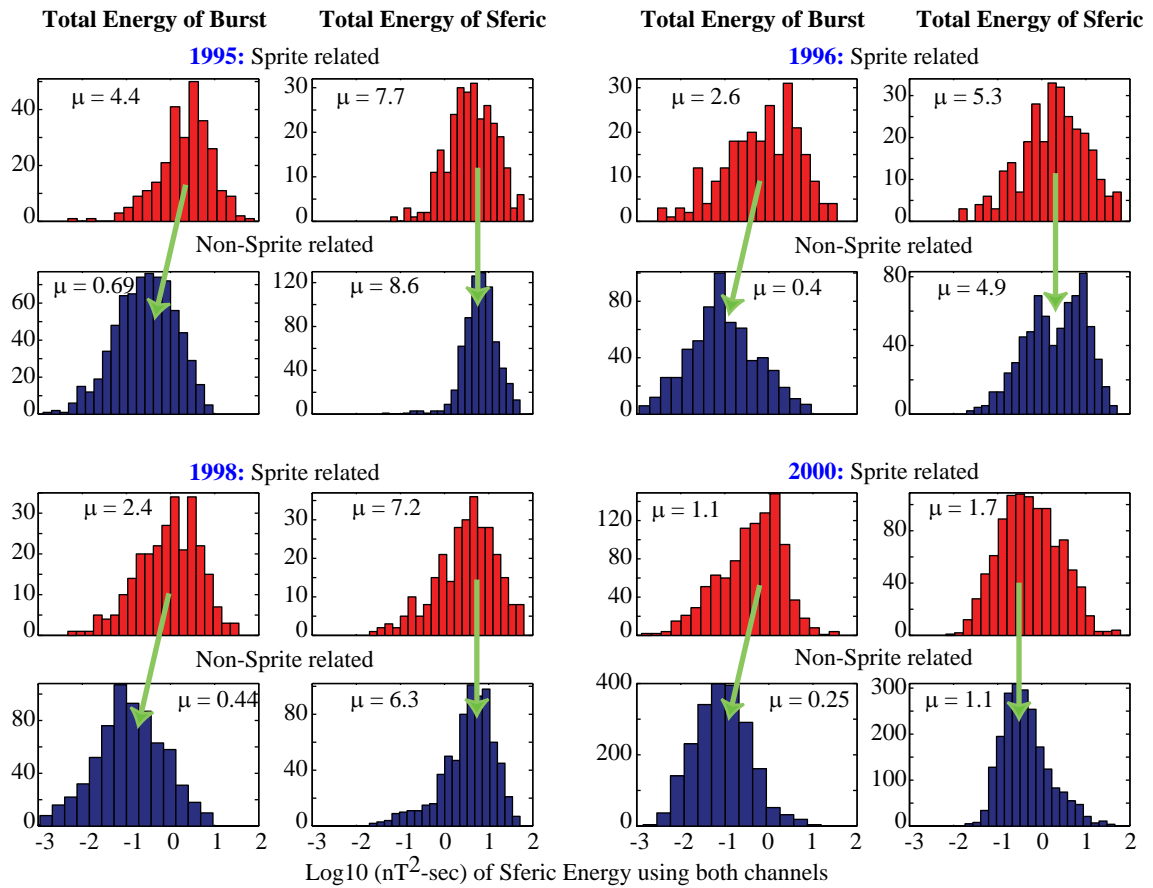


Figure 2.14: Distributions of sferic energy for each year, in units of nT²-sec. Histograms are of the energy of either the sferic only, or the burst activity outside the sferic. The clear shift in each histogram from sprite to non-sprite cases demonstrates the interrelationship. μ refers to the mean of each distribution.

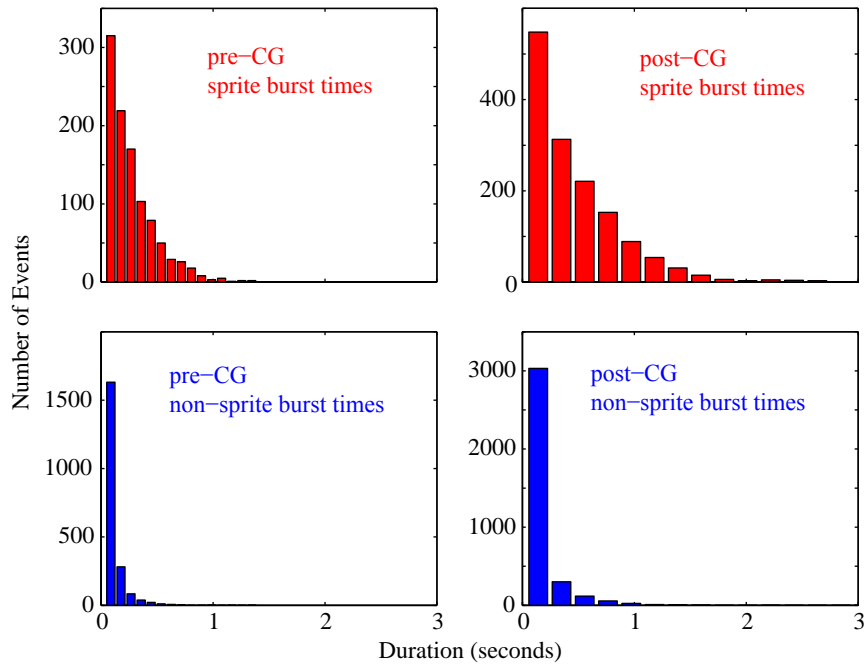


Figure 2.15: Distributions of durations of sferic bursts, for sprite- and non-sprite-related bursts, pre- and post-CG.

more prominent in events with associated sprites. While the total energy of the burst, as in Figure 2.14, is higher for sprite cases, this is in part due to the fact that the duration is longer.

2.3.3 In-cloud sources of VLF bursts

It has been speculated [*Johnson and Inan, 2000; van der Velde et al., 2006*] that these VLF sferic bursts are caused by in-cloud lightning activity. However, previously no convincing comparisons have been made between such VLF sferic bursts and measurements of in-cloud activity. This section shows correlations between sferic bursts and in-cloud activity, as measured by the New Mexico Tech LMA, deployed near the Colorado/Kansas border in the summer of 2000 [i.e., *Thomas et al., 2000*]. LMA data was not available for the other summers of sprite and VLF data discussed above.

Note that the “in-cloud” lightning activity referred to herein is actually most often the in-cloud horizontal component of CG discharges, rather than typical intracloud

lightning which never connects to the ground. Indeed, all of the cases analyzed in the previous section and in this section were associated with +CGs. As such, if the correlations outlined below hold, the results in Figure 2.14 can be interpreted as a measure of the horizontal in-cloud activity associated with the parent CG for each case. The term “in-cloud” is used for brevity, but it is important to note that the CG is still integral to the discussion.

Data from the LMA are established by the reception of a pulse at a minimum of six locations (four for 3-D location and time, and an extra two for redundancy and a measurement of uncertainty), and source locations are calculated using time-of-arrival (TOA) differences. Uncertainties for the three direction components at 200 km are ~ 60 m (azimuth), ~ 1500 m (range), and ~ 1500 m (altitude) [*Thomas et al., 2004*, Fig. 12]. Given that a 1.5 km uncertainty is far more significant for altitude (which usually ranges from 0–20 km), latitude/longitude positions are generally considered accurate for events within ~ 200 km from the LMA receivers, while altitudes are only considered accurate for events within ~ 100 km [*P. Krehbiel*, private communication, 2006].

Figure 2.16 shows an example of LMA data together with VLF and NLDN data for a sprite case. The LMA data shown here are the decimated data available through the New Mexico Tech website, which have a time resolution of 0.4 ms. This example clearly shows a strong correlation between LMA and VLF sferic burst data, as both show a distinct, continuous burst of activity lasting about 3.5 seconds.

LMA activity is observed during sprite times, although this part of the study does not account for sprite occurrence; these times are simply used for convenience, since the VLF data have already been compiled above. Of over 1000 sprites observed in the summer of 2000, when the LMA was operational, 373 sprite times had corresponding LMA data available. Of these, 154 correspond to storms within ~ 200 km of the LMA, where 2-D latitude/longitude data are reliable. Figure 2.16 shows a good example of the association between the LMA and the VLF burst activity. The color scale of the LMA data progresses from blue to red in time, so that pulses can be tracked in time on the corresponding map. Figure 2.17 shows another example with exceptional association.

In Figure 2.17, it is evident that the VLF sferic burst activity is almost perfectly correlated with the LMA data, even at times when no NLDN strokes were reported. Note specifically the burst from 5–6 seconds on this plot; no NLDN stroke was reported, but one must take into account the 85–90% efficiency of NLDN for +CGs. However, VLF data were analyzed for this time period from Palmer Station, Antarctica, and no sferics were found in this time period coming from the United States sector. This comparison shows that in-cloud activity, as measured by the LMA, can explain many cases of VLF sferic burst activity; and that in turn, the VLF sferic bursts can provide a measurement of in-cloud activity.

Note that since amplitudes of the individual LMA pulses are not available, quantitative rules for these correlations cannot be established. However, a metric has been created to attempt to quantify the association between the LMA data and the VLF activity. Taking into account only the 154 cases that are near enough to the LMA for data to be reliable, the following analysis is conducted:

VLF data are first rectified, then integrated in 100 ms time segments, to yield a time trace of VLF “energy” similar to those shown in *Johnson and Inan* [2000]. Next, LMA pulses are counted in 100 ms bins, creating a time histogram of LMA activity. Both of these traces are then normalized. The two normalized traces are shown in Figure 2.18 for the data in Figure 2.17. The middle five seconds (centered around the sprite time) of the traces are then cross-correlated; the peak of the cross-correlation, occurring at zero-lag, is recorded. The distribution of all of these peaks are shown in the bottom panel of Figure 2.18. For comparison, the correlation peaks for each of the example figures are shown in their respective captions. The relatively low correlation in Figure 2.17 (and 2.18) can be attributed to lack of amplitude data for the LMA, and thus the effect of simply counting the pulses, as can be seen by the discrepancy in amplitude around 5–6 and 8–9 seconds. For further comparison, correlations were calculated for the storm of 02 July 2000, occurring in South Dakota, some ~ 750 km from the LMA and ~ 600 km from Yucca Ridge, for each of about 400 sprites. At this range, the LMA would not be expected to receive many pulses from the storm. VLF burst activity was prominent in the data, and no other large storms occurred within 1000 km of the VLF receiver that might contribute to the sferic burst activity.

Results show a mean correlation peak of 0.53 with a standard deviation of 0.1. When compared with the distribution in Figure 2.18, this demonstrates that when the LMA data is reliable, it is undeniably associated with VLF sferic burst activity.

Further examination of the LMA activity leads to some insight into the nature of the VLF sferic bursts. Figure 2.19 shows an example including a zoomed-in view of the 2D latitude/longitude positions of the LMA pulses, using the undecimated data (80 μ s resolution). With the color scale fading from blue to red in time, it is apparent that from the time of the CG, LMA pulses were observed originating from progressively farther from the CG, fanning out where the red pulses are seen; this activity strongly resembles the “spider” lightning reported by *Mazur et al.* [1998]. The black dashed line shows where the sprite occurred as observed from Yucca Ridge, taking into account the ± 50 km uncertainty.

This example shows evidence that the LMA and VLF data are both recording signatures of the CG-associated in-cloud horizontal lightning activity. This in-cloud activity likely serves to tap the large positive charge reservoir of the convective system [Williams, 1998; Lyons et al., 2003]. In this way, the sferic burst activity is actually a signature of the processes by which large amounts of charge are removed from the thundercloud in a +CG, leading to a large charge moment change; and in turn, since sprites require large charge moment changes [e.g., Cummer and Inan, 2000], the VLF sferic burst can be interpreted as the signature of cloud processes that often lead to sprite occurrence. Furthermore, the statistics in Figure 2.12 show that sprite events have much longer sferic burst durations; this long duration in-cloud lightning activity could also be related to the large charge moment change through the long continuing current that has been associated with sprites [Reising et al., 1996]. In a similar vein, these longer duration sferic bursts most likely reach a greater distance into the cloud, and these longer channels will likely radiate stronger in the VLF, appearing as stronger sferic bursts. In this way the duration and the average power of these sferic bursts should be intertwined. Figure 2.20 shows a scatter plot of the sferic burst durations versus the average power in the sferic burst for all sprite-related cases in 2000. While the result is obviously quite noisy, one can discern a general trend that higher sferic burst power correlates with longer duration.

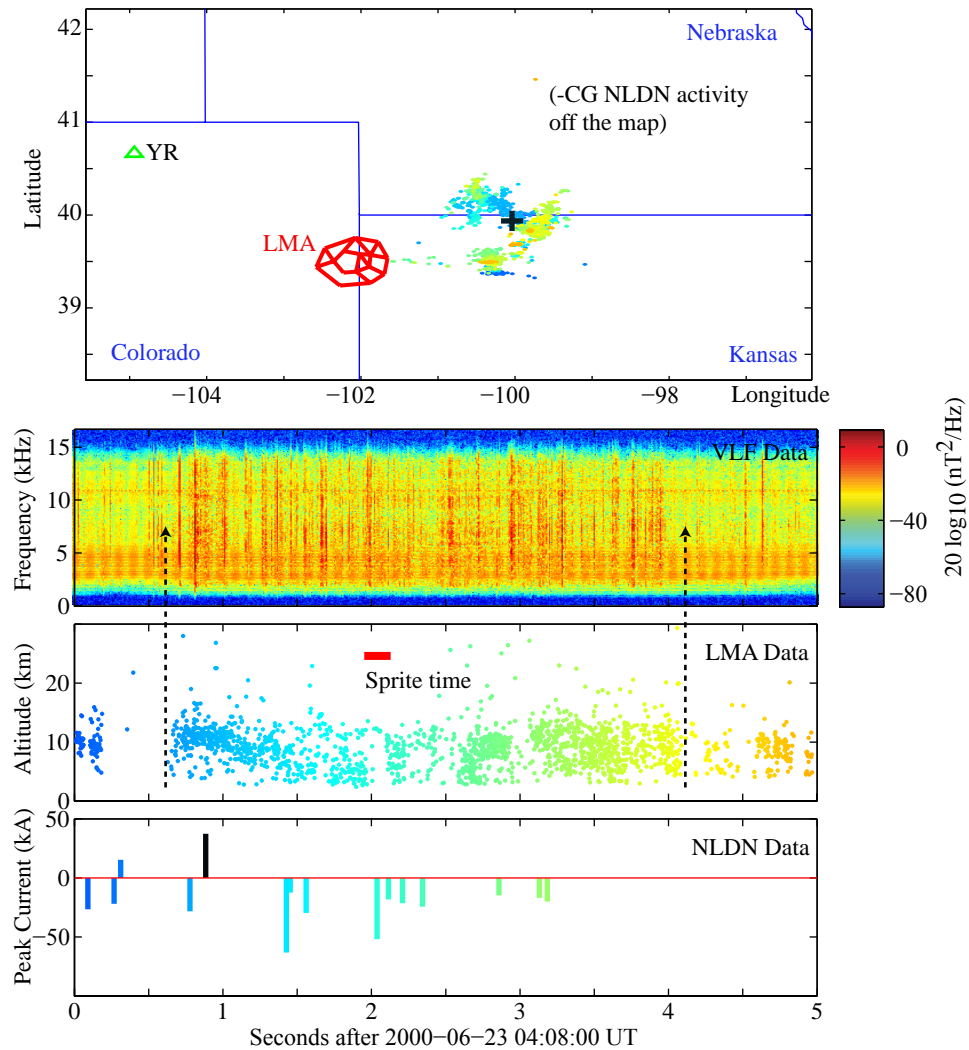


Figure 2.16: Example of VLF, NLDN and LMA data together for a sprite case. The large +CG (shown in black) caused a sprite halo at 04:08:00.908 UT, followed by a sprite at 04:08:01.108 UT; VLF data shows the causative sferic, as well as burst activity lasting about 3.5 seconds. LMA data during the same time and location corroborates the 3.5 second period of in-cloud activity. This example has a correlation peak (described in the text) of 0.863. In this case, the NLDN -CG activity was off the map shown.

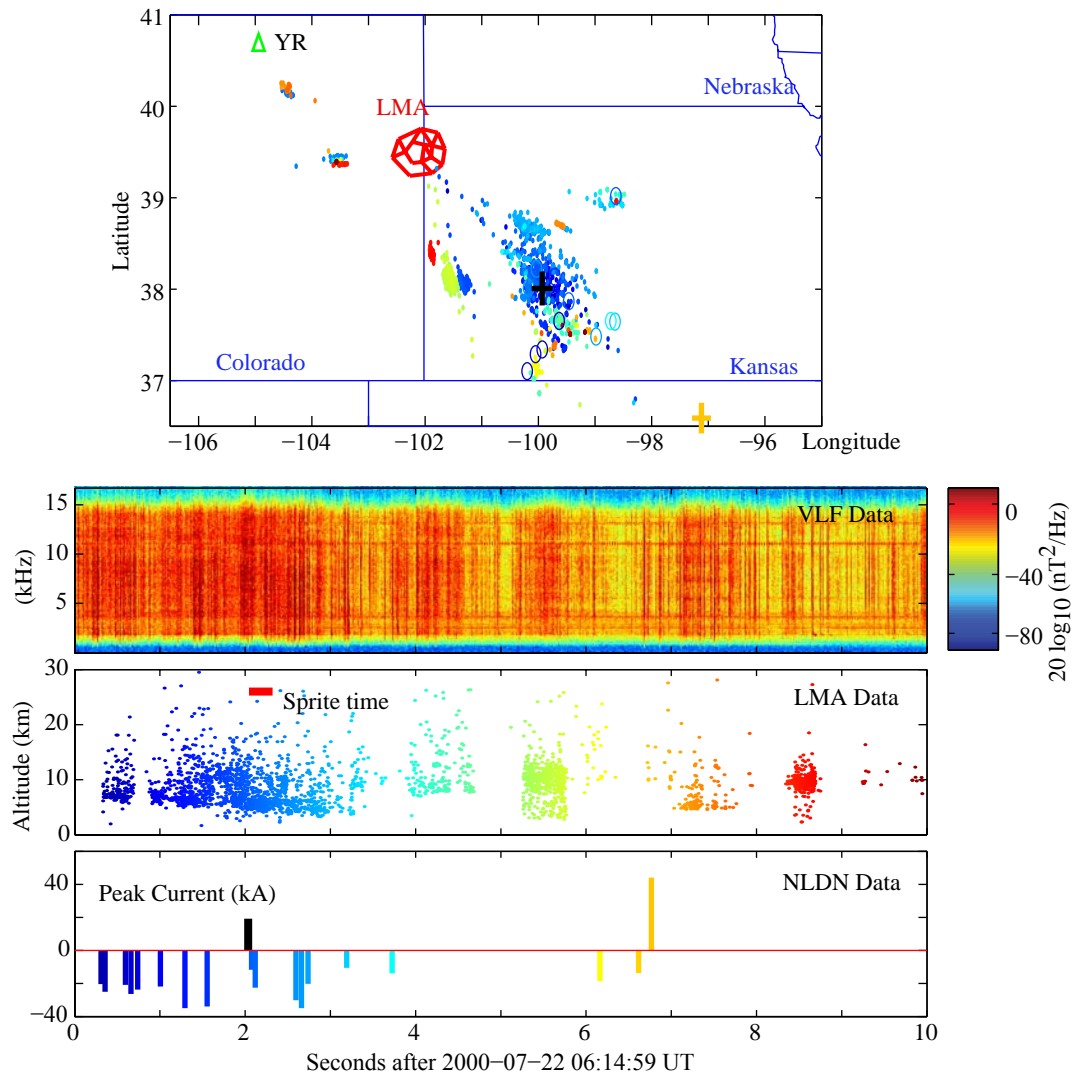


Figure 2.17: A second example of VLF, NLDN and LMA data together for a sprite case. In this case the correlation between VLF and LMA data is very strong, even explaining VLF activity where there is no NLDN (seconds 5–6). On the map, $-CG$ discharges are shown as circles. This example has a correlation peak of 0.688.

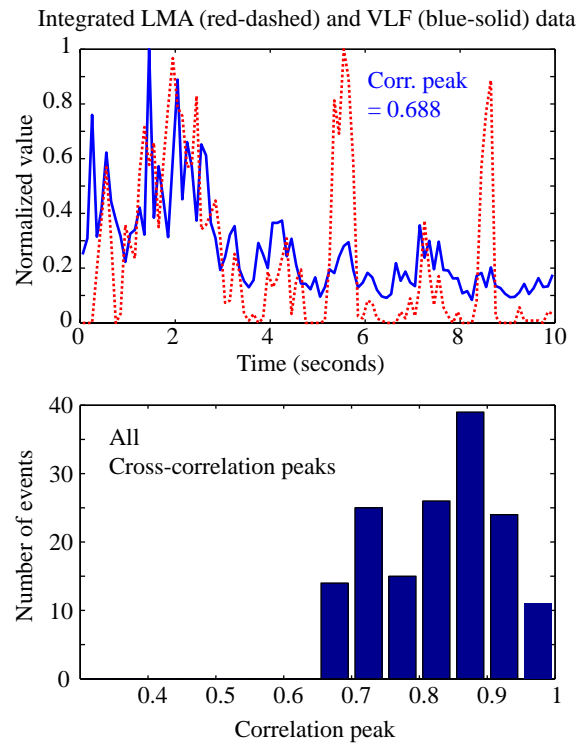


Figure 2.18: Top: normalized running integrals of VLF and LMA data from Figure 2.17. Bottom: histogram of correlation peaks for the dates discussed in the text. Note that for the case shown, the correlation peak is weak, despite the visual correlation; this is possibly due to the lack of amplitude data with which to scale the LMA integration.

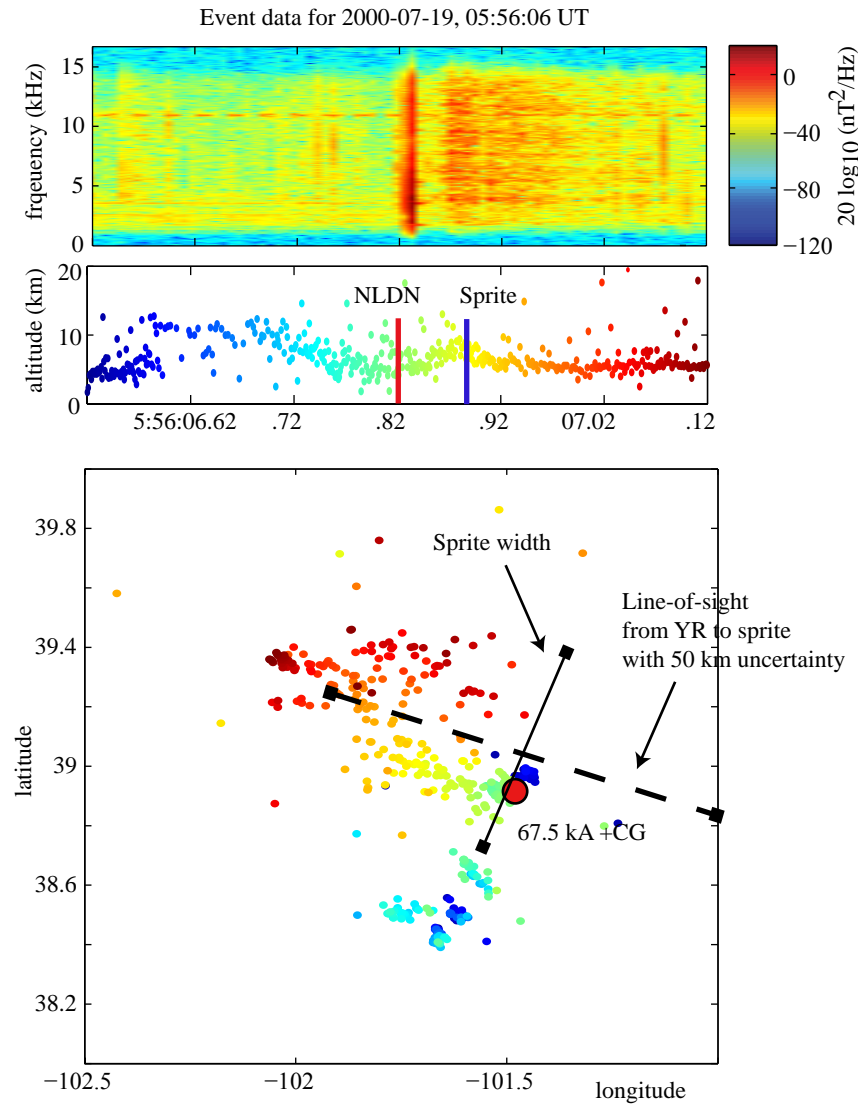


Figure 2.19: An example of LMA and VLF sferic burst data demonstrating the tendrillike structure of the in-cloud lightning. This example has a correlation peak (described in the text) of 0.824.

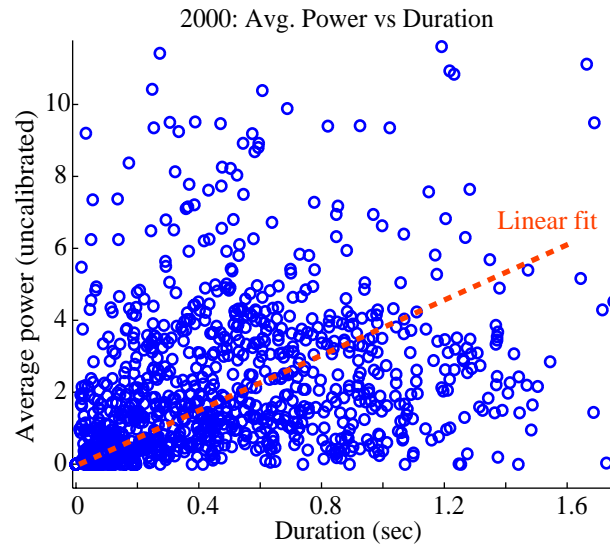


Figure 2.20: Sferic burst average power versus burst duration. A weak trend exists where bursts of longer duration have higher average power, possible evidence that longer duration bursts have longer channels and thus radiate stronger at VLF frequencies.

In-cloud processes leading to Sferic Bursts

The sferic burst data presented here gives some insight into the types of in-cloud activity detected by VLF methods. *Proctor et al.* [1988] showed the differences between “pulses” and “Q-noise” in lightning, having durations of $1 \mu\text{s}$ and $40\text{--}400 \mu\text{s}$ respectively. *Mazur et al.* [1997] showed that Time-of-Arrival (TOA) detection systems for VHF activity are more sensitive to the individual fast pulses, while Interferometric (ITF) detection systems are more sensitive to the long-duration Q-trains. Furthermore, *Mazur et al.* [1997] showed that the Q-trains, as detected by ITF, occur at altitudes significantly lower than pulses, with means of 5 km and 9 km respectively. Note that spider lightning, often thought to be active in sprite initiation [e.g., *Stanley, 2000*], occurs at altitudes of 4–6 km [*Lyons et al., 2003*]. The LMA, used in this study, is a TOA system.

Recently it has been shown that the LMA can often observe impulsive components following CG discharges [*Shao and Krehbiel, 1996; Thomas et al., 2004*]. The example in Figures 1 and 2 of *Thomas et al.* [2004] shows how the LMA can detect

in-cloud components of CG discharges, of precisely the type of dendritic structure thought to be responsible for continuing currents [Reising *et al.*, 1996]. In *van der Velde et al.* [2006], an interferometric SAFIR system was used, which has a $100 \mu\text{s}$ resolution [van der Velde *et al.*, 2006, and references therein], and it was noted that the activity reported by the SAFIR system did not correlate well with the VLF sferic burst activity.

Mazur et al. [1998] notes that spider lightning is often luminous for hundreds of milliseconds, due to continuing current; it is likely that the radio emissions from this continuing current are what is measured by the VLF receiver. The coincident observations from the LMA are evidence of fast leader processes also occurring over hundreds of milliseconds. It is possible, then, that sprite-producing “spider” lightning does not exhibit the Q-train type of pulses that are well mapped by interferometric systems such as SAFIR.

2.3.4 Summary

Bursts of radio activity observed in VLF data almost always accompany the parent CG lightning of sprites. However, many non-sprite-producing +CGs are also accompanied by sferic burst activity, so that sferic burst activity does not provide a unique identifier for sprites. The correlation between sprites and sferic burst activity shows that the in-cloud component of the cloud-to-ground lightning discharge has a significant role in sprite production. Note that the CG component of the discharge is still a requirement for sprite production; no sprites have been confirmed without an associated CG preceding the sprite. It may thus be that in-cloud activity is responsible for enhancing the QE field above the thundercloud, raising it above the breakdown threshold and causing a sprite to occur that would not have otherwise. This scenario is most likely if the in-cloud activity acts to tap the positive charge reservoir of the cloud and enhance the charge moment through continuing current.

Figure 2.21 shows a scatter plot of sferic burst energy versus the peak current of the sprite-causative CG. The trend is evident: in the sferic energy (red circles), a clear slope shows that there are no cases of large peak currents with small sferic

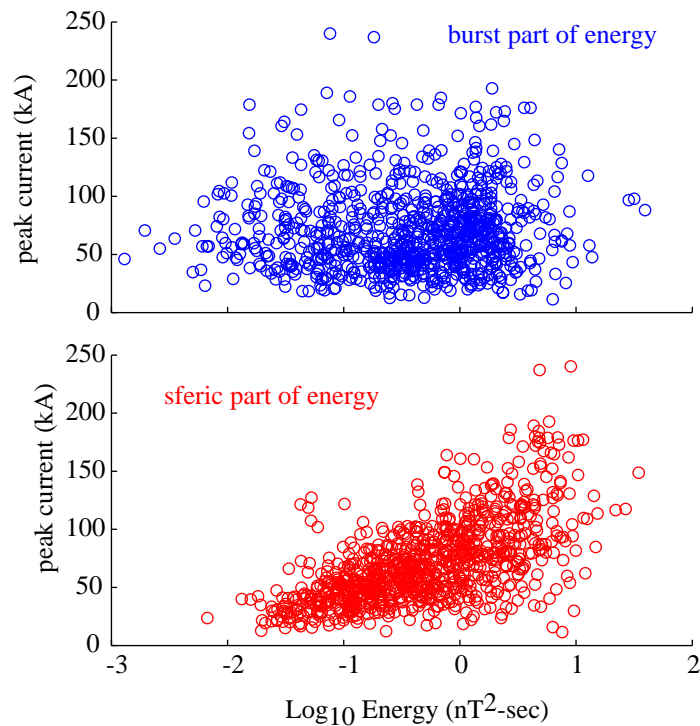


Figure 2.21: Peak currents versus sferic and sferic burst energy. For the sferic, a trend appears that disallows large peak currents with small energy; however, in the sferic burst cases, large peak currents may be accompanied by small sferic burst energy, showing that for larger discharges, sferic burst energy is not required to initiate a sprite (though charge moment is still very important).

burst energy. But in the energy content of the sferic burst (blue circles), such cases do occur. It thus appears that the larger peak current strokes (which presumably, and statistically, have larger charge moments) do not always *require* large sferic bursts (i.e., in-cloud activity) for sprites to occur. Or, viewed conversely, small peak current strokes, when accompanied by sferic burst activity, can produce sprites. The non-sprite-producing cases (not shown) show the same trend in both the sferic and sferic burst parts of the energy distributions.

The comparison of VLF sferic burst examples with LMA data shows a strong correlation and thus evidence that these VLF sferic bursts are indeed signatures of horizontal in-cloud lightning activity. Given the arguments above – that this in-cloud

lightning activity, when associated with a +CG, constitutes the in-cloud component of continuing current that taps the positive charge reservoir, leading to larger charge moments – we conclude that these sferic bursts provide an identifier for large charge moment cloud-to-ground lightning strokes, and thus a good but imperfect measure of sprite occurrence without optical observations.

2.4 Sferic Bursts and Early VLF

The correlation between sferic bursts and Early/fast events was studied extensively by *Johnson and Inan* [2000] and *Johnson* [2000]. A summary of that work is described here to “complete the triangle” of correlative studies between sprites, Early VLF events, and sferic bursts.

The study in *Johnson and Inan* [2000] was prompted by the lack of observation of Early/fast events for 10 NLDN peak currents of at least 64 kA, despite their location on Great Circle Paths to the HAIL array of VLF receivers. In addition, a number of Early/fast events were observed without any NLDN-located causative stroke. While it is possible that NLDN missed some of these CG strokes, *Johnson* [2000] attributed these missed strokes to IC lightning, which would not have been reported by NLDN. Upon further investigation, intense “sferic clusters” (“sferic bursts” in this work) were observed at the time of these Early/fast events. Now, most of the observed Early/fast events did have associated NLDN CG strokes, and it was found that they were not well correlated with peak current, as observed earlier by *Inan and Rodriguez* [1993]. Over the summer of 1998, it was shown that Early/fast events were only observed in association with those lightning events that included significant sferic burst energy.

Of course many more in-cloud lightning events occur that do not have associated Early VLF events. After measuring the sferic cluster intensity, [*Johnson, 2000*, Fig. 3.5] showed that Early/fast events are consistently associated with those sferic clusters with the highest intensity. Examples of sferic bursts with a series of eight Early/fast events from *Johnson and Inan* [2000] is shown in Figure 2.22.

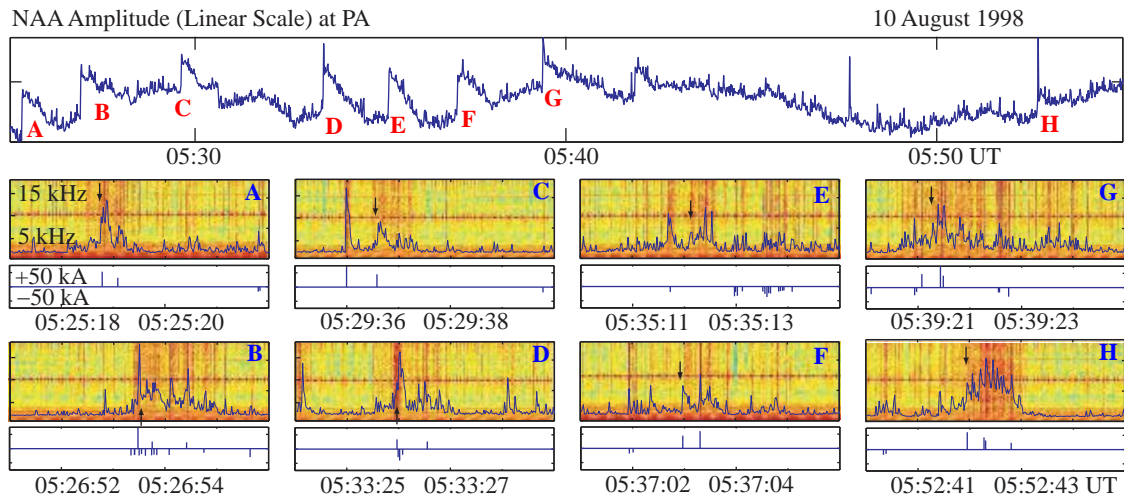


Figure 2.22: Correlations between Early/fast events and sferic bursts, from *Johnson and Inan* [2000]. In this study, every Early/fast event observed had associated sferic burst activity.

2.5 Early VLF Caused by In-cloud EMP pulses

The correlations between sprites, Early/fast events, and sferic bursts are summarized in Figure 2.23:

1. *Johnson and Inan* [2000] demonstrated that Early/fast events are exclusively associated with those lightning events that included significant sferic burst energy. These sferic bursts were conjectured by *Johnson and Inan* [2000] to be the signature of in-cloud lightning; this conjecture was verified through quantitative correlations with LMA data in *Marshall et al.* [2007].
2. *Marshall et al.* [2006] showed that for three summers of events, 48% of sprites had associated Early VLF events, while 61% of Early VLF events had associated sprites. It was also shown that Early VLF events can occur with and without halos. Since sprites and halos are well understood to be triggered by the QE field from lightning charge moment changes, this shows that the QE field cannot alone be the source of all Early VLF events. It must be recognized, however, that the QE field can also be responsible for Early VLF events, as shown by

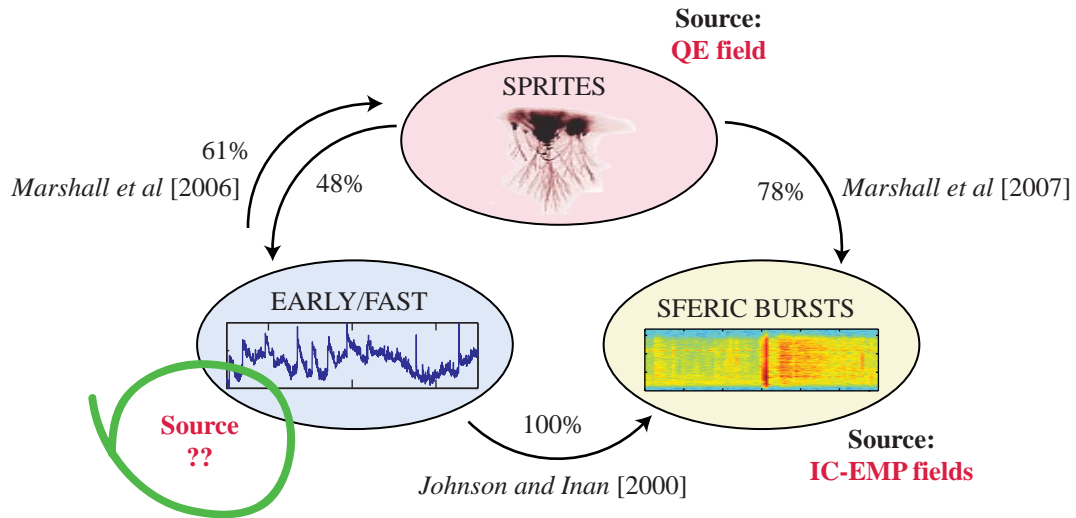


Figure 2.23: Summary of correlations between sprites, Early VLF events, and sferic bursts.

Barrington-Leigh et al. [2001] and *Moore et al. [2003]*, when the field is intense enough to cause ionization.

3. *Marshall et al. [2007]* showed that sprites are most often (78% of the time) associated with sferic burst activity, but the remaining 22% of sprites occur without sferic burst activity. This result comes as no surprise: the in-cloud lightning activity that is measured as sferic bursts serves to tap the thundercloud of charge, increasing the cumulative charge moment change of the CG, and in turn enhancing the QE field that initiates a sprite. Hence, larger burst activity is likely associated with larger charge moment changes, though this connection has yet to be studied. In the cases where no burst activity occurs, the impulsive charge moment change may have been sufficient for sprite initiation.

The second and third correlations demonstrate that the QE field cannot be solely responsible for all Early VLF events. The first correlation, from *Johnson and Inan [2000]*, leads to the idea that in-cloud lightning activity may be somehow responsible

for, or contribute to, the production of Early/fast and Early/slow events. This conclusion was first made by *Haldoupis et al.* [2004], who, as described earlier, suggested that sprite-related QE fields create “seed” electrons, which are subsequently accelerated by the in-cloud EMP fields to create secondary ionization. The conclusions of the second correlation from *Marshall et al.* [2006] create problems for this mechanism, since so many Early VLF events are found without sprites associated.

Given the full picture of Figure 2.23, a new mechanism is proposed in this work, in which the EMP fields from in-cloud lightning components *directly* modify the overlying ionosphere. In a series of such pulses over 1–3 seconds, corresponding to the duration of the sferic bursts described in Section 2.3, a cumulative change in the ionospheric density results, evidenced by a slowly increasing perturbation to the VLF transmitter signal, as exhibited by Early/slow events. In cases where the burst activity happens over a short time period, or where the sferic burst appears as sferic intrusion in the VLF narrowband data, these would be exhibited and categorized as Early/fast events.

The next two chapters test this hypothesis. In Chapter 3, a Finite-Difference Time-Domain (FDTD) model is employed to quantify the electron density changes in the lower ionosphere due to realistic cloud-to-ground and in-cloud lightning events. Chapter 4 uses a Finite-Difference Frequency-Domain (FDFD) model of the VLF transmitter signal propagation to measure the scattered VLF signal due to these density changes.

Chapter 3

Modeling the Lightning EMP

The purpose of this chapter is to model the lightning Electromagnetic Pulse (EMP) interaction with the lower ionosphere. For this purpose a 3D Finite-Difference Time-Domain (FDTD) model is used, which solves for the electric and magnetic fields and currents self-consistently in the time domain. Section 3.1 presents a brief history of the approach to this problem. The model formulation is presented in Section 3.2, and results for a wide variety of parameters are cataloged in Section 3.3. Section 3.4 summarizes the major results of this chapter.

3.1 Previous Work

Inan et al. [1991] was the first to model the lightning EMP interaction with the lower ionosphere, and used thermal heating of electrons to predict the effects on the ionosphere, including optical emissions. This model yielded the first prediction of observable optical emissions that would later come to be known as “elves”. *Taranenko et al.* [1993a,b] presented a new model of the lightning EMP–ionosphere interaction, wherein an electric field pulse was propagated vertically through 70–100 km altitude, and ionization, attachment, and optical emissions were calculated kinetically. These models were both 1D, and so were not able to predict the shape of elves. The 2D cylindrically-symmetric model of *Inan et al.* [1996c] demonstrated the ring-shape of elves and attributed it to the far-field radiation pattern of a vertical current on the

ground; as mentioned in Chapter 1, this ring shape was then confirmed in camera observations, and in the Fly’s Eye photometric observations [Inan *et al.*, 1997]. The 2D model of Veronis *et al.* [1999] and Barrington-Leigh [2000] extended the Inan *et al.* [1996c] model to include effects of the quasi-electrostatic field, and found that heating effects of the QE field led to the observed emissions known as sprite halos.

Other 2D models [Rowland *et al.*, 1995, 1996; Cho and Rycroft, 1998] of the EMP-ionosphere interaction were employed in the early years of sprite observations to attempt to explain the shape of sprites, rather than elves. Rowland *et al.* [1996] was the first to attempt to simulate horizontal currents in a so-called “2-1/2 D” model. The first 3D model was presented by Cho and Rycroft [2001] in an attempt to simulate in-cloud lightning and its effect on the ionosphere. However, those models did not utilize realistic in-cloud currents. Similar to Barrington-Leigh [2000], Kuo *et al.* [2007] modeled the optical emissions from elves in 3D and compared the results to observations on the ISUAL satellite instrument [Chern *et al.*, 2003]. Finally, Nagano *et al.* [2003] modeled the EMP-ionosphere interaction using full-wave methods, which do not inherently treat the ionospheric density change, but did include the effect of the Earth’s magnetic field, predicting asymmetry in the elve emissions.

3.2 The 3D EMP Model

The present 3D model is designed to simulate two effects that cannot be observed in 1D or 2D models. First, the presence of the Earth’s magnetic field may create an asymmetry in observed elves, though it is expected to play a minor role; however, observations suggest that this asymmetry may be observable. Second, the desire to quantify the effects of in-cloud lightning on the lower ionosphere requires a 3D model. In a cartesian 2D model, the simulated current would be infinite in the third dimension, thus simulating an unrealistic “infinitely long wire” source current. The model herein inherently updates the ionospheric electron density, unlike the full-wave model of Nagano *et al.* [2003], includes the Earth’s magnetic field, and is able to simulate realistic in-cloud lightning pulses.

The Finite-Difference Time-Domain (FDTD) method is used to simulate the propagation of EMP pulses and their interaction with the lower ionosphere. The simulation space is shown in Figure 3.1. The space is cartesian and extends 500 km in the x and y directions, and from as low as 50 km to as high as 195 km in altitude; these altitudes are easily adjustable. For the simulations shown in this work, the altitude range of 60–185 km is used, and the grid has units cells of $(\Delta x, \Delta y, \Delta z) = (2, 2, 0.8)$ km, and $\Delta t = 0.025 \Delta z / c$. This choice of Δt ensures stability for phase velocities v_p as low as $\sim c/25$; these simulations typically have $c \geq v_p \geq c/10$.

The model uses a simple second-order Mur absorbing boundary condition (ABC) on the lower boundary at 60 km to absorb waves reflected from the lower ionosphere back toward the lower boundary. The sides and top of the simulation space do not have ABCs, and are instead placed far enough from the source that reflections do not affect the results during the time of observations. In an anisotropic medium such as a magnetized plasma, phase and group velocity vectors can have anti-parallel components into and out of the boundary, which causes some forms of ABC to amplify, rather than absorb, incident waves; this phenomenon is described in full in *Chevalier et al.* [2008]. We place the boundaries far enough from the source to avoid such problems, but at the expense of computational time and memory.

The source fields at the 60 km lower boundary are calculated analytically at each time step and used as an “input” to the model. This procedure reduces the size of the computation space and eliminates the finite current channel size of direct current sources; i.e., with 2 km resolution in x and y , the smallest current source that could be simulated would be 2×2 km square in its x – y cross section. The equations to solve at the boundary are the radiation equations for a small dipole, found in many textbooks, but typically written in the frequency domain for a z –directed current. In the formulation herein, the time domain versions of these equations are used, which

are derived from the Hertz dipole vectors in [[Budden, 1961](#), p. 43]:

$$E_r = \frac{1}{2\pi\epsilon_0} \sin \theta \left(\frac{[M]}{r^3} + \frac{1}{cr^2} \frac{\partial[M]}{\partial t} \right) \quad (3.1)$$

$$E_\theta = \frac{1}{4\pi\epsilon_0} \cos \theta \left(\frac{[M]}{r^3} + \frac{1}{cr^2} \frac{\partial[M]}{\partial t} + \frac{1}{c^2 r} \frac{\partial^2[M]}{\partial t^2} \right) \quad (3.2)$$

$$H_\phi = \frac{1}{4\pi\epsilon_0} \cos \theta \left(\frac{1}{cr^2} \frac{\partial[M]}{\partial t} + \frac{1}{c^2 r} \frac{\partial^2[M]}{\partial t^2} \right) \quad (3.3)$$

$$E_\phi = H_r = H_\theta = 0$$

where $[M]$ denotes the “retarded” value of the dipole moment M , $d\mathbf{M}/dt = i\mathbf{l}$, and i and \mathbf{l} are the current magnitude and current channel vector respectively; thus for a given $M(t)$, $[M] = M(t - r/c)$.

To solve for a dipole of arbitrary orientation (x , y and z components), these equations are simply solved for each component, and for the x and y components a coordinate rotation is applied to the results. For the simulations presented here, the current is modeled by $I(t) = I_0 \cosh^{-1}[\alpha(t - t_0)]$, where I_0 is the amplitude in kA, the parameter α controls the temporal width of the current pulse, and t_0 is chosen so that the pulse ramps up smoothly from zero to the maximum value.

3.2.1 Update Equations

The EMP model self-consistently solves Maxwell’s Equations and the Langevin Equation [[Bittencourt, 2003](#), p. 239]:

$$\nabla \times \vec{E}_w = -\mu_0 \frac{\partial \vec{H}_w}{\partial t} \quad (3.4)$$

$$\frac{\partial \vec{J}}{\partial t} + \nu_e \vec{J} = \epsilon_0 \omega_p^2 \vec{E}_w + \vec{\omega}_b \times \vec{J} \quad (3.5)$$

$$\nabla \times \vec{H}_w = \epsilon_0 \frac{\partial \vec{E}_w}{\partial t} + \vec{J} \quad (3.6)$$

where the subscript w is used to denote the wave electric and magnetic fields (in contrast to the Earth’s static magnetic field \mathbf{B}_0); $\omega_p = \sqrt{N_e q^2 / m_e \epsilon_0}$ is the electron plasma

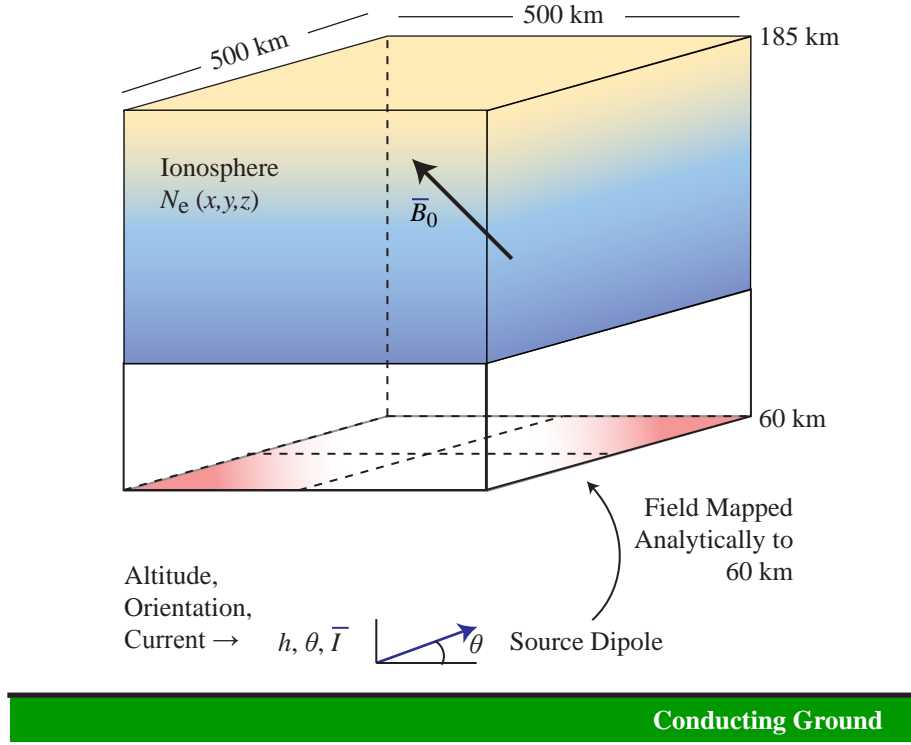


Figure 3.1: Simulation space used in the EMP model. Fields are calculated analytically at the lower boundary for an arbitrarily-oriented dipole, and then propagated into the simulation space using Equations 3.4–3.6.

frequency for an electron density N_e , $\omega_b = q_e \mathbf{B}_0 / m_e$ is the electron gyrofrequency, and ν_e is the effective electron collision frequency with air molecules. Equation (3.5) is the equation of motion for electrons; its full form is given by [Bittencourt, 2003, p. 202]:

$$N_e m_e \left[\frac{\partial \vec{v}}{\partial t} + (\vec{v} \cdot \nabla) \vec{v} \right] = \nabla \cdot p + N_e q_e (\vec{E}_w + \vec{v} \times \vec{B}) + N_e m_e \vec{g} - \nu_e N_e m_e \vec{v} + \vec{v} S \quad (3.7)$$

but is reduced to the form given in Equation (3.5) with the following approximations:

- $(\vec{v} \cdot \nabla) \vec{v}$ is the convection term, due to gradients in the electron velocity. It can be ignored when average (i.e., bulk) velocity is small;
- $\nabla \cdot p$ is due to gradients in electron pressure: it is negligible in a cold plasma (at

90 km, $T_e \simeq 180$ K);

- $N_e m_e \vec{g}$, the force on electrons due to gravity, is negligible in comparison with the electromagnetic forces;
- $\vec{B} = \vec{B}_w + \mathbf{B}_0$, the wave magnetic field plus the Earth’s ambient magnetic field; but B_0 is on the order of μT , while for $\vec{E} \sim 20$ V-m $^{-1}$, $\vec{B}_w \sim nT$. Hence it can be approximated that $\vec{B} \simeq \mathbf{B}_0$;
- The term $\vec{v}S$ is the momentum transfer due to creation or destruction of particles, and is usually ignored.

These simplifications are equivalent to the linearization procedure in which terms quadratic in velocity \vec{v} and wave magnetic field \vec{B}_w are ignored. Ultimately, with these simplifications Equation (3.7) reduces to:

$$N_e m_e \frac{\partial \vec{v}}{\partial t} = N_e q_e (\vec{E}_w + \vec{v} \times \mathbf{B}_0) - \nu_e N_e m_e \vec{v} + \vec{v}S \quad (3.8)$$

Finally, note that $N_e q_e \vec{v} = \vec{J}$, and Equation (3.5) follows.

Equations (3.4) to (3.6) are discretized with second-order centered-differencing in time and space. Equation (3.5) is discretized using a modified version of the so-called “TRISTAN” algorithm presented by [Buneman \[1993\]](#). In this algorithm, the solution of Equation (3.5) is separated into the “natural” and “forced” components, and the forces on the right are labeled “acceleration” (the $\epsilon_0 \omega_p^2 \vec{E}$ term) and “rotation” (the $\omega_b \times \vec{J}$ term). The details of the modified [Buneman \[1993\]](#) algorithm are presented in Appendix A.

3.2.2 Collision Frequency

The nighttime ionosphere has an electron density that increases exponentially with altitude beginning around 65 km. At this altitude and above, the electron mobility μ_e dominates the overall conductivity of the ionosphere, which is given by $\sigma = q_e N_e \mu_e + \sum_{\text{ions}} q_i N_i \mu_i$. Typical electron densities as a function of altitude are shown in Figure 3.2, along with atmospheric density versus altitude. In most of the simulations in

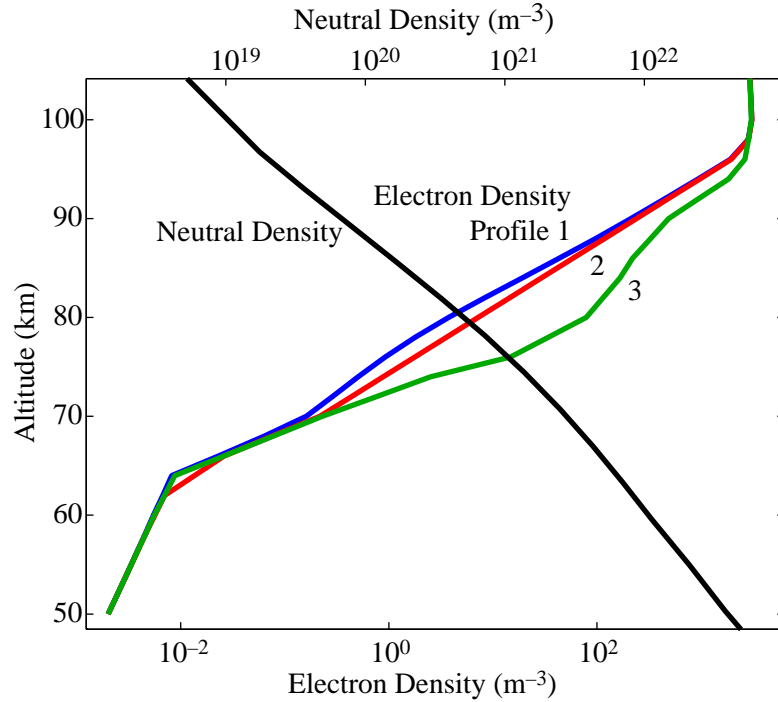


Figure 3.2: Typical ionospheric electron density and neutral density profiles; adapted from [Pasko and Inan \[1994\]](#).

this work profile #2 is used, but the effects of different electron density profiles are also investigated later.

The presence of collisions (ν_e) and the Earth’s magnetic field ($\vec{\omega}_b = q_e \mathbf{B}_0 / m_e$) in Equation (3.5) both modify the electron motion in the presence of the wave electric field \vec{E}_w . Electrons and ions are confined to gyrate around Earth’s magnetic field lines with angular frequency ω_b , except when the collision frequency ν_e becomes comparable to or larger than ω_b , in which case the gyro-motion becomes regularly interrupted. The “effective electric field” of the incident wave that is applied to these confined electrons can be approximated, in phasor form, by [[Gurevich, 1978](#), p. 75, equation 2.169]:

$$E_{\text{eff}}^2 = E_{\parallel}^2 + (\omega^2 + \nu^2) \left[\frac{E_{\perp-}^2}{(\omega - \omega_b)^2 + \nu^2} + \frac{E_{\perp+}^2}{(\omega + \omega_b)^2 + \nu^2} \right] \quad (3.9)$$

where E_{\parallel} is the component of the wave electric field parallel to \mathbf{B}_0 , $E_{\perp-}$ and $E_{\perp+}$ are the perpendicular components of the electric field which rotate with and against

the electron gyromotion, and ν is a kinetically-calculated effective collision frequency [Glukhov and Inan, 1996]. In the simulations described here, the frequency ω (≤ 100 kHz) is always much less than the gyrofrequency ω_b (~ 0.7 – 1.8 MHz at 100 km altitude, depending on latitude), so that Equation (3.9) reduces to

$$E_{\text{eff}}^2 = E_{\parallel}^2 + E_{\perp}^2 \frac{\nu^2}{\nu^2 + \omega_c^2} \quad (3.10)$$

Note that Equation (3.10) is independent of frequency. Electron motion is also damped by collisions with neutrals, given by the second term in Equation (3.5). The rate of collisions between electrons and neutrals is given by $\nu_e = q_e/(\mu_e m_e)$, where μ_e is the electron mobility. Laboratory data on electron swarms from Davies [1983] demonstrate that the mobility is a nonlinear function of the reduced electric field E_{eff}/N , where in this case E_{eff} is the magnitude of the “effective” electric field calculated above. The data from Davies [1983] and the analytical fit used herein are shown in Figure 3.3. This analytical fit is given by the expression

$$\log(\mu_e N) = \sum_{i=0}^2 a_i x^i \quad \text{where} \quad x = \log(E_{\text{eff}}/N) \quad (3.11)$$

and the coefficients are $a_0 = 50.970$, $a_1 = 3.0260$, and $a_2 = 8.4733 \times 10^{-2}$ [Pasko, 1996]. The mobility takes a maximum value of $1.36 N_0/N \text{ m}^2\text{-V}^{-1}\text{-s}^{-1}$ in the thermal limit, i.e. for small applied fields. In our model the mobility is updated self-consistently at each point in time and space as the fields propagate.

3.2.3 Ionization and Attachment

Ionization occurs when an electron with sufficient energy collides inelastically with a neutral molecule and creates an extra free electron. In the atmosphere dominated by nitrogen and oxygen, ionization can be characterized by the reaction $M_2 + e^- + \text{energy} \rightarrow M_2^+ + 2e^-$, where M_2 represents either N_2 or O_2 , and the energy required for ionization is 12.06 eV for oxygen or 15.60 eV for nitrogen [Moss et al., 2006]. The number of ionization events that occur in a volume of air per unit time depends on

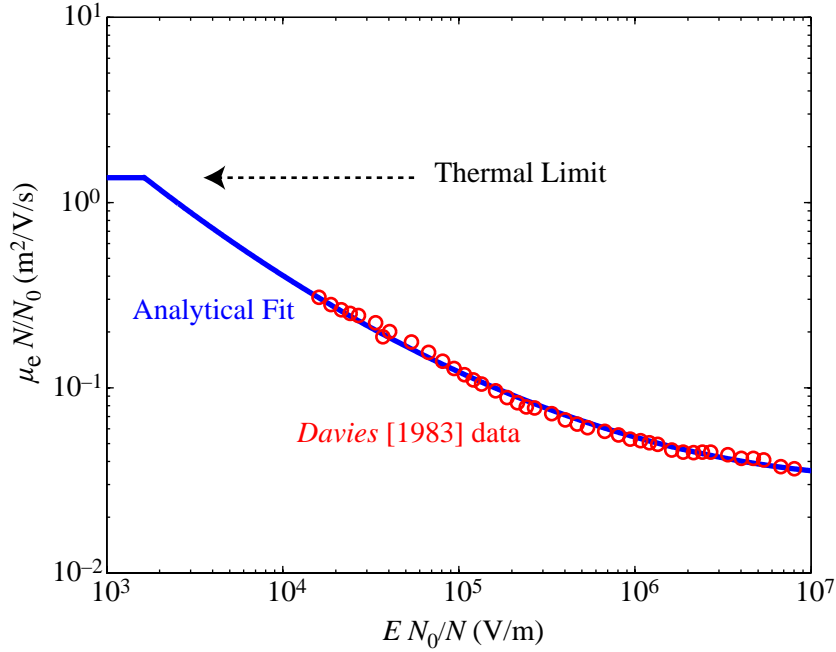


Figure 3.3: Electron mobility in air as a function of reduced electric field; determined from fits to data in *Davies* [1983].

the reduced electric field E_{eff}/N .

The results of laboratory experiments and numerical models, yielding the ionization rate ν_i as a function of reduced electric field, are summarized in Figure 3.4. *Davies* [1983] presents results of laboratory swarm experiments for a range of electric fields. *Papadopoulos et al.* [1993] gives an analytical fit to kinetic calculations. In *Moss et al.* [2006], kinetic calculations are presented using a numerical solution to the electron distribution function (using the ELENDIF code; see *Morgan and Penetrante* [1990]) and Monte Carlo simulations, and these are compared to ionization rates given by *Aleksandrov et al.* [1995]. In this work we use the analytical expression given by *Papadopoulos et al.* [1993]:

$$\nu_i = 7.6 \times 10^{-13} N x^2 f(x) e^{-4.7(\frac{1}{x}-1)} \quad (3.12)$$

where

$$f(x) = \frac{2}{3}(1 + 6.3 e^{-2.6/x}) \quad \text{and} \quad x = E_{\text{eff}}/E_k \quad (3.13)$$

The breakdown field E_k in $\text{V}\cdot\text{m}^{-1}$ is given by [Papadopoulos *et al.*, 1993]:

$$E_k = 32 \times 10^5 \frac{N}{N_0} \sqrt{1 + \frac{\omega^2}{(1.6 \times 10^{-13} N)^2}} \quad (3.14)$$

with $N_0 = 2.688 \times 10^{25} \text{ m}^{-3}$. Note that the breakdown field depends on frequency; for the results described here, the number density $N \simeq 10^{19} \text{ m}^{-3}$ at 100 km altitude (the highest altitude of interest; see Figure 3.2), and the term under the square-root sign can be ignored for all frequencies below 500 kHz. Note that at 90 km altitude, $N \simeq 7 \times 10^{19} \text{ m}^{-3}$, and the breakdown field is $E_k \simeq 8.3 \text{ V}\cdot\text{m}^{-1}$.

When using the ionization rates of Papadopoulos *et al.* [1993] it is important to recognize that in that work, the authors dealt with high frequencies and the source fields were assumed to be sinusoidally-varying. Thus, the E -field that appears in the above expressions refers to the RMS field values. For low frequency (i.e., quasi-DC) fields, we are interested in the actual applied field amplitude, and so we must multiply the rates by a factor of $\sqrt{2}$. Otherwise, the ionization curve is shifted in E to the right by this factor, and the relative contributions of ionization (compared to dissociative attachment and optical emissions) are significantly altered. The lower ionization rate was used by Taranenko *et al.* [1993a,b] and Pasko *et al.* [1997]; in those results, the density changes may have been underestimated due to these lower ionization rates. Conversely, those results required larger peak currents or charge moment changes to produce the same results; the results herein require smaller inputs to achieve the same results. However, since the ionization rate is increased but attachment is not, those prior results also exhibit a more significant effect of attachment; in the model herein, the window of electric fields where attachment can occur, before it is overwhelmed by ionization, is considerably smaller.

Electrons are removed via dissociative attachment to molecular oxygen, given by the reaction $\text{O}_2 + \text{e}^- + 3.7 \text{ eV} \rightarrow \text{O} + \text{O}^-$. The attachment rate similarly depends on the reduced electric field E_{eff}/N . Figure 3.4 shows rates from a number of sources. Davies [1983] again provides rates determined from electron swarm experiments, while Pasko *et al.* [1997] provides empirical fits to this data. We use the analytical form

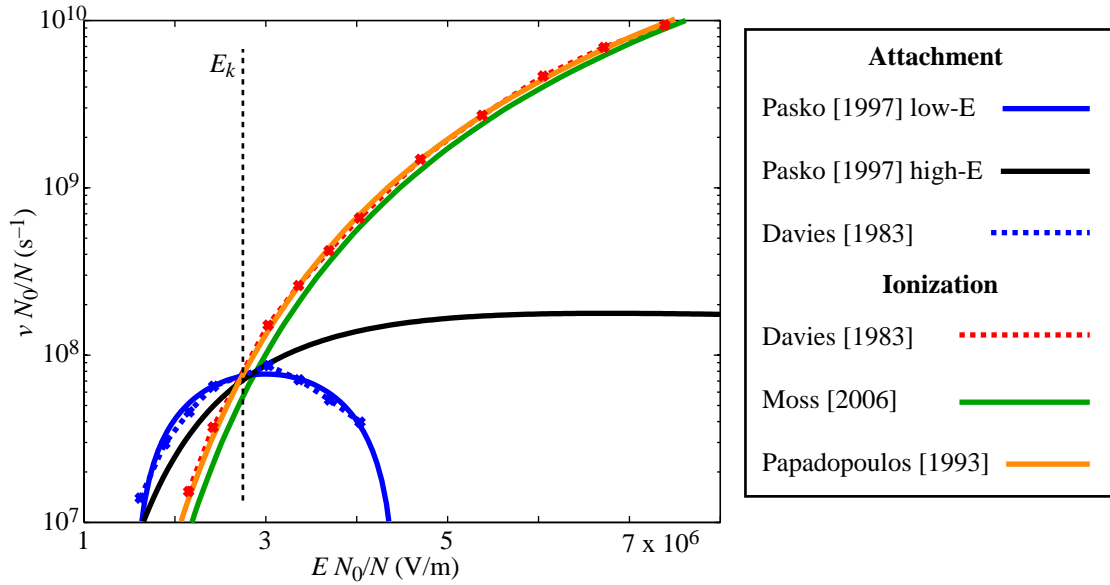


Figure 3.4: Ionization and attachment rates in air as a function of reduced electric field. See the text for a discussion of the various curves.

given therein:

$$\nu_a = \frac{N}{N_0} \sum_{i=0}^2 a_i x^i \quad \text{where} \quad x = E_{\text{eff}} N_0 / N \quad (3.15)$$

and the coefficients are $a_0 = -2.41 \times 10^8$, $a_1 = 211.92$, and $a_2 = -3.545 \times 10^{-5}$ [Pasko, 1996]. This model has been shown to underestimate the attachment rate at higher energies [Pasko et al., 1997]; however, at these high energies ionization overwhelms attachment, so that an accurate calculation of the attachment rate is not necessary.

The field strength at which the ionization rate equals the attachment rate ($\nu_i = \nu_a$) is the breakdown field E_k , shown in Figure 3.4. Above this field value, avalanche ionization occurs, so that the electron density continues to grow as long the electric field is applied. Our use of a higher ionization rate than previous work, such as Taranenko et al. [1993a] and Pasko et al. [1997], results in a lower breakdown field, about $2.8 \times 10^6 N/N_0$ V/m, rather than the often-cited $3.2 \times 10^6 N/N_0$ V/m. However, a number of sources [e.g., Naidis, 2005; Raizer, 1991, p.136] cite values in the range

from 2.6 to 3.2×10^6 N/N_0 V/m. Furthermore, [Davies \[1983\]](#) suggests that the poorly-understood rates for associative detachment processes may significantly affect the ionization and dissociative attachment rates; then again, these detachment effects may not be relevant at the low pressures in the lower ionosphere [[V. Pasko, private communication, 2009](#)]. As such, it should be understood that the ionization and attachment rates used in this work are not well understood, especially at high altitude.

After calculating the effective electric field at a given location in space at a particular time step, the electron density is updated via the simple differential equation:

$$\frac{dN_e}{dt} = \underbrace{(\nu_i - \nu_a)}_{\nu_{\text{tot}}} N_e \quad (3.16)$$

The solution to (3.16) for a small time step Δt , at spatial coordinate (i, j, k) , is given by:

$$N_e(i, j, k, t + \Delta t) = e^{\nu_{\text{tot}} \Delta t} N_e(i, j, k, t) \quad (3.17)$$

3.2.4 Optical Emissions

Optical emissions are calculated for the N_2 first positive (N_2 1P; $B^3\Pi_g \rightarrow A^3\Sigma_u$), N_2 second positive (N_2 2P; $C^3\Pi_u \rightarrow B^3\Pi_g$), N_2^+ first negative (N_2^+ 1N; $B^2\Sigma_u^+ \rightarrow X^2\Sigma_g^+$), O_2^+ first negative (O_2^+ 1N; $b^4\Sigma_g^- \rightarrow a^4\Pi_u$), and N_2^+ Meinel (N_2^+ M; $A^2\Pi \rightarrow X^2\Sigma_g^+$) band systems. The optical excitation rates for these band systems are evaluated for a range of electric fields E_{eff} and neutral densities N using the rates calculated by [Moss et al. \[2006\]](#) using the ELENDIF code. The excitation rates are shown in Figure 3.5 as a function of the reduced electric field.

To determine the photon output, the number of molecules n_k in the excited state k corresponding to the band system of interest must be determined; for instance, for the N_2 1P band system, the number of N_2 molecules in the $B^3\Pi_g$ state is calculated, which is governed by the relation [[Sipler and Biondi, 1972](#)]:

$$\frac{\partial n_k}{\partial t} = \nu_k N_e - \frac{n_k}{\tau_k} + \sum_m n_m A_m \quad (3.18)$$

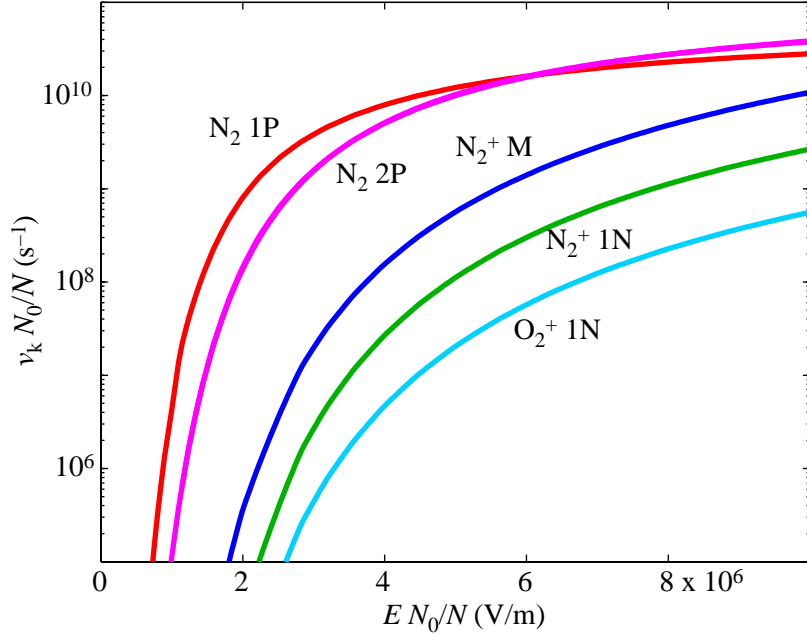


Figure 3.5: Optical excitation rates used in this work; taken from *Moss et al. [2006]*.

where τ_k is the total lifetime of state k and is given by $\tau_k^{-1} = A_k + \alpha_1 N_{N_2} + \alpha_2 N_{O_2}$; α_1 and α_2 are the quenching rates due to collisions with N_2 and O_2 molecules; N_{N_2} and N_{O_2} are the densities of Nitrogen and Oxygen molecules; and ν_k is the excitation rate, given in Figure 3.5. The term $\sum_m n_m A_m$ represents an increase in n_k due to cascading from higher states; for example, cascading from $C^3\Pi_u$ to $B^3\Pi_g$ (through the N_2 2P emission) leaves an extra molecule in the $B^3\Pi_g$ state available for the N_2 1P emission. The coefficients for the band systems under consideration are given in Table 3.1. N_2 1P is primarily quenched by collisions with Nitrogen molecules, while N_2 2P is primarily quenched by collisions with Oxygen molecules.

Since the lifetimes of the states of interest are very short (\sim ns to a few μ s) compared to the rate of change of the electric field (tens to hundreds of μ s), a steady-state solution of Equation (3.18) is assumed at every instant of time, i.e. $dn_k/dt = 0$, so that the solution of (3.18) is

$$n_k = \frac{\nu_k N_e + \sum_m n_m A_m}{A_k + \alpha_1 N_{N_2} + \alpha_2 N_{O_2}} \quad (3.19)$$

Table 3.1: Optical coefficients

Band	α_1 ($\text{m}^3 \text{s}^{-1}$)	α_2 ($\text{m}^3 \text{s}^{-1}$)	A_k (s^{-1})
N_2 1P	10^{-17}	0	1.7×10^5
N_2 2P	0	3×10^{-16}	2×10^7
N_2^+ M	5×10^{-10}	0	7×10^4
N_2^+ 1N	2×10^{-10}	0	1.4×10^7
O_2^+ 1N	4×10^{-10}	0	8.5×10^5

Finally, the intensity in Rayleighs measured by an observer is given by

$$I_k = 10^{-6} \int_L A_k n_k dl \quad (3.20)$$

where the integral is taken along L , the line-of-sight through the source to an observer.

3.2.5 Determination of IC Amplitudes

In this section, estimates are discussed for the amplitudes of the input source current. While currents for cloud-to-ground discharges can be directly measured as discussed in Chapter 1, direct measurements of in-cloud lightning are far more difficult. An accurate measure of realistic in-cloud discharge amplitudes is critical to realistic simulations, since, as is evident from the ionization and attachment rates above, both effects are highly nonlinear. Measurements of in-cloud pulse amplitudes are sparse in the lightning literature. *Smith et al.* [1999] report an average E_{100} (as defined in Chapter 1) of $9.5 \text{ V}\cdot\text{m}^{-1}$ for bipolar pulses, but similar measurements for standard intracloud discharges or spider lightning are not available. In order to simulate spider lightning and intracloud discharges with reasonable accuracy in the 3D EMP model herein, pulse amplitudes are estimated in the following manner, as illustrated in Figure 3.6 for an example event.

VLF broadband data recorded at Yucca Ridge Field Station (YRFS) from 1995–2000 (from Chapter 2) is used with National Lightning Detection Network (NLDN) data to calibrate cloud-to-ground discharges; for instance, knowing that a 90 kA peak current CG discharge corresponds to $E_{100} = 27 \text{ V}\cdot\text{m}^{-1}$ (from Equation (1.6)), the broadband sferic data, with known peak currents, can be converted to E_{100} values.

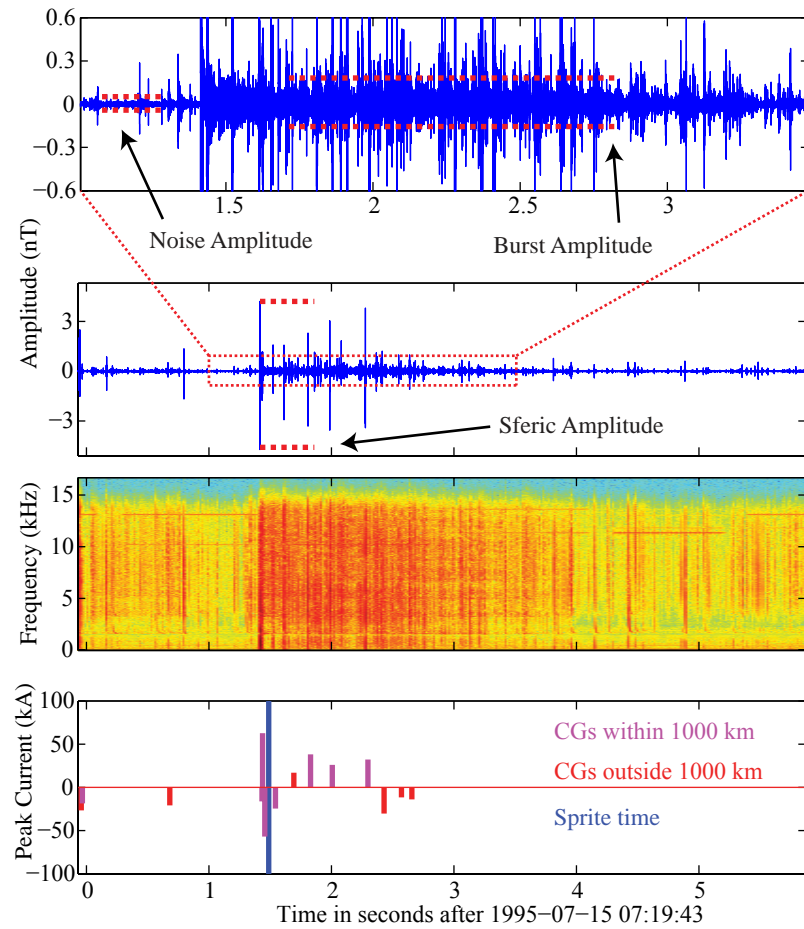


Figure 3.6: Measurement of relative sferic and burst amplitudes. The top two panels show time-series VLF data and the process of measuring the burst envelope amplitude. The third panel shows the sferic burst in spectrogram form, and the bottom panel shows the NLDN lightning data.

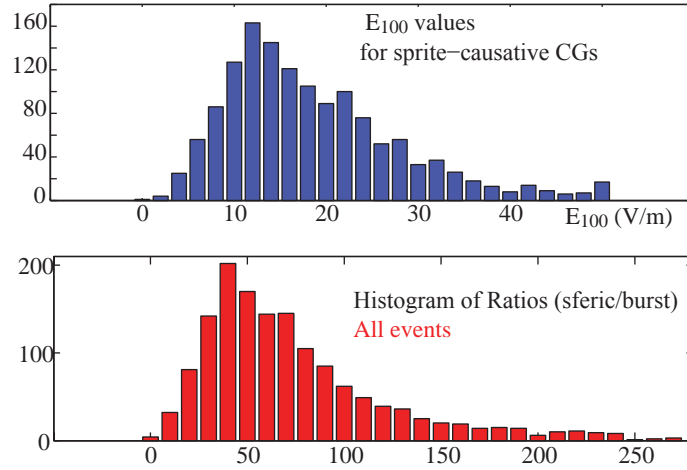


Figure 3.7: Top: Histogram of E_{100} values, directly converted from NLDN peak currents via Equation 1.6. Bottom: Histogram of sferic-to-burst amplitude ratios measured in each of the events studied.

The associated “sferic bursts”, which are thought to be signatures of in-cloud discharges and likely spider lightning when associated with CGs [Marshall *et al.*, 2007], are similarly converted to E_{100} amplitudes by comparing their envelope amplitude (shown in Figure 3.6) to that of the CG-associated sferic. This comparison is made after removing a noise background amplitude determined from a segment nearby (as shown in Figure 3.6, top panel). The distribution of these ratios is shown in Figure 3.7. These results show that the ratio varies from values close to 1 to over 200, but mostly remains in the 20–100 range.

Next, the propagation path to the receiver is modeled to find the expected ratio of sferic amplitude to burst amplitude for pulses of the same source amplitude. For this purpose, an FDTD model of the Earth-ionosphere waveguide propagation is used, using a Debye-like model of the dispersive, anisotropic ionosphere [Chevalier *et al.*, 2008]. An impulsive source is input into the model, and the horizontal magnetic field (H_y) is measured at 600, 800, and 1000 km from the source along the ground. This process is repeated for a vertical current on the ground and for a horizontal current at 5 km altitude. The output is then low-pass filtered at 16 kHz to match the data used above. Figure 3.8 shows the received impulses. One can see that the amplitude of the

CG decreases with distance due to $1/r$ spreading in the first ~ 1000 km (as shown by the dashed line). For the horizontal discharges, however, the amplitude drop is much faster than $1/r$. Horizontal impulses preferentially excite higher-order TE modes (with higher attenuation; [Budden, 1961]) in the Earth-ionosphere waveguide; it is for this reason that sferic bursts are rarely observed at distances > 1000 km [Marshall *et al.*, 2007]. Most events studied were in the 600–800 km range from the receiver; at those distances, the relative amplitude received for the horizontal discharge is ~ 10 –30 times lower than that of the vertical CG sferic, using the impulses in Figure 3.8. Using this value and the factor of ~ 20 –100 reduction in the data amplitude of sferic bursts in Figure 3.7, we find that the relative amplitude at the source is 2–3 times lower for horizontal pulses in sferic bursts than for vertical discharges.

This analysis is applied to each burst measured in Section 2.4; i.e., the distance, CG amplitude, and sferic-to-burst ratio is taken into account for each case, and a resulting burst envelope amplitude is determined. In this way, the distribution of sferic bursts depicted in Figure 3.7 are found to have envelope magnitudes of $E_{100}^{\text{ic}} \sim 5$ –10 $\text{V}\cdot\text{m}^{-1}$. Note that this value is not the electric field amplitude that would be measured at 100 km lateral distance, as it is for the CG; the nomenclature used here is simply for comparison. However, it turns out that the numerical values of E_{100}^{ic} are equivalent to the E_{100} for the CG in terms of the source current, and the E_{100}^{ic} value reported is thus the field that would be measured 100 km in the vertical direction, in the absence of an ionosphere and reflecting ground.

3.3 Results

3.3.1 Single Vertical Discharge

We begin by simulating vertical discharges (cloud-to-ground lightning) in order to a) compare with previous 1D and 2D models, and b) measure the effect of the Earth’s magnetic field on elve observations. Cloud-to-ground lightning is considerably better understood than in-cloud lightning, and amplitudes, stroke durations, and other parameters are generally well-known, as summarized in Table 1.1. Here, we use peak

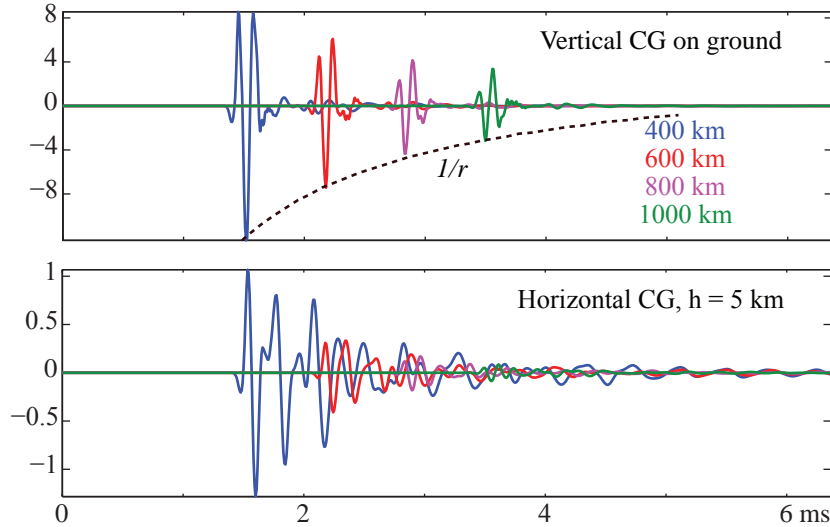


Figure 3.8: Simulated sferics using an FDTD code. Top: vertical CG; bottom: horizontal IC at 5 km altitude. The horizontal discharge decays much more rapidly with distance. These are used to determine the “expected” ratio in Figure 3.7 given the same source amplitude.

currents from Table 1.1 and Equation (1.6) to find input amplitudes.

Figure 3.9 shows the electric field amplitude for an $E_{100} = 20 \text{ V}\cdot\text{m}^{-1}$ vertical and an $E_{100}^{\text{ic}} = 7 \text{ V}\cdot\text{m}^{-1}$ horizontal pulse, at seven snapshots in time, as it propagates into the lower ionosphere. In this example, the Earth’s magnetic field is at 45 degree inclination as shown. The pulses start to impinge on the ionosphere in the third frame ($t = 0.336 \mu\text{s}$), after which the reflection from the ionosphere is evident, with waves propagating back toward the lower boundary. Most of the pulse energy propagates below 90 km altitude in the Earth-ionosphere waveguide as expected; however, a significant amount of energy leaks through the ionosphere. In the upper regions of the ionosphere, where the collision rate is much lower, the fields tend to follow the Earth’s magnetic field, creating an asymmetry in the field pattern. Note that some of the fields with very small magnitude propagating perpendicular to the magnetic field (in blue, at $-70 \text{ dB V}\cdot\text{m}^{-1}$) are artifacts of the numerical code. Further comments will be made comparing the vertical and horizontal cases in Section 3.3.2.

Figure 3.10 shows electron density changes from simulation results using a vertical

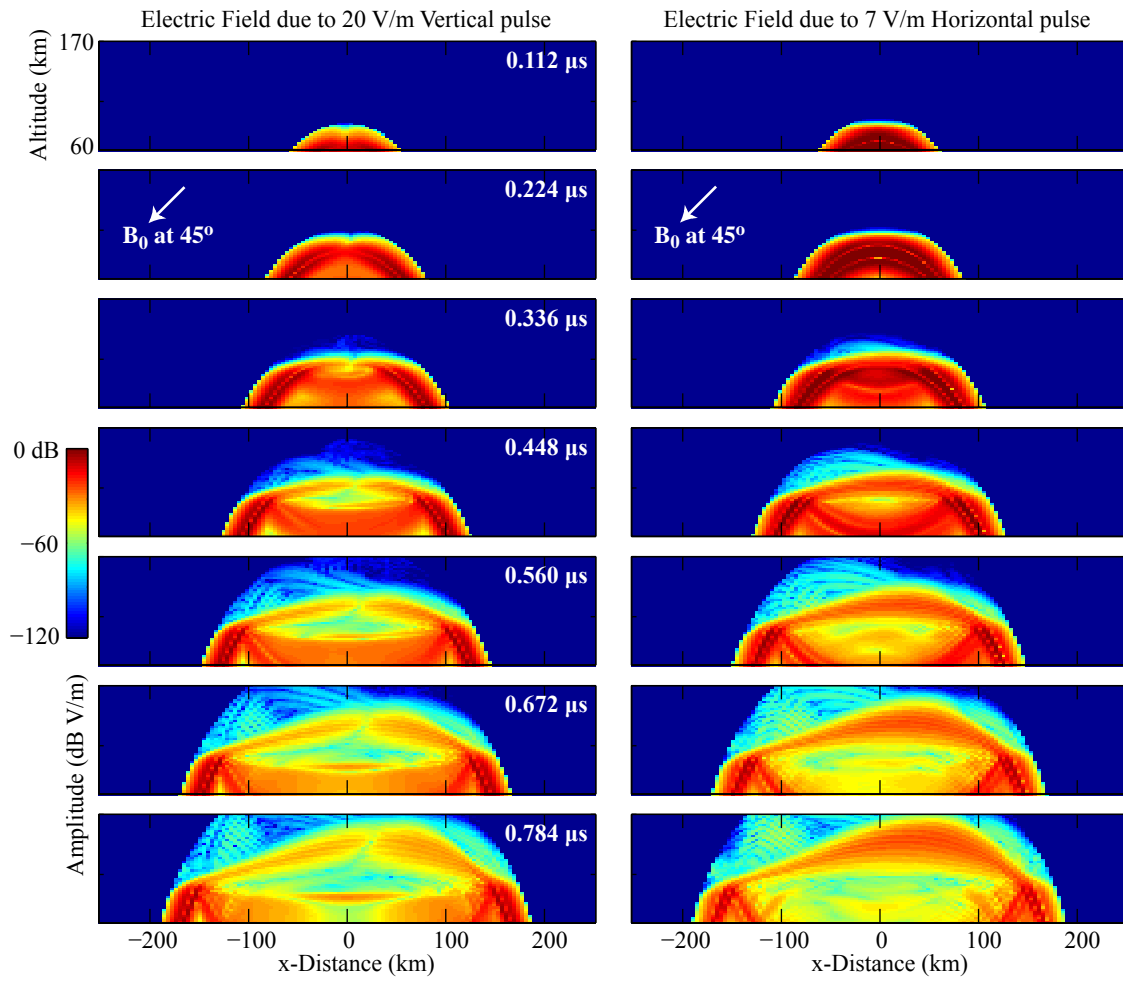


Figure 3.9: Electric field amplitudes of input vertical and horizontal pulses.

dipole with $E_{100} = 15 \text{ V}\cdot\text{m}^{-1}$ (corresponding to a peak current of $\sim 56 \text{ kA}$). At left is a 3D image of four concentric isosurfaces showing the relative effects of ionization (red) and attachment (blue) over the affected volume. At top right is a 2D slice through the x - z plane of the percentage electron density change (calculated as $\Delta N_e/N_{e0} \times 100$). In this plot, zero density change has been held to the color green, so that ionization is red and attachment is blue; this color scheme is kept consistent in all similar plots in this chapter. The bottom right panel shows the 1D slice through the peak in ionization to show the relative and absolute levels of ionization and attachment.

Because of the radiation pattern of a vertical dipole on the ground, the maximum field at 70 km altitude is only $10.4 \text{ V}\cdot\text{m}^{-1}$; in this connection, the results shown here differ from previous work in 1D, such as [Taranenko et al. \[1993a,b\]](#), which simply injected a field amplitude at the lower 70 km boundary. For this pulse we use $\alpha = 10^5$ (temporal pulsewidth $\tau = 20 \mu\text{s}$), which is among the fastest return strokes for CG discharges, but within measured values [Table 1.1 herein [Berger et al., 1975](#)]. The magnetic field is taken to have a dip angle of 45° , corresponding to a geomagnetic latitude of $\sim 27^\circ$. Note that most elves observed by the ISUAL experiment onboard the FORMOSAT-2 satellite are seen in the tropics, near the equator [[Mende et al., 2005b](#)] (generally following the global distribution of lightning), so that 45° is a good upper limit on the magnetic dip angle.

Figure 3.11 shows simulation results for vertical dipoles of $E_{100} = 15, 20, 25,$ and $30 \text{ V}\cdot\text{m}^{-1}$, as well as optical emissions for the $20 \text{ V}\cdot\text{m}^{-1}$ case. We see that while dissociative attachment (blue) is prevalent for the $15 \text{ V}\cdot\text{m}^{-1}$ case, ionization (red) takes over at $20 \text{ V}\cdot\text{m}^{-1}$ and quickly dominates. This result is most evident in the 1D slices shown at bottom right. The dominance of ionization is attributed to the small window of electron energies where attachment dominates in Figure 3.4, with relatively low rates, while above E_k ionization takes over with considerably higher rates. The Earth's magnetic field results in an observable asymmetry in the electron density perturbation at $20 \text{ V}\cdot\text{m}^{-1}$ (top left), but the asymmetry is small in the optical emissions (top right).

In the directions perpendicular to \mathbf{B}_0 the density changes and optical emissions are strongest, since in those directions the EMP electric field is along the magnetic

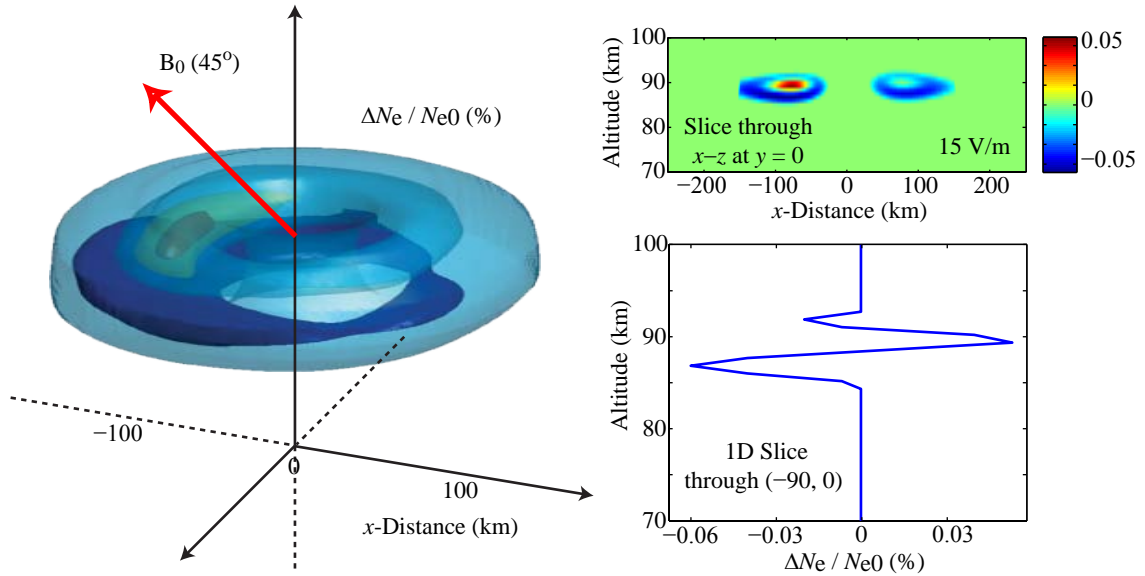


Figure 3.10: Example simulation of an elve from a vertical discharge. Left: 3D isosurfaces; red corresponds to the strongest ionization, and the dark blue is the strongest attachment. Right: 2D and 1D slices through the 3D density change region. All quantities plotted are $\Delta N_e / N_{e0}$ in percent of local ambient density.

field (i.e., $\vec{E}_w \parallel \mathbf{B}_0$). As a function of the amplitude of the input pulse, the asymmetry is strongest for lower amplitude pulses, since the “effective field” is reduced according to Equation (3.10), wherein the collision frequency ν_e increases with the effective field E_{eff} . This equation implies that the lower the field intensity, the greater is the asymmetry due to the magnetic field. Physically, this result makes sense since when the EMP electric field is more intense, the less important is the role of the magnetic field in facilitating (parallel direction) or inhibiting (perpendicular direction) collisions. Events that are only just above the respective thresholds of attachment, optical emissions, or ionization thus exhibit the greatest asymmetry. This is reflected in Figure 3.11, where the asymmetry is much less obvious when the amplitude reaches $30 \text{ V}\cdot\text{m}^{-1}$; and for the $20 \text{ V}\cdot\text{m}^{-1}$ case, the asymmetry is much more prominent in attachment than it is in the optical emissions.

A comment on the choice of pulse duration ($\sim 20 \mu\text{s}$) is necessary. Due to the use of the second-order Mur boundary condition at the input boundary, longer pulse durations are difficult to simulate in the current version of the model. Longer pulse

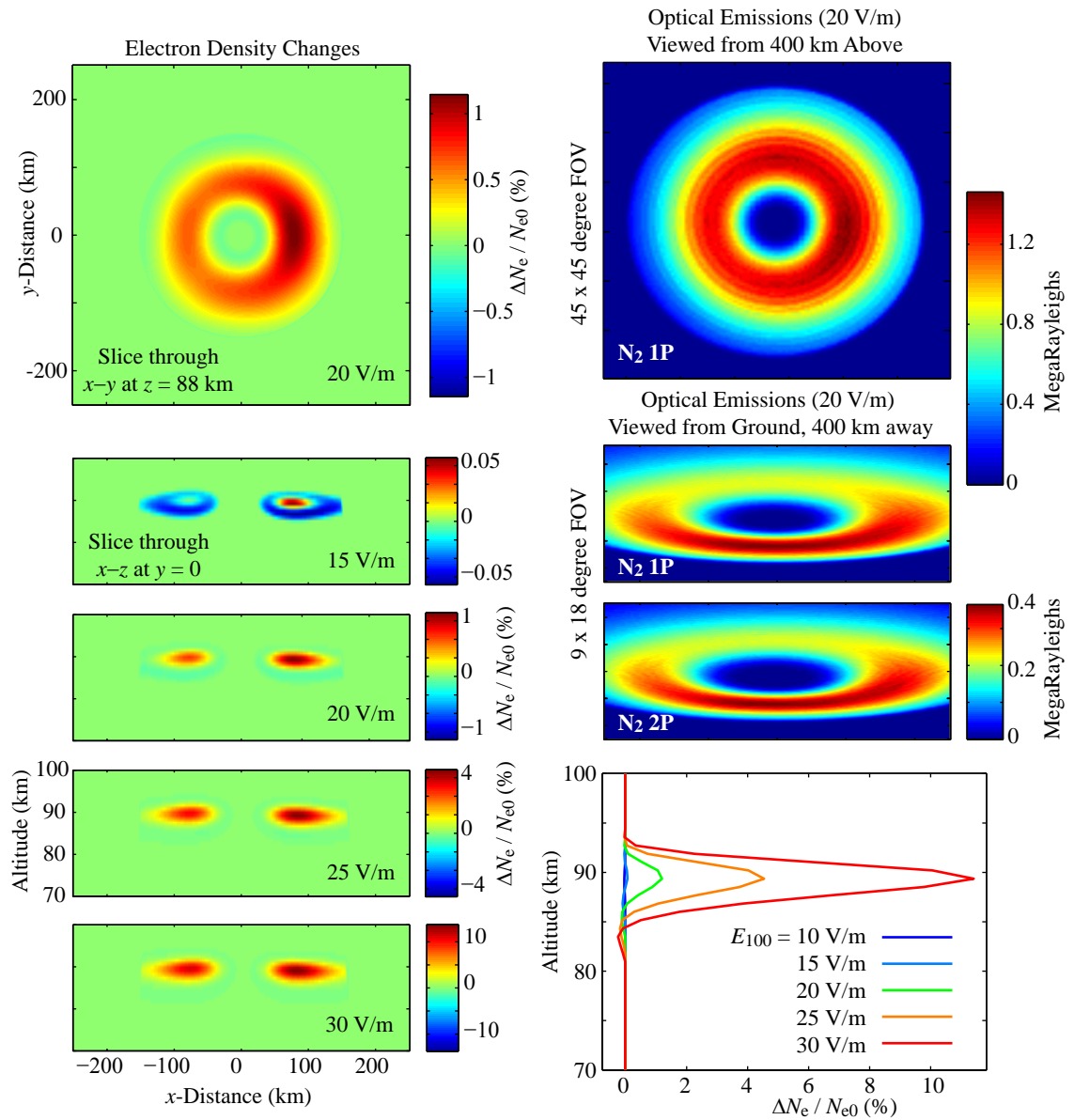


Figure 3.11: Simulations of an elve from a vertical discharge. Density changes in 2D slices are shown at left; optical emissions for the 20 V-m⁻¹ case in the first three panels on the right; and 1D slices of density changes at bottom right. The bottom-left four panels show the effects of varying input amplitude.

durations do not affect the Electric field amplitude in the ionosphere, since E_{100} and τ are forced to be independent. Thus, a larger τ merely extends the duration of the electric field in the ionosphere. This longer duration increases ionization, attachment, and optical emissions on an absolute scale, but their *relative* contributions do not change since the field amplitude is the same. Hence, the qualitative results should not be significantly affected by this choice of pulse duration α .

3.3.2 Horizontal Discharge

The 3D nature of this model allows us to realistically simulate horizontal discharges for the first time. The right column of Figure 3.9 shows the electric field amplitudes at various snapshots in time for a $E_{100}^{\text{ic}} = 7 \text{ V}\cdot\text{m}^{-1}$ horizontal pulse at 5 km altitude. This pulse has the same duration ($20 \mu\text{s}$) as the vertical $E_{100} = 20 \text{ V}\cdot\text{m}^{-1}$ pulse in the left column. First, note that for the horizontal case, there is no null in the vertical direction, as expected. Second, there is much less intensity at late times at altitudes in the 70–90 km range; in the vertical case, these persistent fields are the quasi-electrostatic field due to the charge removal (the $1/r^3$ terms in Equations (3.1) and (3.2) related to M , the integral of the dipole moment).

Figure 3.12 shows density changes and optical emissions for a single $7 \text{ V}\cdot\text{m}^{-1}$ pulse at 5 km altitude, with a pulse duration of $\tau = 20 \mu\text{s}$. Note that the electron density changes for this $7 \text{ V}\cdot\text{m}^{-1}$ discharge compare to the effects of a $20 \text{ V}\cdot\text{m}^{-1}$ CG in both magnitude and the relative contributions of ionization and attachment. However, the shape of the disturbed region is significantly different, and the total volume disturbed is somewhat smaller (note the different x and y scales). The absence of the ring shape is simply due to the radiation pattern of the CG versus IC discharges; where the CG discharge had a null in the vertical direction, the IC discharge has a maximum.

Figure 3.13 shows results for horizontal discharges as a function of the input amplitude. Again, note that much smaller pulses create effects with similar magnitude compared to vertical discharges of the same E_{100} ; for example, ionization begins around $5 \text{ V}\cdot\text{m}^{-1}$, whereas for the vertical discharge, $15 \text{ V}\cdot\text{m}^{-1}$ is required. The lowered threshold is of course due to i) the radiation pattern of the horizontal discharge, having

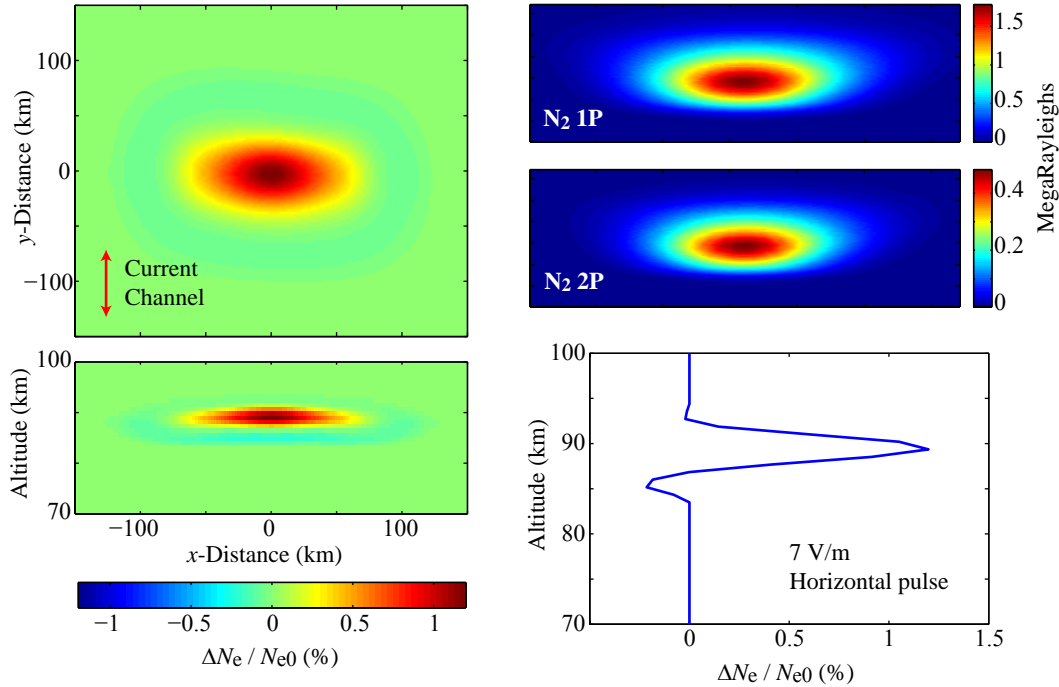


Figure 3.12: Results for $7 \text{ V}\cdot\text{m}^{-1}$ horizontal discharge at 5 km altitude. Left: 2D slices of electron density change; Top right: optical emissions in N_2 1P and 2P band systems; Bottom right: 1D slice of electron density change.

its maximum in the vertical direction; ii) the difference in distance, since the greatest effects of the vertical discharge are seen ~ 100 km radially from the discharge; and iii) the reflection from the conducting ground, which in these simulations is treated as a perfect conductor. The combined effects of these three factors also account for the three-times lower amplitude required in Figure 3.12 to achieve effects similar to the CG case.

Results shown here once again use a pulse with $\alpha = 10^5$, or a $\sim 20 \mu\text{s}$ pulse. This value agrees well with data from *Proctor et al.* [1988] and *Mazur et al.* [1997], which report on intracloud pulses of two types: $1 \mu\text{s}$ “pulses”, and “Q-trains”, bursts of pulsed activity lasting from 10 to over $400 \mu\text{s}$, with a median of $80 \mu\text{s}$ [*Proctor et al.*, 1988]. Statistics are not given on the duration of individual pulses within Q-trains, as they are indistinguishable from one another. By contrast, bipolar pulses have been reported with durations from 10 to $75 \mu\text{s}$ [*Rakov and Uman*, 2003, Table 9.3].

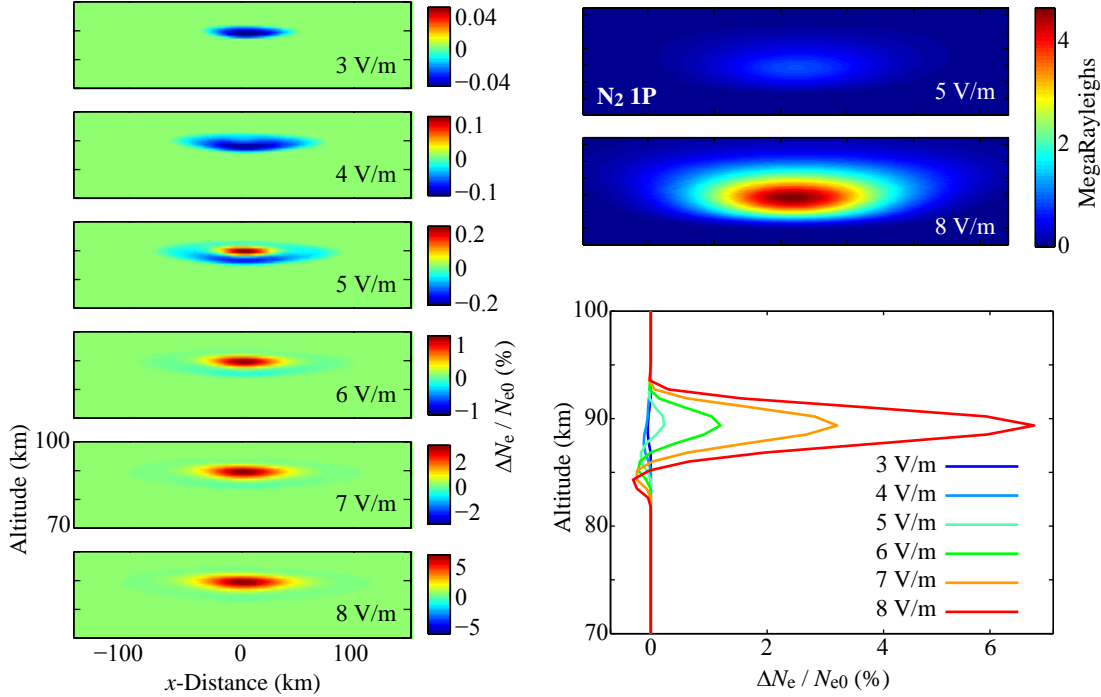


Figure 3.13: Amplitude variation for horizontal discharges at 5 km altitude. Below 3 V-m^{-1} no attachment is observed; ionization begins at about $4\text{--}5 \text{ V-m}^{-1}$. This ionization threshold depends on both the pulse speed and altitude as described in the text.

Statistics for pulses within so-called “spider lightning”, thought to be the source of continuing current and thus large charge moment changes in sprite-producing lightning [Stanley *et al.*, 1999], are not available in the literature; unfortunately, spider lightning is of the greatest interest to the current problem. For the results shown in this work, $\sim 20 \mu\text{s}$ has been chosen as a mean value for two reasons: first, faster pulses cannot be accurately simulated with the present model since it assumes the establishment of a stationary electron distribution function over a time on the order of $\sim 2 \mu\text{s}$ [Taranenko *et al.*, 1993a; Glukhov and Inan, 1996]; and second, slower pulses create near-field effects (the $1/r^3$ terms in Equations (3.1) and (3.2), related to M , the integral of the current moment) on the ionosphere which are not likely to exist in the fast pulses and Q-trains described by Proctor *et al.* [1988].

Optical emissions from the 7 V-m^{-1} pulse are also shown in Figure 3.12. For the

same pulse duration, the optical emissions in the N₂ 1P and N₂ 2P band systems are very similar in magnitude to the CG results in Figure 3.11. However, it is important to note that the optical intensities in Figure 3.11 are likely to be underestimated. As mentioned earlier, the shape and type of density perturbations (ionization versus attachment) and optical emissions are primarily controlled by the field amplitude, radiation pattern, and ionospheric profile, as is shown in detail later; however, the depth of the density perturbation and intensity of the optical emissions are also controlled by the pulse duration and rate of change. Shorter pulse durations (larger α) yield fields of shorter duration in the ionosphere. Since the ionization, attachment, and optical effects are integrated in time, longer pulses of the same E_{100} have stronger effects. The $\sim 20 \mu\text{s}$ pulses are above average for horizontal pulses, but are on the low end for vertical CG discharges; hence, those effects would in fact be enhanced in the case of the more realistic pulse duration. For a pulse of $\sim 100 \mu\text{s}$, for example, one can expect optical emissions to have a similar shape but ~ 5 times higher intensity. This estimate has been confirmed by simulations that are not shown here.

The left-hand panel of Figure 3.14 shows the intensities of optical emissions, integrated over the field-of-view, versus vertical and horizontal pulse amplitudes, for the N₂ 1P and N₂ 2P band systems. This figure shows that the intensities vary in a predictable way with amplitude. The right-hand panel in Figure 3.14 shows the ratio of N₂ 1P to N₂ 2P intensities versus pulse amplitude; these ratios are similarly independent of pulse duration. Using these results, the discharge amplitudes can be inferred from ground or space-based measurements of elves.

3.3.3 Parameter Variations for Horizontal Discharges

In this section, the parameters for horizontal discharges are varied, including altitude, dipole orientation, magnetic field dip angle, and ionospheric density profile, in order to quantify the effects of these inputs on the resulting density changes.

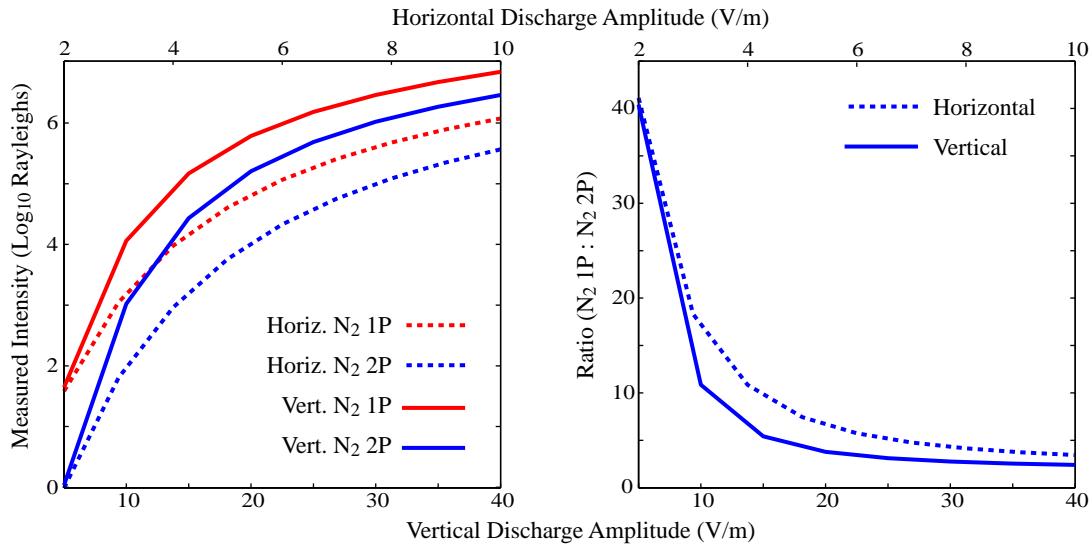


Figure 3.14: Left: Optical intensities for the N₂ 1P and 2P band systems, for horizontal pulses from 2–10 V·m⁻¹ and vertical pulses from 5–40 V·m⁻¹. Right: Ratio of Intensities in 1P and 2P for the same pulses.

Altitudes of IC Discharges

Mazur et al. [1997] provides an overview of source pulse altitudes for IC discharges measured with Time-of-Arrival (TOA) versus Interferometric (ITF) receiver systems. Results therein show that TOA-received pulses, which are preferentially single, fast $\sim 1 \mu\text{s}$ pulses, range in altitude from 5–15 km with a peak in the distribution at ~ 10 km, whereas ITF sources, which are preferentially the longer Q-trains of *Proctor et al.* [1988], range in altitude from 1–10 km, with a peak in the distribution at ~ 5 km. *Marshall et al.* [2007] discussed these results and concluded that the latter category may constitute the currents in spider lightning, which is reported to have altitudes of 4–6 km [*Stanley et al.*, 1999; *Mazur et al.*, 1998]. Similarly, *Noble et al.* [2004] reports on discharges observed by the New Mexico Tech Lightning Mapping Array (LMA) with altitudes from 1–12 km, while *Thomas et al.* [2000] shows 5–7 km altitudes for “hybrid IC-CG discharges”, referring to IC pulses that are associated with a CG. These discharge altitudes are used in this work, and most results herein use an altitude of 5 km, with variations shown below.

Figure 3.15 shows results of analytical calculations, using a $10 \text{ V}\cdot\text{m}^{-1}$ horizontal source input, of the maximum field amplitude over time at 70 km altitude for a range of dipole altitudes from 0.5–10 km. These calculations are for $\alpha = 10^5 \text{ s}^{-1}$. The left-hand panel shows the field amplitude in $\text{V}\cdot\text{m}^{-1}$ versus time at 70 km altitude (with no ionosphere) for pulses from 0.5–10 km altitude. The right-hand panel shows the peak field amplitude versus the amplitude along the ground at 500 km range (again, with no ionosphere). These analytical calculations predict that the field has its highest magnitude for pulses at 3 km, and the amplitude slowly drops off up to 6 km altitude. This result is due to the ground reflection: for a source altitude of 3 km, the ground reflection interferes constructively with the input pulse; below and above 3 km, the interference becomes more and more destructive. At its point of most constructive interference (at 3 km source altitude), the fields measured are essentially double the input field, showing that the ground reflection plays a vital role in ionospheric effects (Note that $\alpha = 10^5 \text{ s}^{-1}$ corresponds to a spatial pulsewidth of about 6 km). It is important to note that this optimal altitude varies depending on the pulse frequency content (i.e., the parameter α). The right-hand panel of Figure 3.15 also demonstrates a source pulse at 3 km altitude also has the highest “efficiency” in terms of directly affecting the ionosphere: it yields a strong field in the ionosphere but a very small amplitude 500 km away on the ground, where a VLF receiver might be located.

Figure 3.16 shows a variety of simulations with dipoles located at different altitudes, to demonstrate the effects described above. Note that in this case, unlike other figures in this section, the density perturbations and optical emissions are shown using the same color scales for ease of comparison. These results agree with Figure 3.15; the largest perturbations are seen for a source dipole at 3 km, with effects diminishing as the altitude is increased or decreased. For a source altitude above 5 km, the maximum density change does not vary greatly, in agreement with Figure 3.15; essentially, for higher source altitudes the primary pulse and its ground reflection become separated in time and do not interfere, so that the effects are those of two successive impulses.

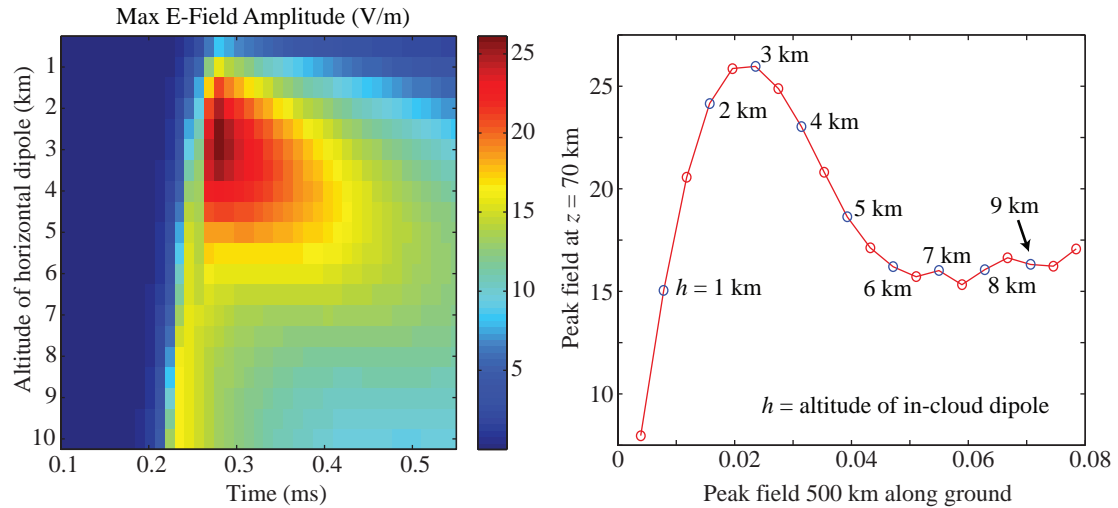


Figure 3.15: Effect of variation in the dipole altitude: Analytical calculations. Left: the maximum electric field amplitude observed at 70 km altitude, as a function of time, for pulses from 0.5 to 10 km altitude. Right: the maximum field amplitude 500 km along the ground (i.e., where a VLF receiver would measure it) versus the amplitude at 70 km above the pulse. A pulse at 3 km altitude, for example, yields the strongest field at 70 km, while its amplitude along the ground is very small.

Ionospheric Profiles

As shown in previous results such as in [Taranenko et al. \[1993a\]](#) and [Barrington-Leigh et al. \[2001\]](#), the ionospheric profile used has a very significant effect on the electron density changes and optical emissions. Figure 3.17 shows the results for a $E_{100} = 20 \text{ V}\cdot\text{m}^{-1}$ vertical discharge (left) and a $E_{100}^{\text{ic}} = 7 \text{ V}\cdot\text{m}^{-1}$ horizontal dipole at 5 km altitude (right), incident on three different electron density profiles. Density profile #2 is used in all other results shown in this paper. Profile #1 is slightly more tenuous than #2, and shows a slight increase in the ionospheric effects, both in density changes and optical emissions. Profile #3, a dense nighttime profile, tends to suppress the effects of the input pulse compared to #2, and shows only effects of attachment. This result is in agreement with [Taranenko et al. \[1993a\]](#); therein, the authors had to increase the input pulse from $E_{100} = 20 \text{ V}\cdot\text{m}^{-1}$ to $35 \text{ V}\cdot\text{m}^{-1}$ in order to see similar effects for a denser ambient profile. Generally, as described in [Taranenko et al. \[1993a\]](#), effects of CG and IC pulses are relatively small in dense nighttime or

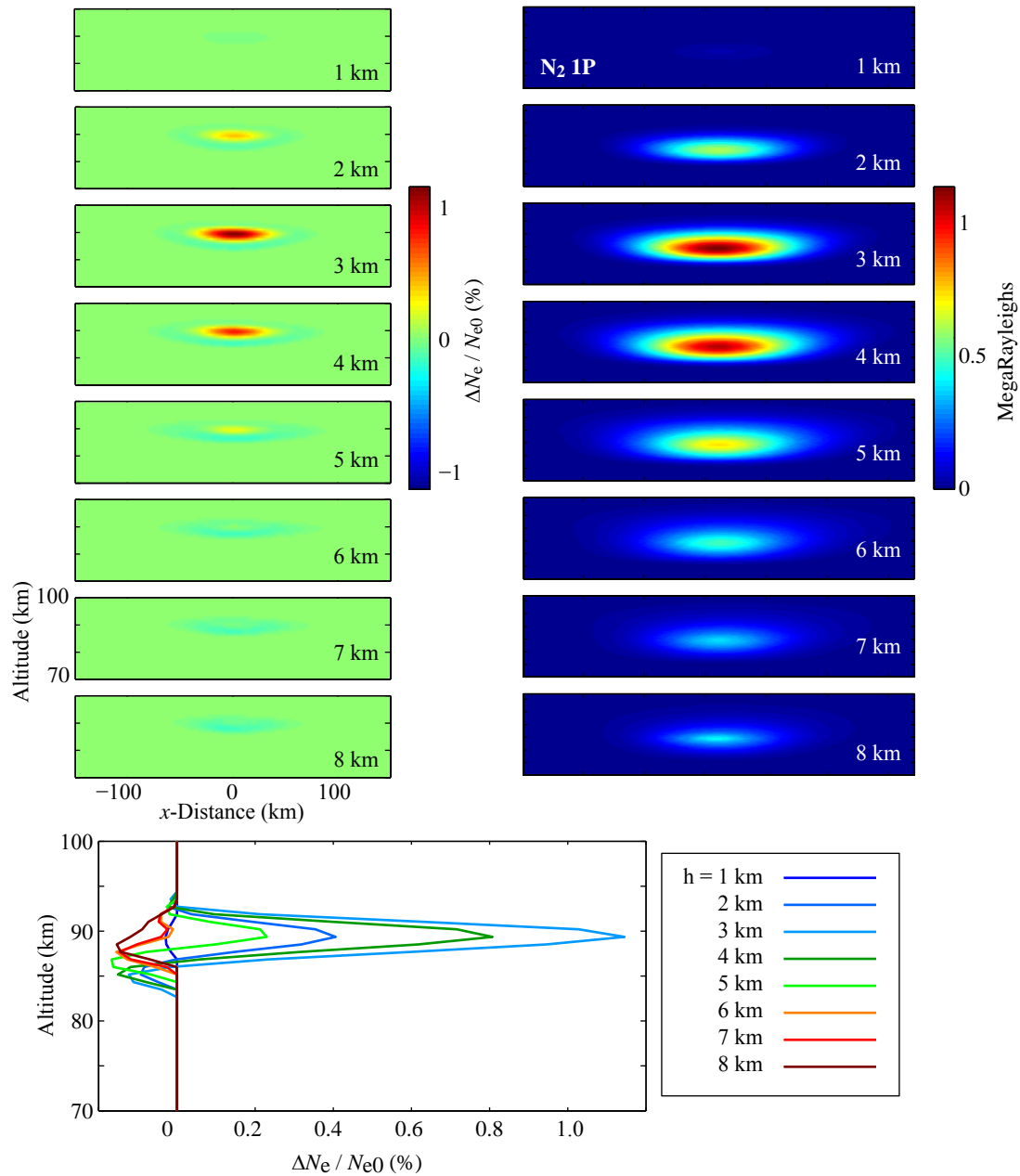


Figure 3.16: Simulation results for horizontal dipoles located at 1–8 km altitude. As predicted by Figure 3.15, the strongest effects are seen for 3 km altitude dipoles; furthermore, above 5 km, the maximum density change does not vary greatly.

daytime ionospheric conditions, and are furthermore relatively less important, and probably not measurable, given the much larger background density. At nighttime, such a circumstance may occur, for instance, after a large Lightning-Induced Electron Precipitation (LEP) event [*Peter and Inan, 2005; Peter et al., 2006*]. The large density increases associated with such events, which may cover a large spatial area, may act to suppress ionospheric effects of lightning discharges below the affected region.

Dipole Orientation

While we have assumed “in-cloud lightning” to be synonymous with “horizontal” lightning, in-cloud lightning discharges may occur with any orientation. In fact, in many cases the discharge occurs between two reservoirs of opposite-polarity charge that are vertically separated, as in *Krehbiel et al. [2008]*. In the case of spider lightning, which extends out many tens of km into the stratiform region of large thunderstorms [*Lyons et al., 1998*], the discharge may be predominantly horizontal. In this section we investigate the effect of the dipole orientation on the EMP-ionosphere interaction.

Figure 3.18 shows results for a $E_{100}^{\text{ic}} = 5 \text{ V}\cdot\text{m}^{-1}$ pulse at 5 km altitude with a duration of 20 μs as usual, while the dipole angle has been varied from 0 degrees (horizontal) to 90 degrees (vertical). In all cases the dipole is oriented so that the projection onto the ground is parallel to that of the Earth’s magnetic field \mathbf{B}_0 ; i.e., both are in the y - z plane. As expected, the resulting electron density change decreases rapidly as the dipole varies away from horizontal. The radiation pattern of a dipole is maximum perpendicular to the current, so angles off horizontal have maxima in the pattern away from vertical. Furthermore, the interference with the ground reflection is significantly affected by the radiation pattern. Above 60 degrees, there is no change in electron density for this 5 $\text{V}\cdot\text{m}^{-1}$ pulse. The optical emissions show a similar effect, with rapidly decreasing intensity with dipole angle towards vertical. The vertical dipole, in fact, has a ring-like shape, due to the null in the radiation pattern, but its intensity is far below observable intensity.

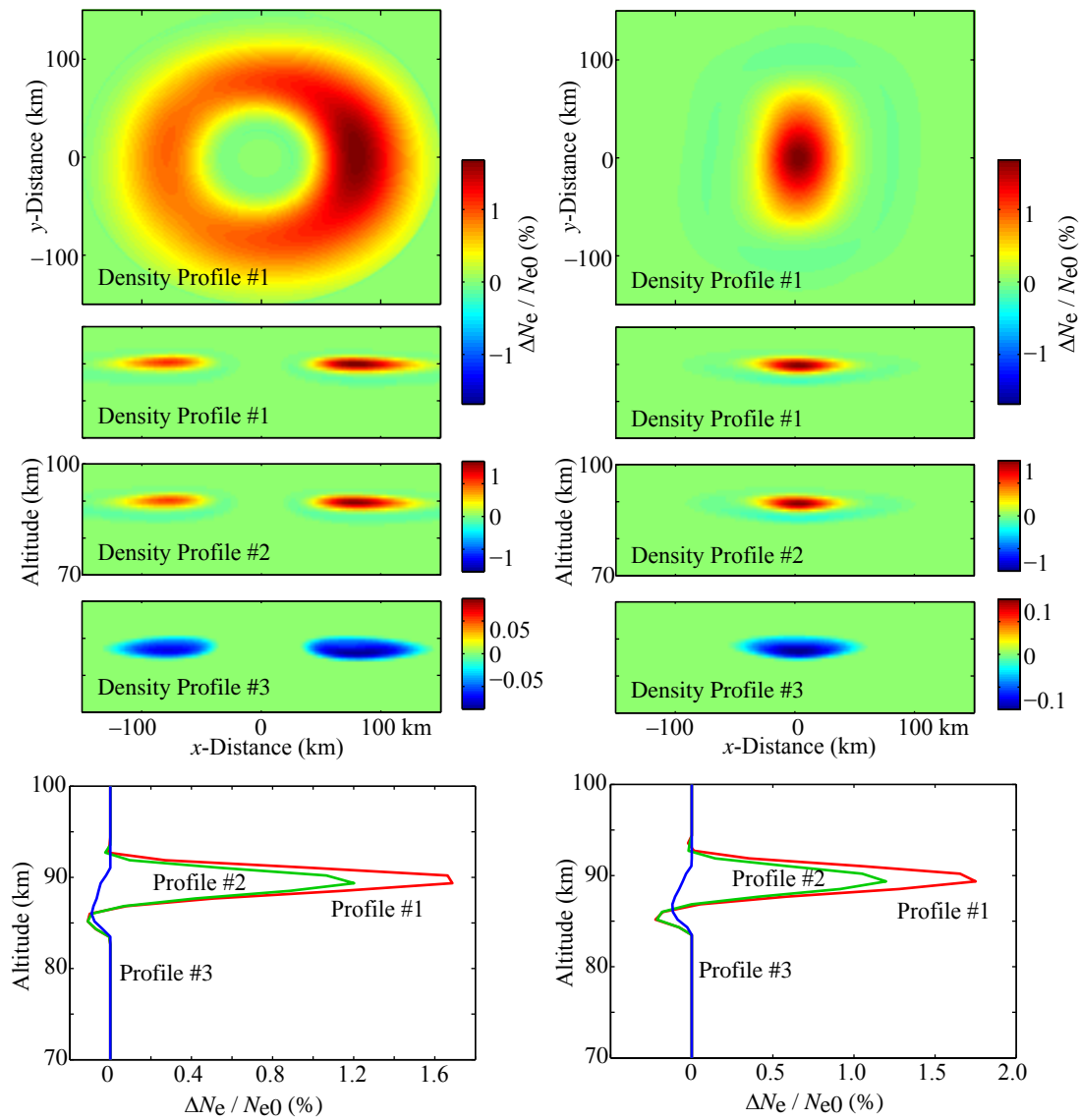


Figure 3.17: Variation with the ionospheric density profile. The dense ionosphere #3 has the weakest response in both electron density change and optical emissions.

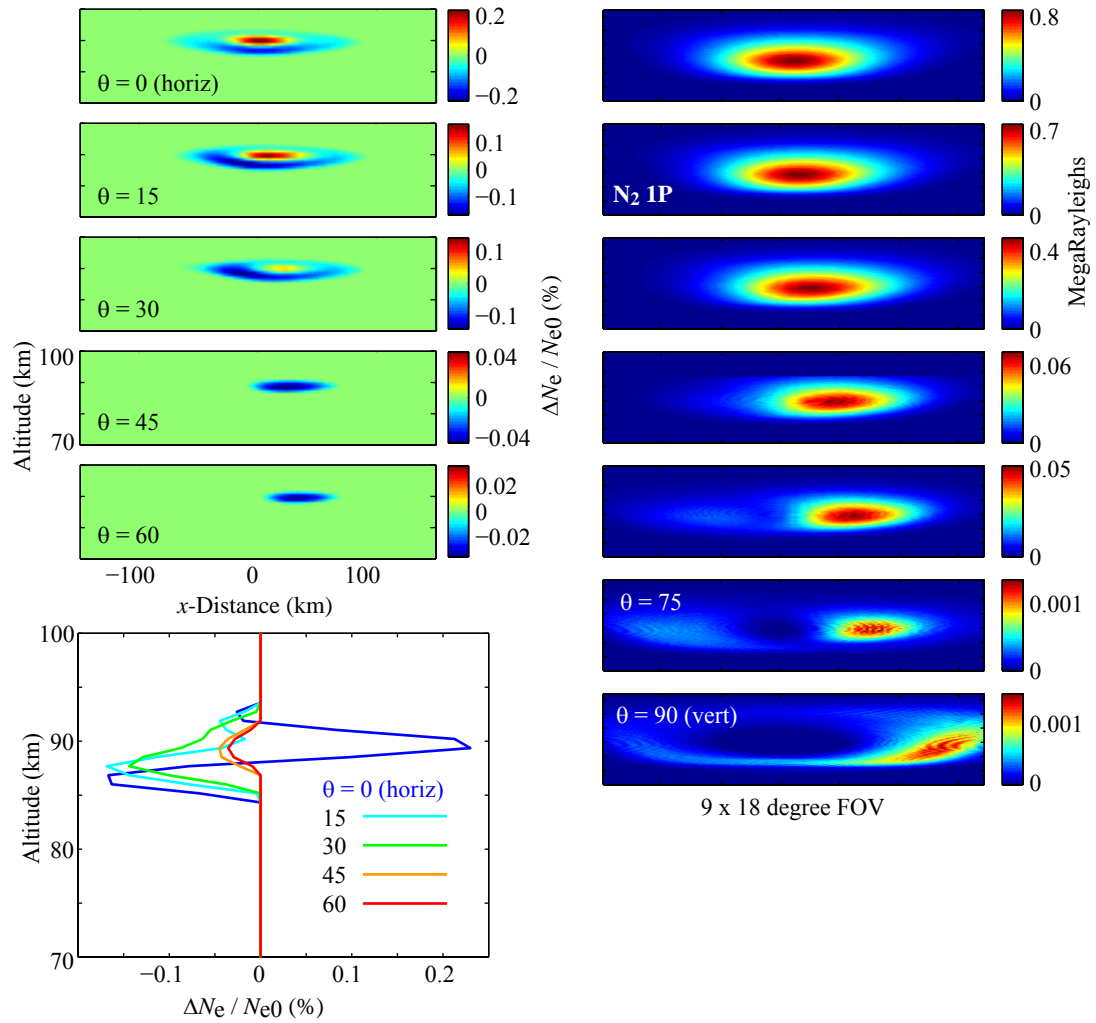


Figure 3.18: Variation in horizontal dipole orientation angle, for pulses of $5 \text{ V}\cdot\text{m}^{-1}$ at 5 km altitude, with B_0 at 45 degrees.

Magnetic Field Orientation

Variation in the orientation of the Earth’s magnetic field is equivalent to variation in latitude. A horizontal magnetic field occurs at the magnetic equator; low angles correspond to the tropics; and higher angles correspond to high latitudes, where a vertical magnetic field would occur at the magnetic poles. The vast majority of lightning occurs over land and at lower latitudes, with very little over 50 degrees geographic latitude [i.e., *Christian et al., 2003*, Fig.4]. Figure 3.19 shows results for which the Earth’s magnetic field orientation has been varied from horizontal (i.e., at the magnetic equator) to vertical (at the magnetic poles). Note that this variation is almost equivalent to a variation in latitude, except that we have not changed the magnetic field amplitude from its value of $B_0 = 50,000$ nT, corresponding to the value at 37° N, 100° E, in Kansas, near where much of the data in Chapter 2 was taken.

The top left panels of Figure 3.19 show the electric field amplitudes at $t = 0.784$ μ s, measured from the time the pulse reaches 70 km altitude, for each of the magnetic field angles. Note that when \mathbf{B}_0 is horizontal, as in the top panel, the magnetic field “shields” the higher altitudes, preventing the fields from penetrating into the magnetosphere. This behavior is explained by the angular dependence of the imaginary part of the refractive index. However, as the magnetic field angle is increased, fields do manage to penetrate through the ionosphere to higher altitudes. For this reason, VLF signatures of lightning, known on the ground as sferics but in space as so-called “0+ whistlers” [*Smith and Angerami, 1968*], are less likely to be seen on satellites near the equator compared to higher latitudes.

Furthermore, we see that a horizontal \mathbf{B}_0 results in higher density changes, by about a factor of two compared to the vertical \mathbf{B}_0 . The horizontal \mathbf{B}_0 results in a stronger reflection from the ionosphere (since fields do not penetrate into the magnetosphere); this reflection thus has a stronger constructive interference with the upgoing pulse, resulting in higher fields and stronger effects. Note that the Earth’s magnetic field is about a factor of two stronger at the magnetic poles than it is at the equator; hence, this effect should be somewhat reduced by the variation of the Earth’s magnetic field intensity.

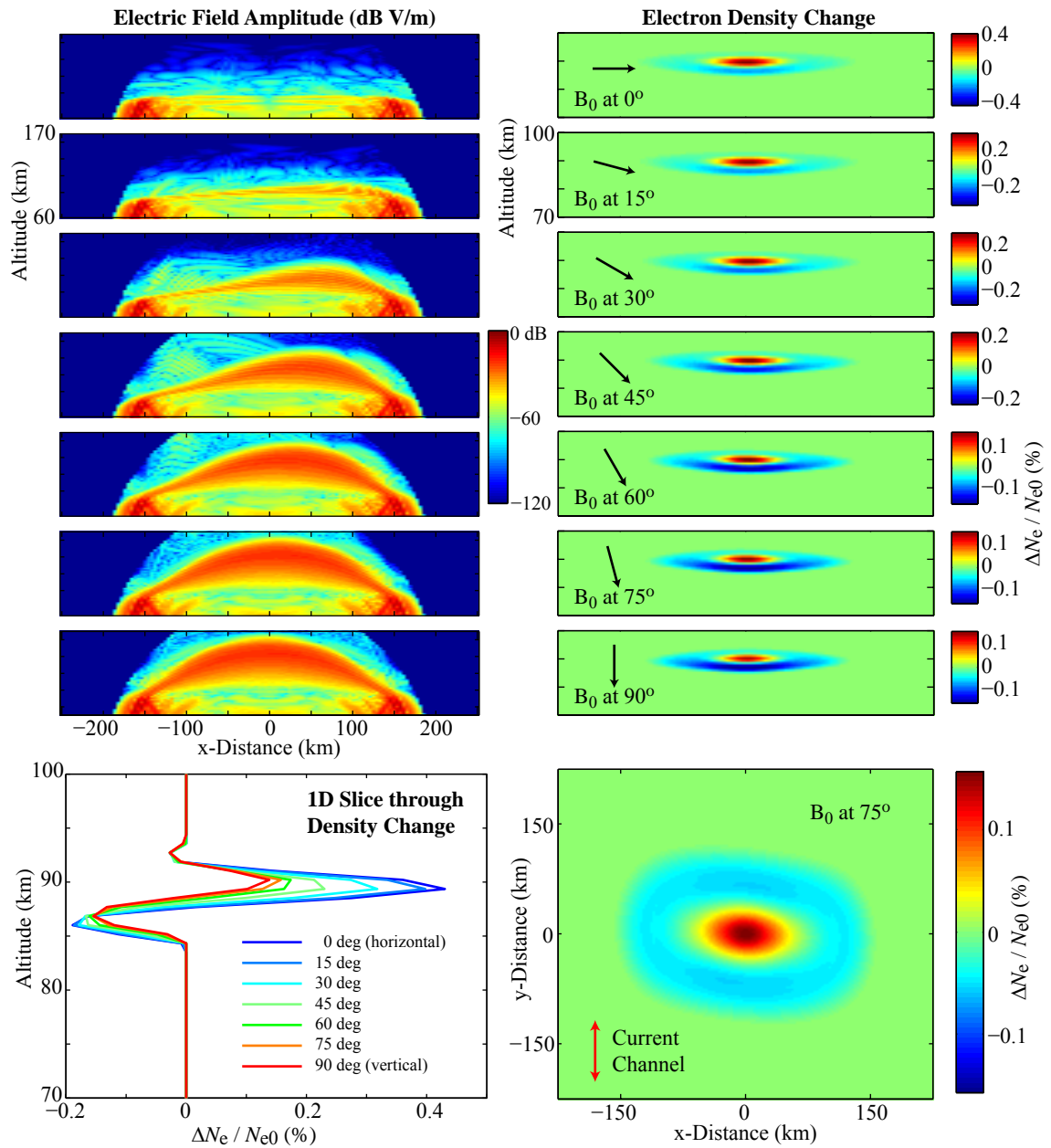


Figure 3.19: Variation in magnetic field dip angle, for horizontal pulses of $7 \text{ V}\cdot\text{m}^{-1}$ at 5 km altitude.

3.3.4 Repeated Pulses

As shown in *Taranenko* [1993], successive pulses may have a cumulative effect on density changes in the ionosphere, yielding density perturbations that may be measurable with subionospheric VLF transmitter signals [*Inan et al.*, 1995; *Johnson et al.*, 1999]. Sprite-producing lightning events, as well as many other lightning events, often have a large component of in-cloud lightning [*Marshall et al.*, 2007], and in the case of sprites this may be so-called spider lightning [*Stanley et al.*, 1999]. It is thus important to model the effect of multiple in-cloud horizontal impulses on the lower ionosphere. In fact, very rarely do in-cloud discharges consist of single events, but rather many hundreds of impulsive discharges [e.g., *Mazur et al.*, 1997; *Noble et al.*, 2004], except maybe in the case of bipolar discharges [*Smith et al.*, 1999].

The effect of multiple pulses is modeled by using the resulting 3D electron density profile from one run of the simulation as the input density profile for a subsequent run. This process can then be streamlined and run iteratively for any reasonable number of pulses. Note that the relaxation time of newly-introduced ionization at 80–100 km altitudes is about $\sim 10\text{--}100$ s [*Pasko and Inan*, 1994], while in-cloud lightning bursts last no longer than ~ 3 seconds; as such, the relaxation phase can be ignored. Ignoring the bottom right two panels for the moment, Figure 3.20 shows the effects of up to 60 horizontal discharge pulses of 5, 7 and 10 $\text{V}\cdot\text{m}^{-1}$. The optical output for each pulse is very nearly the same as for a single pulse, with small variations due to the change in electron density; the N_2 optical emissions have short lifetimes ($\sim 10\text{--}100$ ns) compared to the realistic inter-pulse period ($\sim \mu\text{s}$), and so is taken to have extinguished before the next pulse; high-speed photometry should thus see a sequence of independent, repeated pulses with intensities as presented in Figure 3.13. In these first three sets of simulations the amplitudes, altitudes and discharge orientations have been kept constant for simplicity.

Results show that for 60 pulses, a significant density change accumulates in the lower ionosphere, which initially increases the 3D electron density perturbation cumulatively, very nearly linearly with number of pulses. This linear trend must of course break down for the negative perturbation when it reaches many tens of percent, as in Equation (3.16) the rate of change of electron density dN_e/dt depends on N_e itself.

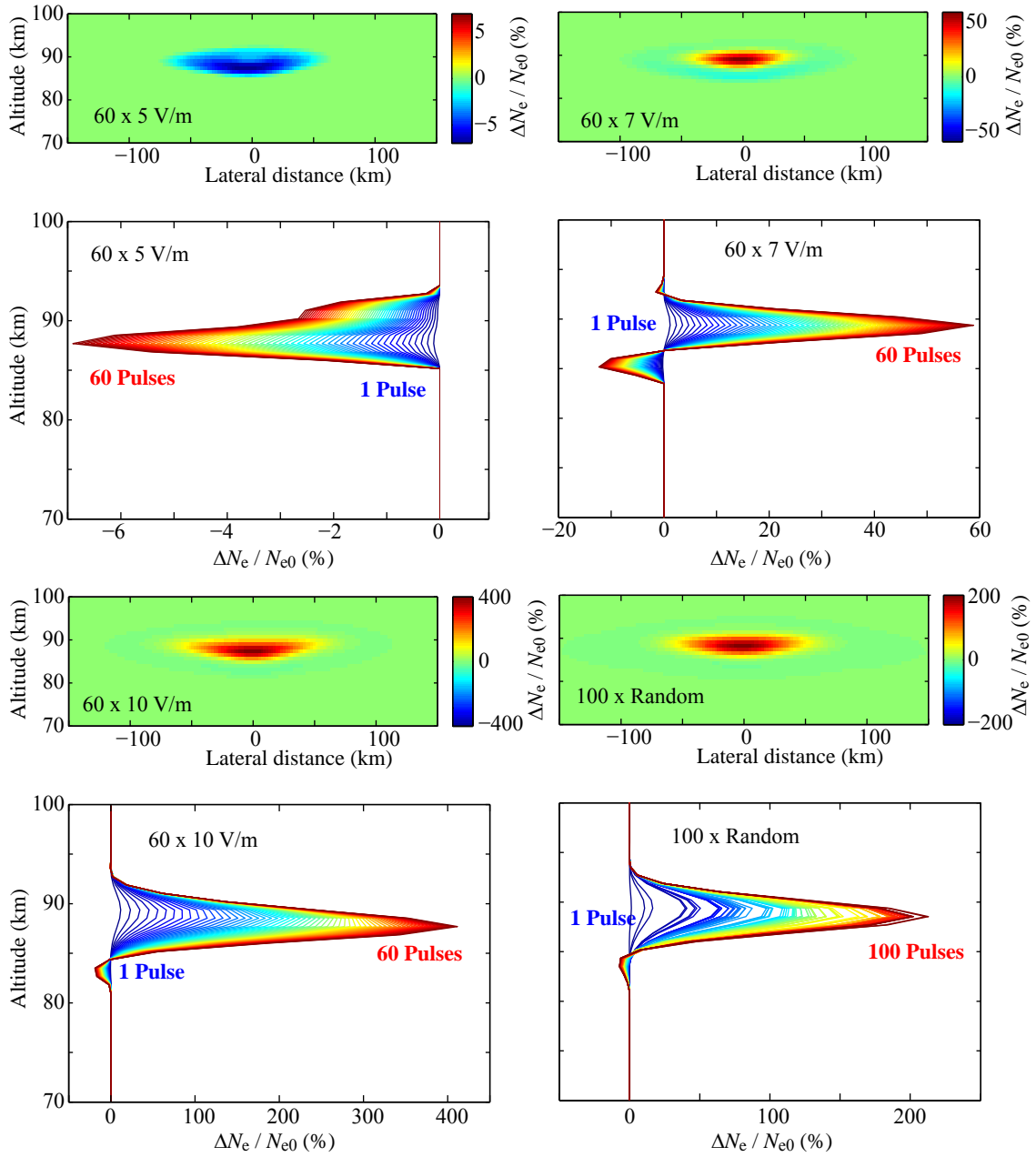


Figure 3.20: Effects of multiple pulses on the ionosphere. The top left two panels are for $E_{100}^{ic} = 5 \text{ V}\cdot\text{m}^{-1}$ inputs; top right for $7 \text{ V}\cdot\text{m}^{-1}$; bottom left for $10 \text{ V}\cdot\text{m}^{-1}$; and bottom right for random inputs. Note that optical emissions are the same as for each pulse separately, since the optical relaxation times are short compared to the inter-pulse timing.

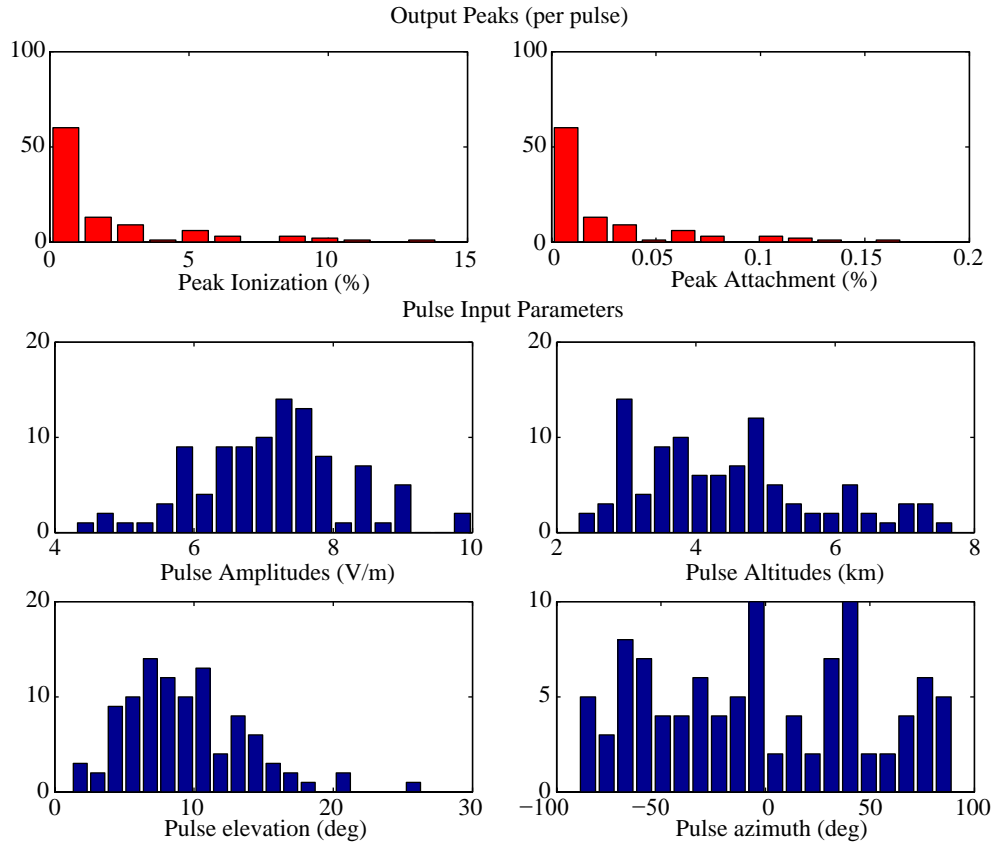


Figure 3.21: Parameters of pulses for random sequence in Figure 3.20.

The possibility that these multi-pulse density perturbations could be measured by VLF transmitter signals was explored in [Marshall et al. \[2008a\]](#) and is discussed in full detail in Chapter 4.

The fourth set of simulations in Figure 3.20 (bottom right) shows results for 100 successive pulses, where each pulse is given a random altitude, amplitude, and orientation in three dimensions. These parameters are taken from the realistic values cited above, and their statistics are shown in the histograms in Figure 3.21. This sequence thus represents the closest approximation to the ionospheric effects of a “real” in-cloud burst. With most of the pulse amplitudes falling in the $E_{100}^{ic} = 6\text{--}8$ $\text{V}\cdot\text{m}^{-1}$ range (very reasonable values), this sequence of 100 pulses yields a density increase of over 200%.

3.4 Summary

The most important results of this chapter can be summarized as follows:

1. For realistic CG lightning amplitudes above about 75 kA ($E_{100} = 20 \text{ V}\cdot\text{m}^{-1}$), the threshold for ionization is easily reached, so that most EMPs result in a dramatic increase in the local electron density. For amplitudes of $15 \text{ V}\cdot\text{m}^{-1}$ and below, attachment causes a reduction in electron density, but the total effect is very small. As mentioned in the introduction, a prior 3D model of the EMP-ionosphere interaction was presented by *Cho and Rycroft* [2001]. In that work, while attachment was mentioned and may have been included in the model calculations, the results do not show the effects of attachment.
2. Horizontal impulses, either intracloud discharges, bipolar pulses, or spider lightning, may create significant density perturbations in the overlying ionosphere as well as detectable optical emissions. For realistic IC pulse parameters, these density perturbations are predominantly negative, as above for CG discharges.
3. The parameters of the in-cloud discharge (altitude, amplitude, duration, and orientation) as well as the ionospheric density and magnetic field B_0 have a significant effect on the EMP-ionosphere interaction. Furthermore, the effects are interdependent; for example, there is a maximum field for a dipole at a particular altitude, but that altitude is strongly dependent on the duration. For this reason there is not a particular altitude, duration, or orientation that is the “best”.
4. A sequence of many IC discharges, as in most IC and spider lightning events, may create a cumulative density perturbation in the overlying ionosphere of many tens to hundreds of percent density change. *Marshall et al.* [2008a] further showed that these multi-pulse density perturbations may be detectable as Early VLF events, and that Early VLF events may in fact be the signature of these largely negative density perturbations. This scenario will be explored in detail in the next chapter.

Point number two above has a further implication: each of these sequences of pulses creates potentially observable optical emissions as shown in Figure 3.12, and so the sequence of pulses should create a sequence of “flashing elves” in the ionosphere. These are likely too dim to be observed by ground cameras, but could potentially be observed by ground photometer instruments or satellites.

Chapter 4

Modeling the VLF Transmitter Signal

In the previous chapter, results of a 3D EMP Model were presented, showing electron density disturbances and optical emissions due to the lightning EMP interaction with the lower ionosphere. This chapter investigates whether or not these predicted electron density changes are observable via VLF remote sensing as “Early VLF” events. This determination is of great importance both for understanding of the scientific processes involved in the lightning-ionosphere interaction, as well as in the interpretation of Early VLF data.

4.1 VLF Wave Propagation in the Earth-Ionosphere Waveguide

As mentioned in Chapter 1, at VLF frequencies of a few tens of kHz, both the Earth’s surface and the lower ionosphere are good conductors. Because of these high conductivities, the cavity formed by the nearly concentric spheres of the Earth’s surface and the lower ionosphere acts as a waveguide for VLF frequencies. VLF transmitters, operated by the U.S. Navy and by other countries, take advantage of

the efficient VLF propagation in the Earth-ionosphere waveguide and use it for long-range communications over the surface of the Earth.

Of course, neither the Earth's surface nor the ionosphere is a perfect or homogeneous conductor. The Earth's conductivity varies over its surface and depth; while the conductivity of seawater is about 4 S/m, that of the some rocky regions is as low as 10^{-7} S/m [Rycroft *et al.*, 2008]. Furthermore, the conductivity and permittivity of the Earth's surface are frequency dependent. The nighttime ionosphere reaches a conductivity of 10^{-7} S/m at 80 km altitude [Rycroft *et al.*, 2008], but its conductivity and permittivity are both frequency-dependent and anisotropic due to the presence of Earth's magnetic field \mathbf{B}_0 . What's more, the curvature of the Earth adds to the level of complexity of the waveguide system.

VLF wave energy originating from a source on the ground initially decays as $1/r^2$ from the source (expanding over an area of $4\pi r^2$). After a short distance energy begins to decay as nearly $1/r$, as the fields are now expanding in a cylindrical shell, and waveguide modes begin to be established. This rate of decay does not last long, however; the curvature of the Earth affects this cylindrical expansion, and for distances of ~ 1000 km and greater, field amplitudes are seen to decay at the very low rate of about 2 dB per 1000 km [Crory, 1961]. This decay is primarily due to absorption in the lossy ionosphere.

Reflection from the lower ionosphere is also affected by its lossy and anisotropic nature. The ionospheric losses are dominated by collisions between electrons and neutrals at a rate ν_e , as discussed in Chapter 1. This causes reflection to occur not at $\omega = \omega_p$ ($X = 1$ from Equation 1.2) as in collisionless plasmas, but rather at $X = Z$ (see Equation 1.4), as shown in Figure 1.4 and described in Section 1.3. However, given that the VLF wavelength (~ 15 km at 20 kHz) is long compared with the thickness of this interaction region, it is reasonable to expect that VLF waves would penetrate significantly into the lower ionosphere.

Budden [1961, p. 194] showed that the electric field \vec{E} at a great distance d and altitude z_r due to an oscillating dipole source of unit amplitude at height z_s can be

written as the sum of modes:

$$\vec{E} = \left[\frac{j\omega^2 \mu_0 e^{j\pi/4}}{h\sqrt{2\pi kd}} \right] \sqrt{\frac{d/R_E}{\sin d/R_E}} \sum_m e^{-jk_0 S_m d} \Gamma_m(z_s) \Gamma_m(z_r) \Lambda_m \quad (4.1)$$

where the Earth and the ionosphere are assumed to be concentric spheres and the ionosphere is homogeneous in the longitudinal directions and undisturbed. In Equation (4.1), R_E is the radius of the Earth, and $S_m = \sin \theta_m$, where θ_m is the complex angle of incidence of the ray in mode n ; hence kS_m is the horizontal component of the mode wavenumber. The fractional square-root term outside the summation takes into account the spherical expansion in the Earth-ionosphere waveguide. Γ_m is a 3×3 tensor of height-gain functions that describe the three electric field components as a function of height for a given mode [Budden, 1961]. The tensor Λ_m describes the excitation coefficients of field components for each mode m based on the source dipole orientation.

The goal of a VLF waveguide mode theory is to determine the allowed incident angles θ_m to solve (4.1). The solutions are given by the Fundamental Equation of Mode Theory [Budden, 1961, p. 115] for a wavenumber k :

$$\mathbf{R}_I(\theta) \mathbf{R}_G(\theta) e^{-2jkh \sin \theta} = \mathbf{I} \quad (4.2)$$

where \mathbf{I} is the 2×2 identity matrix, and $\mathbf{R}_I(\theta)$ and $\mathbf{R}_G(\theta)$ are reflection coefficient matrices for the ionosphere and ground, given by

$$\mathbf{R}_I(\theta) = \begin{bmatrix} \parallel R_{\parallel}(\theta) & \parallel R_{\perp}(\theta) \\ \perp R_{\parallel}(\theta) & \perp R_{\perp}(\theta) \end{bmatrix} \quad (4.3)$$

$$\mathbf{R}_G(\theta) = \begin{bmatrix} \parallel \bar{R}_{\parallel}(\theta) & 0 \\ 0 & \perp \bar{R}_{\perp}(\theta) \end{bmatrix} \quad (4.4)$$

In the matrix entries above, the left-hand subscript gives the polarization of the incident wave, while the right-hand subscript gives the polarization of the reflected wave; hence, the $\parallel R_{\perp}(\theta)$ term gives the coupling from a parallel-polarized wave incident on the ionosphere into a perpendicularly-polarized reflected wave. Here the

ground is taken to be isotropic so the cross terms of $\mathbf{R}_G(\theta)$ are zero. The eigenangles θ_m that are the solutions of Equation (4.2) thus define the allowed waveguide modes for a given frequency corresponding to a given wavenumber k .

4.2 Previous Work

An extensive numerical code known as MODEFNDR [*Pappert and Snyder, 1972; Ferguson and Snyder, 1987*] was developed by the Naval Ocean Systems Center (NOSC) to solve for the coefficients S_m in Equation (4.1). MODEFNDR is one of the components of a package known as the Long Wave Propagation Capability (LWPC), which has been used in most prior work of VLF propagation in the Earth-ionosphere waveguide [e.g., *Cummer and Inan, 2000; Moore et al., 2003*].

Tolstoy [1983] and *Tolstoy et al. [1986]* used an early version of MODEFNDR to calculate scattering from regions of enhanced electron density due to Lightning-induced Electron Precipitation (LEP) events. This version of the model was 1D; it did not allow for variations off the Great Circle Path (GCP) from the transmitter to the receiver. This model did, however, include multiple modes and mode coupling.

Dowden and Adams [1988, 1989] were the first to simulate VLF waveguide propagation through a disturbed ionosphere when the disturbance was located off the GCP. However, those models used single-mode propagation and calculated the scattering for only the 2nd propagating mode.

Poulsen et al. [1990] solved a form of Equation (4.1) given in *Wait [1962]* using MODEFNDR for a general D-region disturbance on and off the transmitter GCP. In this model the input energy is partitioned into modes according to the theory of *Wait [1962]*. Coupling between modes is neglected under the disturbed region; however, the method does allow simulation of a full 3D disturbance. *Poulsen et al. [1993a,b]* used the same model to simulate the effects of LEP events on the VLF transmitter signal, again using a 3D geometry.

The complete LWPC package consists of three parts: PRESEG, which uses ground conductivity and permittivity values, together with ionospheric conditions input by

the user, to break the simulation space up into segments. MODEFNDR then calculates the propagating modes in each segment. The third component, FASTMC, calculates the coupling from one mode to another at waveguide discontinuities (i.e., where changes in the ground and ionosphere occur). The inclusion of this third component has allowed more recent simulations to account for the effects of mode coupling. This full version of LWPC has since been used by various authors in its 2D form [e.g., *Inan et al.*, 1996b,d; *Johnson et al.*, 1999; *Cummer and Inan*, 2000; *Moore et al.*, 2003] to model VLF measurements of ionospheric disturbances.

4.3 The FDFD Propagation Model

This work departs from all the prior work cited above and presents a new method for modeling perturbations to VLF transmitter signals. All of the prior models used mode theory to solve for the field amplitude at a given receiver location. In this work, a finite-difference model is used to solve for all six components of the wave field everywhere in 2D space. Any discussion of modes and rays is not necessary in this context, since the fields are solved self-consistently, including effects of the frequency-dependent, anisotropic, and inhomogeneous ionosphere and ground.

The 2D Finite-Difference Frequency Domain (FDFD) model used here to simulate the VLF transmitter signal propagation was first presented in *Chevalier and Inan* [2006] and *Chevalier et al.* [2008]. This model solves the coupled Maxwell's Equations in frequency domain form, discretized in space via second-, fourth-, or even sixth-order centered-differencing, depending on the required degree of accuracy. The equations to be solved are Maxwell's Equations in frequency domain:

$$\nabla \times \mathbf{H} = \sigma_d \mathbf{E} + \sum_n \sigma_n \mathbf{E} + j\omega\epsilon_0 \mathbf{E} \quad (4.5)$$

$$\nabla \times \mathbf{E} = -j\omega\mu_0 \mathbf{H} \quad (4.6)$$

where

$$\sigma_d = \frac{j\omega\epsilon_0(\epsilon_s - \epsilon_\infty)}{1 + j\omega\tau_d} \quad (4.7)$$

$$\sigma_n = \epsilon_0\omega_{p,n}^2 (j\omega\mathbf{I} - \Omega_n)^{-1} \quad (4.8)$$

$$\Omega = \begin{bmatrix} -\nu & -\omega_{cz} & \omega_{cy} \\ \omega_{cz} & -\nu & -\omega_{cx} \\ -\omega_{cy} & \omega_{cx} & -\nu \end{bmatrix} \quad (4.9)$$

Equation (4.7) describes the conductivity of the ground in a single-pole Debye model, demonstrating the frequency dependence. This conductivity changes along the propagation path, which may pass over regions of sea water, fresh water, desert, ice, and so on, where each medium has different values for the parameters ϵ_s , ϵ_∞ , and τ_d . Equation (4.8) describes the anisotropic (i.e., tensor) conductivity of the ionosphere. In Equation (4.8), \mathbf{I} represents the 3×3 identity matrix, and $\omega_{p,n} = \sqrt{q_n^2 N_n / m_n \epsilon_0}$ is the plasma frequency for species n , with density N_n , mass m_n and charge q_n . Electron density profile #2 from Figure 3.2 is used in all simulations presented in this chapter. The anisotropy due to the Earth's magnetic field arises through Ω_n , in which ν_n is the collision frequency between ion species n and neutrals, and $\vec{\omega}_{c,n} = q_n \mathbf{B}_0 / m_n$ is the gyrofrequency for species n . In this model the ionosphere may contain n ion species (plus electrons), and each has its own density, collision frequency, charge, and mass. Note that Ohm's Law $\mathbf{J} = \overleftrightarrow{\sigma} \mathbf{E}$ is inherently included in this formulation, appearing as the first two terms in (4.5).

The model uses the freely-available Portable Expression Template for Scientific Computing (PETSc) package [Balay *et al.*, 2001, 2004], which takes advantage of embedded parallel processing and integrated linear and nonlinear solvers [Chevalier *et al.*, 2008]. The code uses an iterative, parallelized Krylov subspace method to invert the large complex matrix that results from the discretization of Equations (4.5) to (4.9); in particular, the generalized minimum residual (GMRES) Krylov method is used along with an additive Schwarz (ASM) preconditioning matrix [Chevalier *et al.*, 2008, and references therein].

As mentioned briefly in Section (3.2), finite-difference solutions in anisotropic

media require advance Absorbing Boundary Conditions (ABCs) to avoid problems with anti-parallel phase and group velocity vectors at some boundaries. *Chevalier et al.* [2008] describes a new technique referred to as the k-PML, used in this model, to compensate for this phenomenon. The boundary condition used is a form of Perfectly Matched Layer (PML) [Berenger, 1994], in which the nabla operator in Maxwell's Equations (4.5 and 4.6) is replaced with a complex operator defined by

$$\tilde{\nabla} = \hat{x} \frac{1}{s_x} \frac{\partial}{\partial x} + \hat{y} \frac{1}{s_y} \frac{\partial}{\partial y} + \hat{z} \frac{1}{s_z} \frac{\partial}{\partial z} \quad (4.10)$$

In Equation (4.10), s_x , s_y and s_z are complex stretching parameters, defined by

$$s = \left(1 + \frac{\alpha_{\text{pml}}}{j\omega} \right) \quad (4.11)$$

where ω is the wave frequency and α_{pml} is an absorption coefficient. In a traditional PML, α_{pml} is graded from zero to some optimal value at the boundary in order to absorb incident waves with minimal reflection [Taflove and Hagness, 2005, p. 292]. The use of this “stretched coordinate” s_x (or s_y , s_z) term yields a planewave phase term of the form

$$e^{-jk_x x} \rightarrow e^{-jk_x x} e^{(-\alpha_{\text{pml}} k_x / \omega) x} \quad (4.12)$$

In an isotropic medium, a positive α_{pml} causes the wave to decay as it propagates into the PML medium. However, in an anisotropic medium, the wavenumber k_x can become negative, yielding exponential growth in the rightmost factor in Equation (4.12). *Chevalier et al.* [2008] circumvented this problem by modifying the stretching parameter in Equation (4.11) at boundaries where the group and phase velocity vectors are known to have anti-parallel components.

Figure 4.1 illustrates the simulation space, which extends from the ground to 110 km altitude, and up to many thousands of km in the direction of propagation. As mentioned above, frequency-domain methods solve for the fields at a single frequency f in steady-state, and the solution of the system of equations requires large matrix inversions; the size of the matrix is directly related to the size of the simulation space

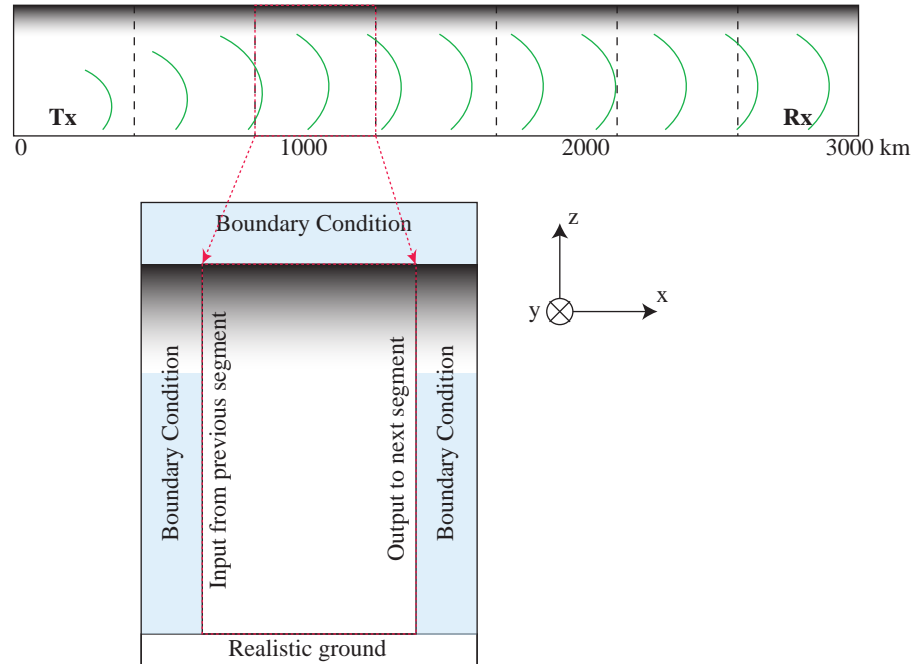


Figure 4.1: VLF Propagation Model, illustrating the Segmented Long Path (SLP) method; adapted from *Chevalier and Inan [2006]*.

in number of grid cells. For the long path lengths simulated here, these matrix inversions are impractical on even modern computers. For this reason, the propagation model uses what is known as the Segmented Long Path (SLP) method, described in *Chevalier and Inan [2006]*, to break the simulation space into manageable segments, as shown in Figure 4.1.

In the first segment (far left), the fields are directly solved for a path of ~ 150 km in length. Once the solution converges to steady-state, the fields at the right edge of the space are used as the “input” to the next segment, as shown at bottom left. This next segment is then allowed to reach steady-state, and its rightmost “output” fields are used as the “input” to the next segment, and so forth until the desired propagation distance is reached.

Figure 4.2 shows the six component output fields of the model after reaching steady state for a typical run. A number of features of the VLF signal propagation

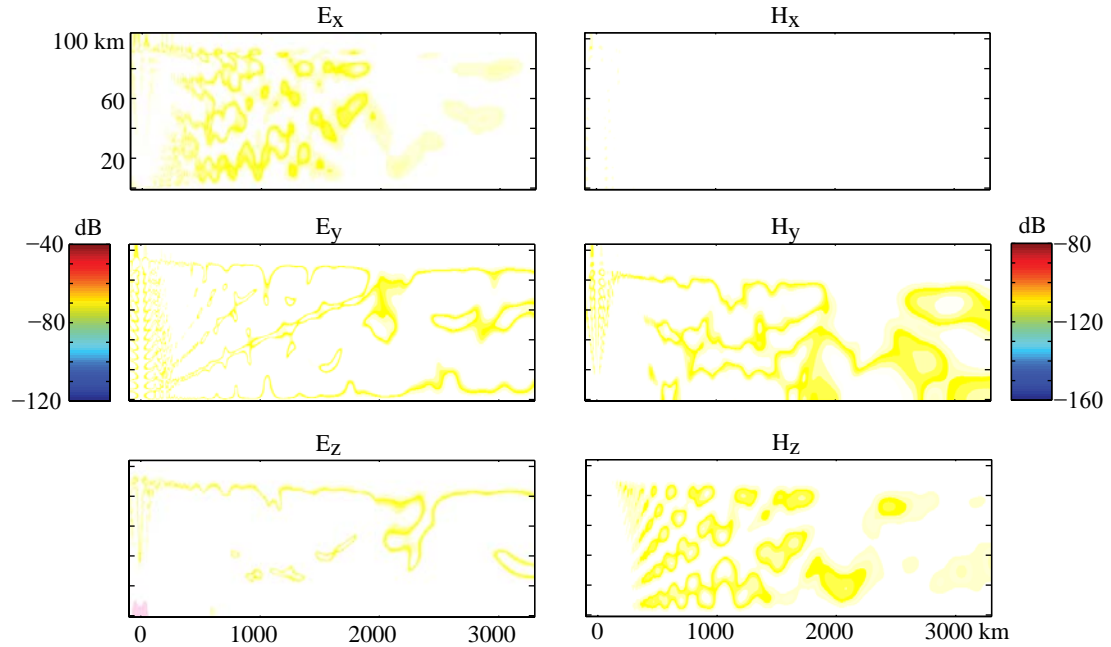


Figure 4.2: Examples of the six component field outputs from the FDFD propagation model; the coordinate system is the same as Figure 4.1. See the text for detailed discussion of prominent features.

are evident in these plots:

1. *Ionospheric reflection.* A sharp drop in field intensity (40 dB or more) is evident around 85 km altitude. This drop is evidence of the particularly “sharp” reflection height for VLF waves, and is the primary reason for efficient propagation in the Earth-ionosphere waveguide.
2. *Slow decay with distance.* Measurements of the E_z and H_y components (the QTEM mode) along the ground show a ~ 2 dB per 1000 km amplitude decay, in agreement with measurements [[Crary, 1961](#)].
3. *Interference patterns.* Near the transmitter (lower left corner at $x = 0$ km), a complex interference pattern is evident in each of the field components, with a large number of nulls throughout the 2D space. This pattern is due to the interference of a large number of waveguide modes excited by the transmitter.

Farther from the transmitter ($\sim 2000\text{--}3000$ km away), only a few waveguide modes are present since the higher order modes decay rapidly with distance. As such, the interference pattern “settles down” after a few thousand km.

4. *Predominance of TM modes.* The vertical source dipole nature of the transmitter preferentially excites TM modes, and their predominance is evident by the relative intensity of the H_y and E_z components.

VLF magnetic dipole loop antennas oriented towards the source measure the H_y component; results shown in the remainder of this dissertation thus focus on the H_y component. Note that the model is 2D only, and so is only able to simulate 2D disturbances in the ionosphere, and cannot model scattering in the azimuthal direction.

4.3.1 Simulation of Ionospheric Disturbances

Figure 4.3 illustrates the method for measuring VLF transmitter signal perturbations using the FDFD model described above. First, “ambient” field patterns are computed over the simulation space of interest; in the case of Figure 4.3, this is a path from the NAA transmitter in Maine to a VLF receiver in Parker, Colorado, about 3000 km away, including the realistic ground conductivity parameters along that path. The output ambient H_y field is shown in the second panel. The third panel shows the H_y field amplitude sampled along the ground. This is the amplitude that would be measured by a VLF receiver at any distance from the transmitter; for instance, a receiver at 1000 km along the path would measure H_y to be about -100 dB relative to 1 microTesla, or 10 pT, while a receiver at the end of the path, at 3300 km, would measure -105 dB, or about 6 pT.

The top panel shows the fully-specified 2D electron density used in the model, along with a 1D profile. For the ambient case, the perturbation (labeled as Ionization and Attachment) is not present. To simulate a perturbation, a 2D slice of the 3D electron density change calculated in Chapter 3 is input into the electron density in the top panel as shown. This electron density is manifested through Equations (4.5)

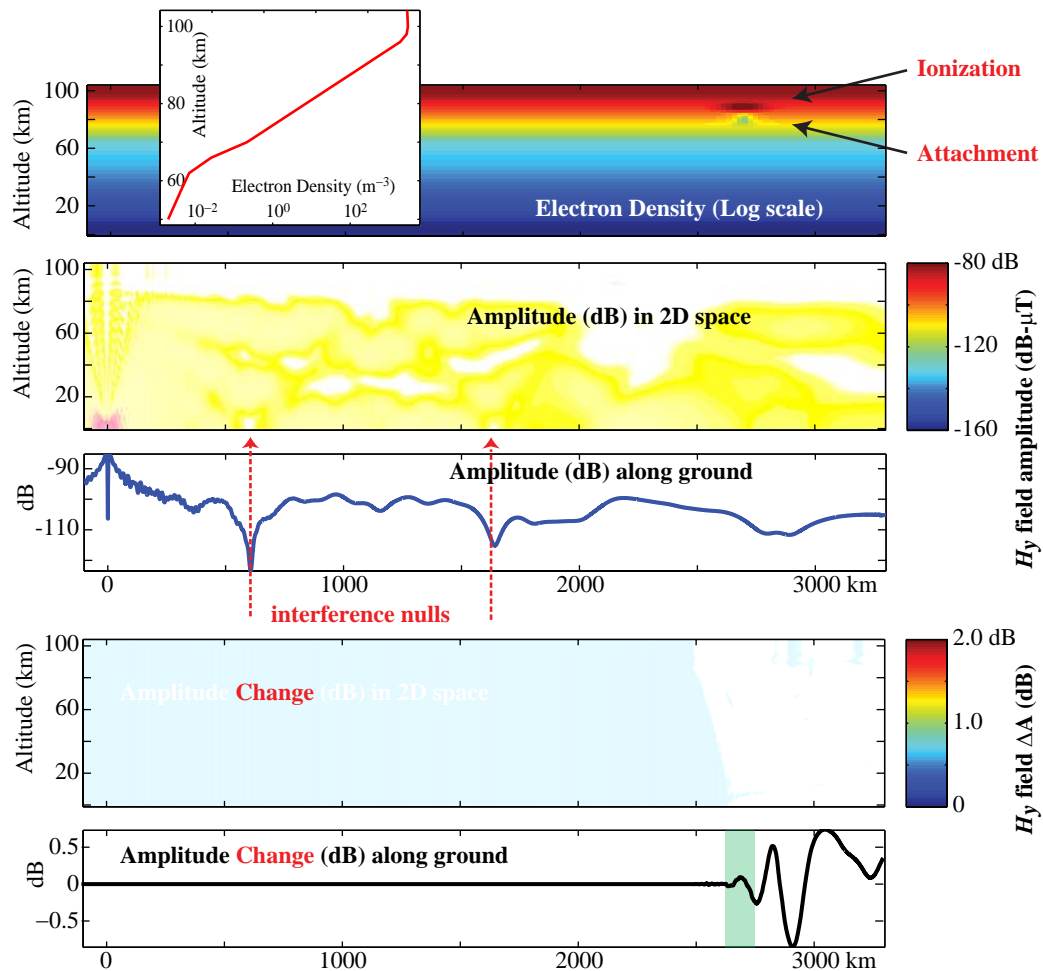


Figure 4.3: Typical perturbation results from the Propagation model. The top panel shows the 2D electron density, with a perturbation imposed 600 km from the end of the path. The 2nd and 3rd panels show the ambient H_y fields in 2D and along the ground, respectively; the 4th and 5th panels show the perturbed fields in 2D and along the ground.

and (4.8) as changes to the 2D conductivity profile, through the modified electron plasma frequency $\omega_{p,e}$. The model is re-run, and outputs similar to the second and third panels are computed. The fourth and fifth panels in Figure 4.3 show the difference between the “ambient” and “perturbed” 2D and 1D (along ground) signals, after converting to dB. These are precisely the “scattered” fields due to the perturbation. The green swath in the fifth panel simply demarcates the disturbance location (although the disturbance is 85 km above). Note that regions of artificially high perturbed amplitude (dB) may appear when the unperturbed field amplitude is low (i.e., near nulls); this problem is discussed in greater detail later in this chapter.

Now, a receiver located at any distance from the transmitter measures an Early VLF perturbation event with amplitude given in the fifth panel. For example, a receiver at 2000 km measures no perturbation, while a receiver located at 3000 km measures as high as a 0.7 dB perturbation.

A comment must be made about the possible use of this model to simulate backscatter, as observed in data in Section 2.2.2. In its present configuration, the SLP model prevents us from accurately measuring backscatter from perturbations. The SLP configuration uses the rightmost fields of one segment as the input to the next segment, but the scattered fields that return to the input (left) side of the segment are not used further. As such, the model calculates scattering in all directions in a single segment, but the backscattered fields are not pursued back into the previous segment. The exclusion of backscatter is not likely to be a problem for these events, however. The perturbations used are all “smooth”, with slowly-varying electron density on scales of 10’s of km (on the order of a VLF wavelength), and so forward scattering is expected, as discussed extensively in Chapter 2. Furthermore, if significant backscatter is excited, one could expect to see a discontinuity in the field pattern (i.e., the fourth panel of Figure 4.3) where the backscattered fields stop without re-entering the previous segment. Such discontinuities are not observed, in Figure 4.3 or any of the examples shown in this chapter. For this reason we conclude that backscatter is not excited by these perturbations.

4.4 Simulation Results

4.4.1 Perturbations from a Single CG Discharge

In Section 3.3, the effects of a single CG discharge interacting with the ionosphere were first presented, yielding the typical “elve” optical emissions and associated electron density changes. *Mika et al.* [2006] and *Mika* [2007] showed that only a subset of elves had associated Early VLF events. From the data presented therein, it is not clear whether the density perturbations underlying elves are due to the EMP (and are thus associated with the elve) or due to associated Quasi-Electrostatic heating or a burst of in-cloud lightning pulses (and hence could instead be associated with a sprite or sferic burst). In fact, a number of the cases studied by *Mika et al.* [2006] and *Mika* [2007] had onset times of up to 2 seconds, suggesting in-cloud sources, as described in Chapter 2. Here, we investigate whether or not the electron density perturbation caused by a single CG discharge could be observed as an Early VLF event.

Figure 4.4 shows simulation results using the single-discharge, vertical EMP results of Figure 3.11, and extending to higher amplitudes of $E_{100} = 35$ and $40 \text{ V}\cdot\text{m}^{-1}$. The top two panels show the ambient 2D and 1D along-ground H_y field amplitude for reference; these panels are repeated in most of the following figures. The lower panels show the 2D scattered H_y field in dB (right) and the 1D along-ground scattered field, ΔA , also in dB (left). In these examples, the propagation path has been extended to 5000 km in order to avoid interference nulls, which may produce artificially high amplitude changes. The path is extended simply to find a region of the simulation space where there are no prominent nulls between the perturbation and the receiver; hence, the region from ~ 3000 to ~ 3700 km would also be appropriate, but would limit the available choice of perturbation locations to ~ 700 km from the receiver. This phenomena of interference nulls and their effect on perturbations is explored in Section 4.4.2 in more detail. Here the disturbance is located 700 km from the receiver end of the path, past the last interference null.

Note that the scattered field patterns for these five simulations show very similar qualitative features, with the amplitude increasing by about a factor of two for each $5 \text{ V}\cdot\text{m}^{-1}$ increase in the input field amplitude. We note that the electron density

changes in Section 3.3 also increased by about a factor of two at each step, so the VLF transmitter signal perturbation here appears to increase approximately linearly with electron density change. Furthermore, upon inspection of the 1D scattered fields at left, the pattern seems to evolve in a regular way from the $E_{100} = 20 \text{ V}\cdot\text{m}^{-1}$ case to the $40 \text{ V}\cdot\text{m}^{-1}$ case; certain fluctuations increase and decrease from one panel to the next.

[Mika, 2007, p. 129] presents a VLF signal perturbation of 0.2–0.4 dB (the exact amplitude change is somewhat difficult to measure) associated with an elve, caused by a +CG of 119 kA (corresponding to $E_{100} \simeq 40 \text{ V}\cdot\text{m}^{-1}$). The results in Figure 4.4 agree very well with these measurements; a maximum ΔA of 0.2 dB is achieved at multiple locations along the path. This helps explain why only a few elves are associated with VLF perturbations [Mika, 2007], since at many locations the amplitude changes would be smaller than detectable levels. The results here demonstrate that only the largest CG strokes can produce measurable perturbations, and thus that only the brightest elves should have associated perturbations; below $35 \text{ V}\cdot\text{m}^{-1}$, the perturbation amplitude is below the measurement threshold. However, in cases where the disturbance is near interference nulls, the amplitude change may reach measurable levels, as investigated in the next section.

It is important to recall at this point, however, that the EMP-induced density changes calculated in Chapter 3 and used here are probably on the lower side, due to the choice of pulse duration (described by the parameter α). For longer pulses, higher density changes may likely occur, and the resulting perturbations to the VLF transmitter signal may be correspondingly greater.

4.4.2 Effects of Perturbation Location

It was postulated in Haldoupis *et al.* [2004] and Marshall *et al.* [2006] that the location of the electron density perturbation along the transmitter–receiver path would affect the presence or lack of an “event” at the receiver. Most of the events analyzed in Marshall *et al.* [2006] came from the HAIL array [Johnson *et al.*, 1999] and the NAA transmitter in Cutler, Maine; the path from NAA to HAIL is around 3000 km,

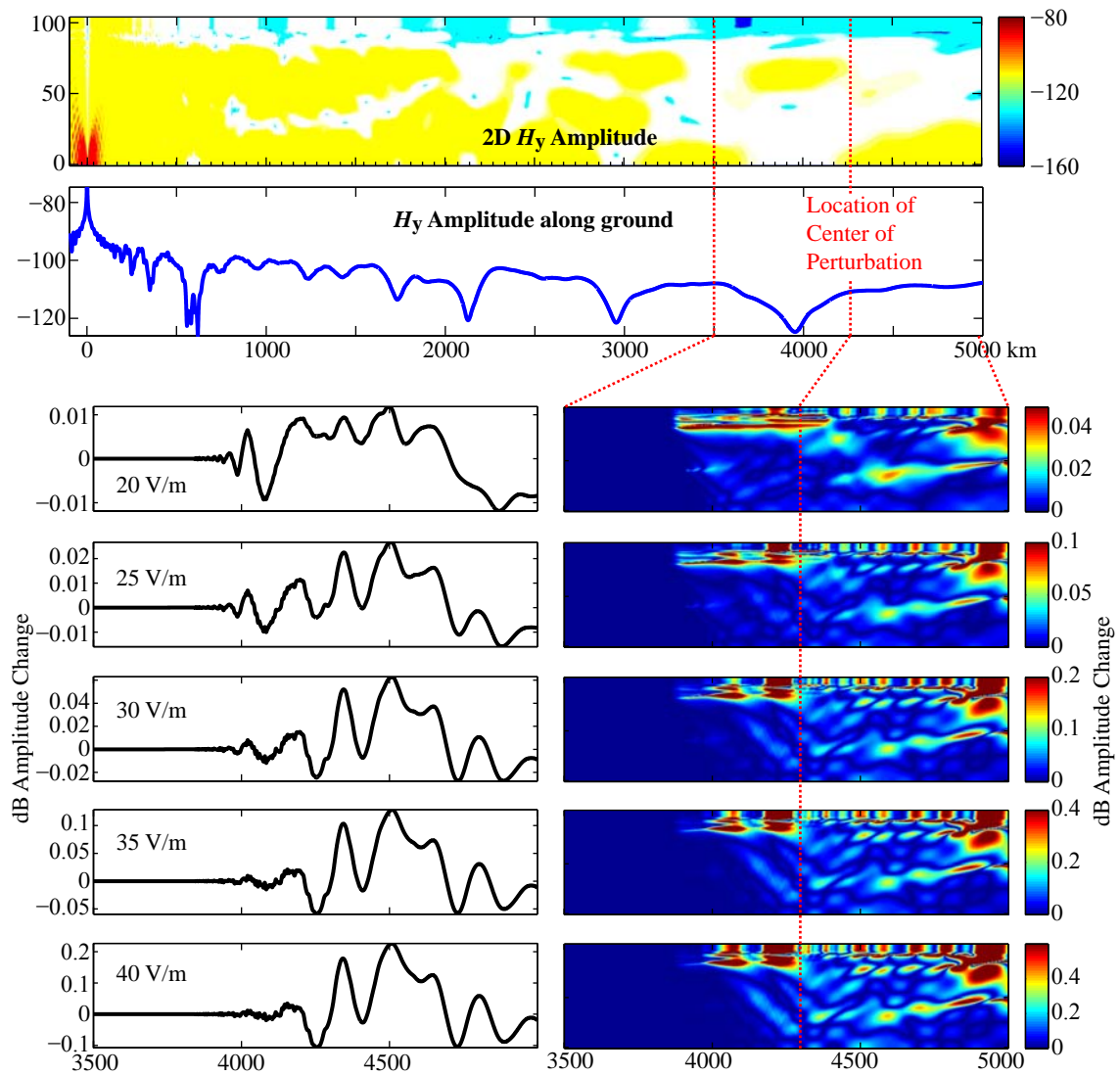


Figure 4.4: VLF transmitter propagation simulation with CG inputs. The top two panels repeat the ambient 2D and 1D along ground amplitudes. The lower panels show the scattered 2D and 1D fields for the EMP cases in Figure 3.11 as well as two more at $E_{100} = 35$ and 40 V-m^{-1} .

and most events were no more than 800 km from the receiver array (as they were generally correlated with sprite observations). These events could thus be labeled “near-receiver” events. On the other hand, *Haldoupis et al. [2004]* analyzed events in Europe that were typically within ~ 500 km of the HWU, HWV and DHO transmitters on which they were observed, while the primary VLF receiver at Crete was some ~ 1500 km away. These events could in turn be labeled “near-transmitter” events. This difference could then account for the difference in correlation between these two data sets: whereas *Haldoupis et al. [2006]* found a “one-to-one” correlation between sprites and Early VLF events, *Marshall et al. [2006]* found that closer to $\sim 60\%$ were correlated.

The lower-left five panels of Figure 4.5 show the change in amplitude along the ground due to perturbations in the ionosphere centered 500, 1000, 1600, 2000, and 2600 km from the receiver. In each of these panels, the green swath marks the lateral location of the perturbation, as in Figure 4.3. The disturbance itself (i.e., the electron density change) is the same as used in Figure 4.3. In each case, the disturbance in the ionosphere is identical. The top two panels simply repeat the ambient 2D and 1D along-ground amplitudes in order to see the alignment of interference nulls. The results shown are for the NAA transmitter signal to a VLF receiver at Parker, Colorado. The table at right shows the amplitude change at the receiver and the maximum amplitude achievable, measured at the red dashed lines.

This example demonstrates that the perturbation and receiver locations play a strong role in determining the received amplitude perturbation. The 1000 km case shows almost zero received ΔA and a small maximum ΔA , because the perturbation falls in the middle of a strong-signal region. The 1600 km case, on the other hand, falls near an interference null, yielding a very high maximum ΔA . In the longer cases, the maximum ΔA happens at the interference null as the scattered signal passes over it. Note that for most of the data presented in Chapter 2, the disturbances fall in the 500–1000 km range from the receiver, on a path of about this length. Note also that interference between the scattered modes makes the received amplitude change difficult to predict, as it varies from positive to negative (and passes through zero) at multiple locations along the path.

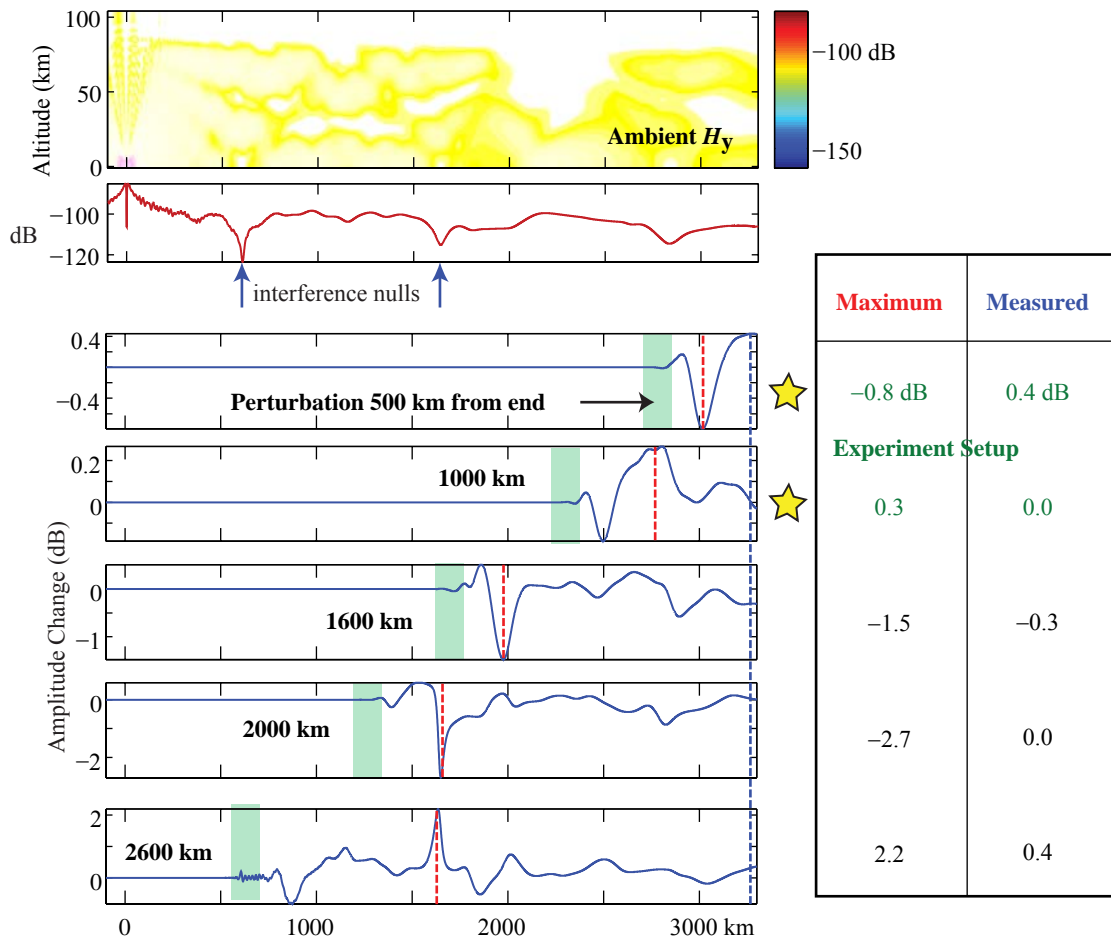


Figure 4.5: Effect of perturbation location on received amplitude. The top two panels show the ambient H_y field in 2D and along the ground. Below, five simulations are shown with perturbations at different distances measured from the receiver (right end, blue dashed line). The red dashed line on each plot shows where the maximum perturbation occurs; these values are tabulated at right. The first two cases (starred), with perturbations at 500 and 1000 km from the receiver, correspond to the experiments in Chapter 2.

4.4.3 Effects of Transmitter Frequency

Equations (4.1) and (4.2) suggest that the interference patterns of the electric and magnetic fields are affected significantly by the transmitter frequency. Furthermore, Figure 1.4 shows that different frequencies will reflect at slightly different altitudes, and so lower frequency transmitters may probe the higher-altitude regions of the electron density disturbances in Chapter 3 with greater efficiency. However, this effect is likely to be small, as the reflection height changes only very slightly over the frequency range of lightning pulses.

Figure 4.6 shows the 2D and 1D along-ground H_y field amplitudes for transmitter frequencies from 18 kHz to 30 kHz, in 2 kHz increments. The VLF transmitters most commonly used range from 18.6 to 25.2 kHz, as listed in Table 1.2, with a few exceptions at 35–40 kHz. While the actual transmitters each have their own distinct location around the globe, each of the simulations in Figure 4.6 uses the path from the NAA transmitter location in Maine to a receiver in the direction towards Colorado (and beyond), in order to isolate the effect of the transmitter frequency.

Similar to Figure 4.4, Figure 4.6 shows that the qualitative properties of the transmitter signal vary in a regular way as the frequency is increased. The interference nulls, both along the ground and in the 2D pattern, tend to move farther from the transmitter as the frequency is increased, as demarcated by the red dashed lines. Furthermore, some nulls disappear altogether, while others appear at higher frequencies only. Ultimately this behavior shows that the choice of frequency has a strong influence on the ambient signal amplitude at a given receiver, simply due to the locations of interference nulls.

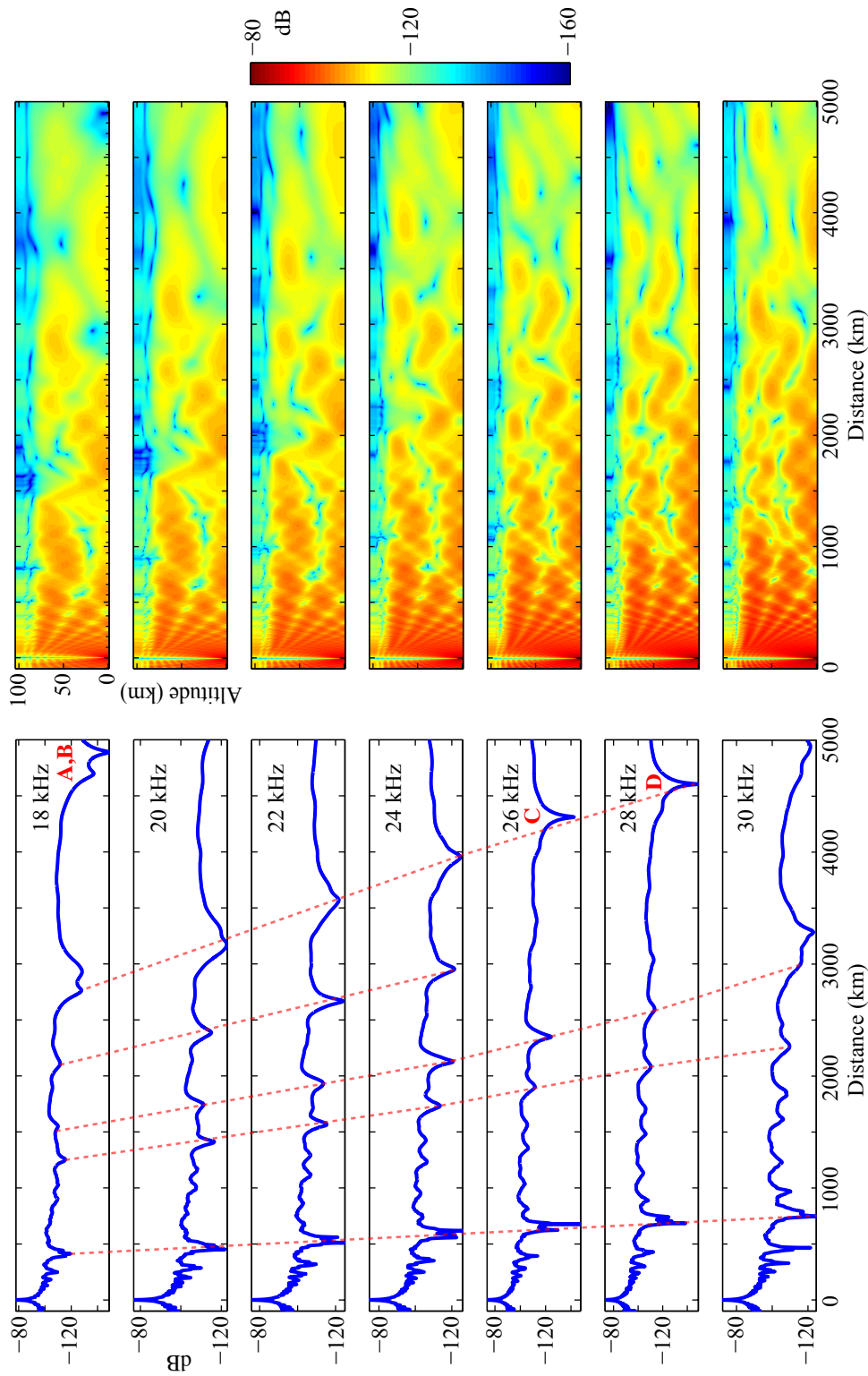


Figure 4.6: VLF signal amplitudes in 2D and 1D along ground for a variety of transmitter frequencies, corresponding to the typical range of 18–30 kHz used for most VLF transmitters. The red dashed lines show how the location of nulls varies with frequency; the labels A–D correspond to null locations to be discussed with Figure 4.7.

Figure 4.7 shows the results of perturbation simulations using the same frequencies. Each of these uses the electron density disturbance from the $E_{100} = 40 \text{ V}\cdot\text{m}^{-1}$ vertical discharge case that is also used in the last panel of Figure 4.4; hence the fourth panel in Figure 4.7, the 24 kHz case, is a repeat of the last panel of Figure 4.4.

Results show that the perturbations depend strongly on the transmitter frequency, exhibited in a number of ways. First and most obvious is the presence or lack of interference nulls. In Figure 4.6, the labels A–D are used to point out prominent interference nulls near the receiver end of three of these paths. In Figure 4.7, at the locations of the nulls A–D we see prominent spikes in the scattered amplitude, exactly as seen in Figure 4.5. In the 18 kHz case, the locations marked A and B jump to over 1 and 2 dB respectively. In the 26 and 28 kHz cases, the amplitudes reach over 5 dB. This large value is consistent with the depth of the interference nulls seen in Figure 4.6. Figure 4.7 zooms in on these perturbations for the following discussion.

Apart from the interference nulls, the received amplitude change ΔA is also affected more simply by the transmitter frequency because of the different mode interference in the transmitter signal. Hence, while the 20 kHz case shows a maximum perturbation of only 0.08 dB, the 30 kHz can reach 0.6 dB. While this figure deceptively appears to yield a trend of higher frequency yielding stronger perturbations, other simulations not shown here, with different paths and different electron density disturbances, show this not to be the case. In fact, there seems to be no frequency that is any “better” than any other at producing measurable perturbations.

4.4.4 Perturbations from Sequences of IC discharges

At the end of Chapter 3, in Section 3.3.4, the hypothesis was put forth that many Early VLF perturbations could be the signature of electron density changes induced by a sequence of many in-cloud lightning discharges. In this section, that hypothesis is tested.

The 3D perturbations calculated in Section 3.3.4, and shown in Figure 3.20, are imposed on the 2D electron density here as described in Section 4.3.1 by taking a slice through the center of the disturbance. In the results shown in this section,

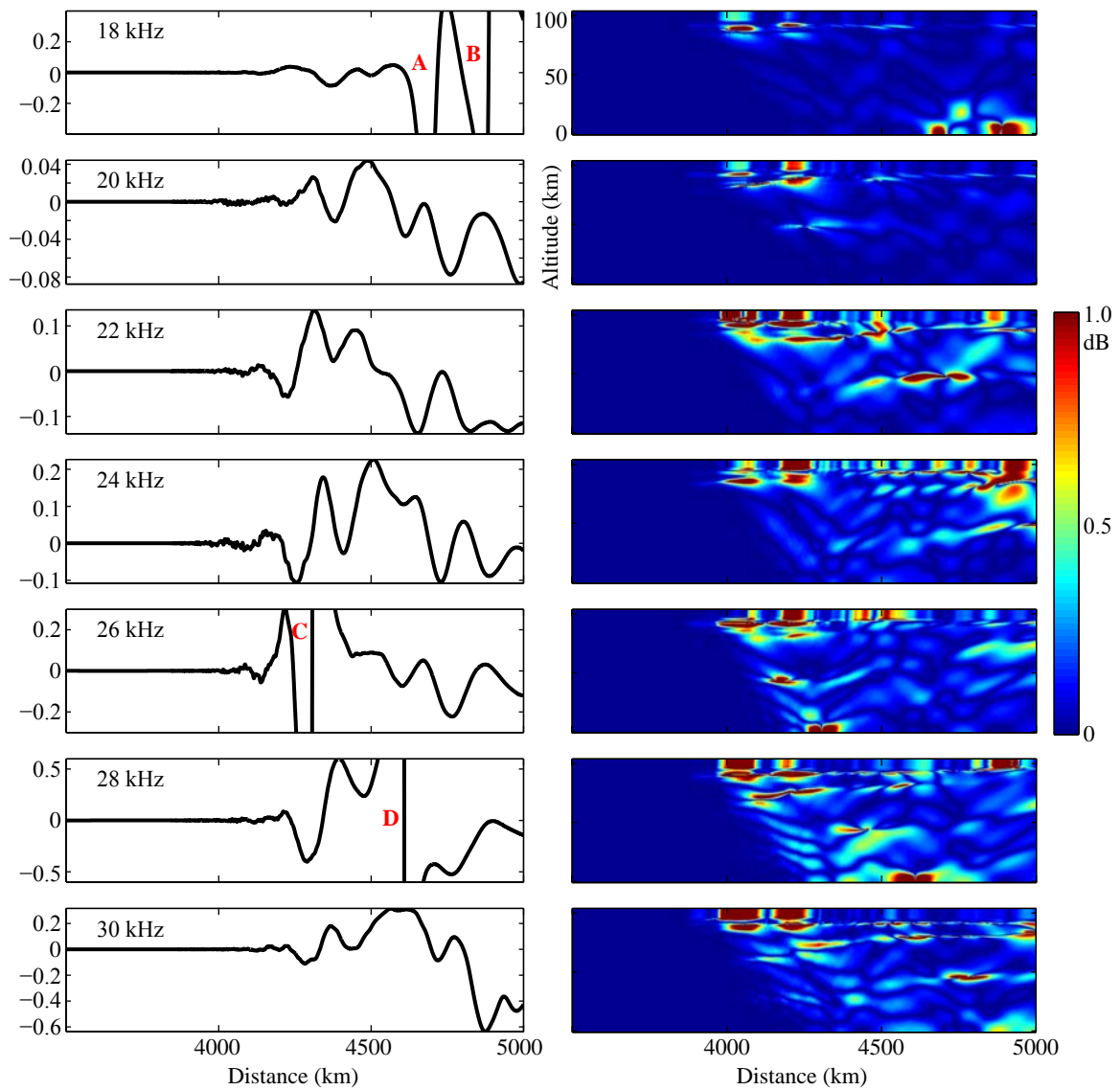


Figure 4.7: Effect of transmitter frequency on received amplitude. The left panels show the 1D amplitude along the ground for simulations from 18 kHz to 30 kHz in 2 kHz increments; at right, the 2D scattering patterns. The labels A-D correspond to the locations of prominent interference nulls in the ambient field pattern.

the slice is taken in the plane of the Earth's magnetic field \mathbf{B}_0 . Figure 4.8 shows results for the 5000 km long simulation space with a transmitter frequency of 24 kHz, where interference nulls have been avoided as described above; the electron density disturbance has again been placed 700 km from the receiver end of the simulation space.

While the 1D and 2D patterns have greater variation than in Figure 4.4, there again seems to be considerable consistency in the mode interference pattern, especially for the $E_{100}^{\text{ic}} = 7 \text{ V}\cdot\text{m}^{-1}$, $10 \text{ V}\cdot\text{m}^{-1}$, and random cases. Once again, we see that the amplitude change ΔA becomes both positive and negative, and is zero in places. However, except for the $E_{100}^{\text{ic}} = 5 \text{ V}\cdot\text{m}^{-1}$ case, the absolute amplitude changes are in the measurable range, with the $7 \text{ V}\cdot\text{m}^{-1}$ case reaching 0.2 dB in places. Note, again, that this 5000 km long path is designed to avoid artificially high ΔA measurements due to nulls (by using a region of the simulation space where there are no interference nulls between the perturbation and the receiver), and so amplitude changes shown here are likely to be at the lower end of observed values.

To compare with real data, Figure 4.9 places the same electron density change 500 km from the receiver end of a 3000 km path; this is the setup from the NAA transmitter in Maine to Parker, CO, including the real values of ground conductivity along that path. The ambient 2D and 1D fields are identical to the first 3000 km of the previous simulation in Figure 4.8. Note that an interference null is present very close to the receiver; as such we might expect large ΔA values at the receiver.

The simulation results indeed show the expected large amplitude changes. Right at the interference null, where the signal amplitude is low, the relative change in amplitude in dB is very high, reaching 0.2 dB even for the $5 \text{ V}\cdot\text{m}^{-1}$ case, and 1 dB and higher for the $7 \text{ V}\cdot\text{m}^{-1}$, $10 \text{ V}\cdot\text{m}^{-1}$, and the random cases. Exactly at the receiver the ΔA drops considerably as the signal amplitude is larger, but the measured values are still 0.3 dB, 2 dB, and 1 dB for the $7 \text{ V}\cdot\text{m}^{-1}$, $10 \text{ V}\cdot\text{m}^{-1}$, and the random cases, respectively. The conclusion we draw from this result is that some of the perturbations measured by the HAIL array may be accounted for by relatively small electron density changes, but enhanced ΔA due to proximity to the interference null. However, it is important to note that the location of this null is sensitive to the ground

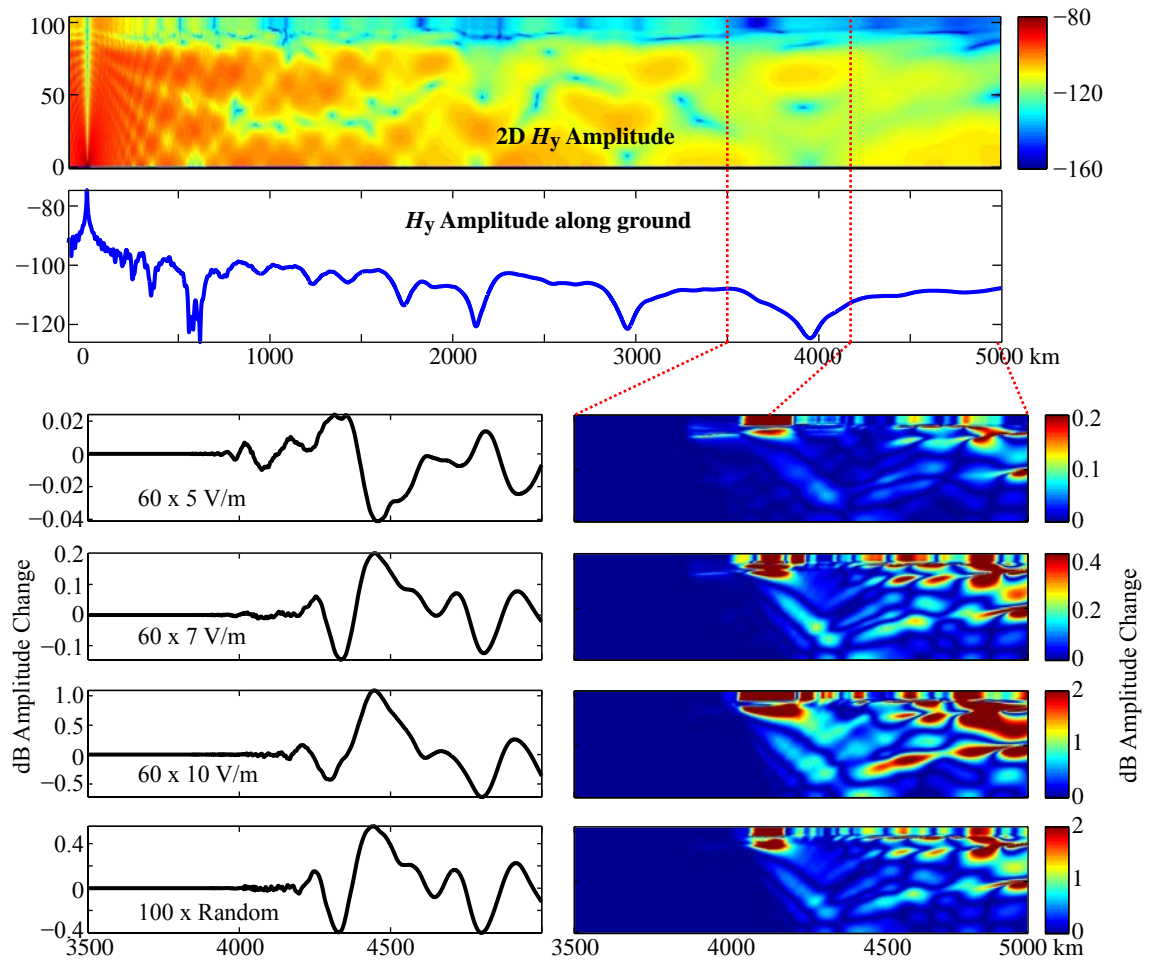


Figure 4.8: VLF transmitter propagation simulation with EMP multi-pulse inputs. The top two panels repeat the ambient 2D and 1D along ground amplitudes. The lower panels show the scattered 2D and 1D fields for the four cases in Figure 3.20.

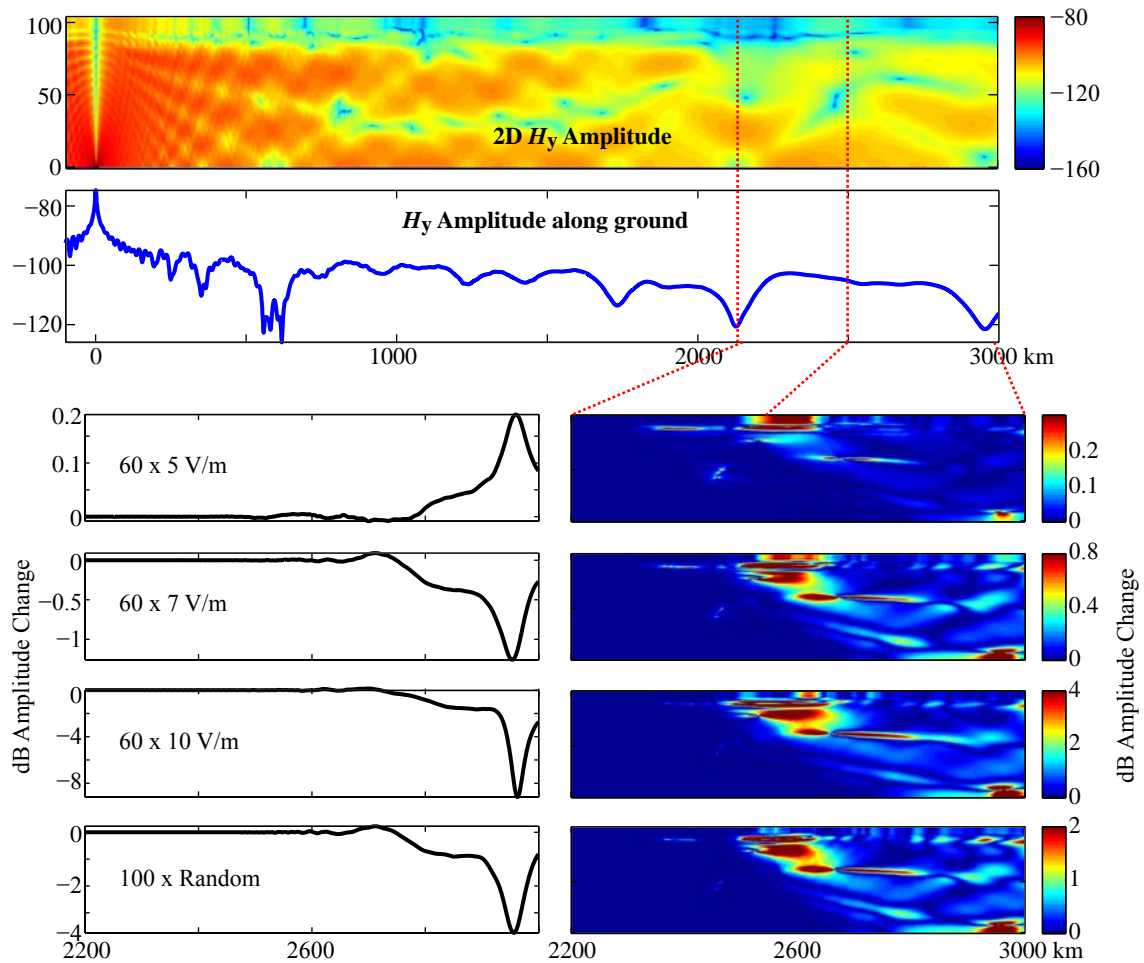


Figure 4.9: VLF transmitter propagation simulation with EMP multi-pulse inputs on a realistic 3000 km HAIL path. The top two panels repeat the ambient 2D and 1D along ground amplitudes. The lower panels show the scattered 2D and 1D fields for the four cases in Figure 3.20. Compared to Figure 4.8, in this case the path is only 3000 km and the perturbation is 500 km from the receiver.

and ionosphere parameters, as well as the transmitter frequency, as shown in Figure 4.6, and thus the actual location may be difficult to predict for any particular event. Furthermore, each of the HAIL paths have slightly different path lengths and ground and ionosphere conditions, so each path would have its own null location.

4.5 Discussion and Conclusions

The main conclusion of this chapter is that electron density disturbances in the lower ionosphere caused by sequences of in-cloud pulse discharges may be measurable by VLF techniques; and thus, that many Early VLF events may be the signature of sferic burst-associated electron density changes in the lower ionosphere. This scenario is most likely the case for Early/slow events; the longer rise time of these events corresponds very well with the duration of sferic bursts, suggesting that the latter is responsible for the former.

The second major conclusion of this chapter is that the received amplitude, as well as its polarity (discussed in the following subsection), is strongly dependent on a number of parameters; in particular, the path length, ionospheric and ground parameters, and transmitter frequency all affect the received amplitude very nonlinearly. Furthermore, recall the results of Chapter 3, wherein it was found that the electron density disturbance is very nonlinearly related to the parameters of the constitutive pulses in a sferic burst, including altitude, pulse duration (i.e., speed), orientation, latitude, and amplitude. These parameters are difficult, if not impossible, to measure completely in a particular sferic burst event. As such, the two processes modeled in Chapter 3 and the present chapter together show the importance of modeling in understanding and quantifying these processes. Qualitatively, this modeling work has shown that these in-cloud bursts, of which sferic bursts are the VLF signature, may account for many observed Early/fast and Early/slow VLF perturbations.

4.5.1 Polarity of Early VLF Events

A detailed review of prior work on Early/fast events shows that the vast majority have positive polarity amplitude changes; i.e., ΔA is almost always positive. In [Inan and Rodriguez \[1993\]](#), all 33 Early/fast events were positive perturbations, while all 22 lightning-induced electron precipitation (LEP) events had a negative amplitude perturbation. Precipitating energetic electrons produce purely an increase in electron density [[Peter and Inan, 2005](#)] through impact secondary ionization from energetic electrons. In [Inan et al. \[1993\]](#), data was shown for different dates, with the same

results: every LEP event has a negative amplitude change, while every early/fast event has a positive change. Similarly, *Inan et al.* [1996d] reported about 29 positive VLF perturbations versus 10 negative events. Note that the results cited here provide a variety of transmitter–receiver paths, so the trend exhibited is not likely to be specific to a particular combination.

Figure 4.10 shows histograms of Early VLF events from 15 July 1995, 18 August 1999, and 22 July 2000, presented and discussed in *Marshall et al.* [2006] and in Chapter 2. Many of the largest Early VLF events are negative perturbations (bottom panel); indeed, a quick inspection of Figures 2.4 and 2.8 herein seems to signify a prevalence of large negative perturbations (some of which are actually LEP events). However, there are far more small positive perturbations, as especially evident in Figure 2.8.

The data summarized above occur over a wide variety of transmitter signals and paths, to a variety of receivers; as such, the trend cannot be attributed to a particular transmitter–receiver geometry. Despite the overwhelming predominance of positive-polarity Early VLF events in the data, the simulation results in this chapter do not seem to agree with this trend. Rather, the results in Figures 4.4, 4.8 and 4.9 back up the argument of significant mode interference, and show that the received amplitude (and presence or lack of a registered “event”) strongly depends on the relative locations of the transmitter, disturbance, and receiver. Hence, the prevalence of positive-polarity Early VLF events remains unexplained.

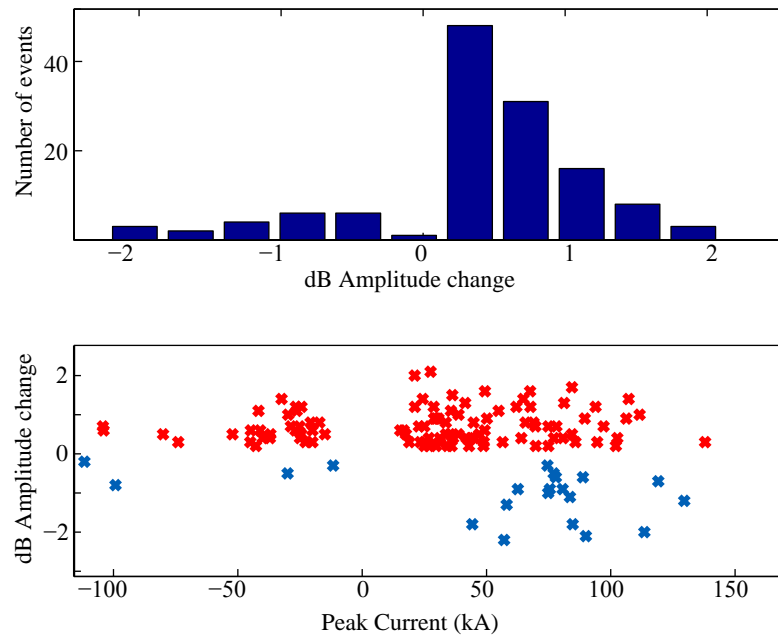


Figure 4.10: Top: Histogram of dB perturbation amplitudes of Early VLF events from 15 July 1995, 18 August 1999, and 22 July 2000, showing a predominance of small, positive amplitude changes. Bottom: Early VLF amplitude changes versus their causative peak currents, showing that most small perturbations are caused by small peak currents <100 kA; a few of the larger perturbations, and especially the negative perturbations, are associated with the rare, large peak currents.

Chapter 5

Summary and Suggestions for Future Research

5.1 Summary of Results

This work has presented a complete theory of Early VLF event production, from the origins of the hypothesized mechanism in VLF and sprite data, to quantitative calculations of the effects of lightning on the lower ionosphere, and finally model calculations of the perturbations to VLF transmitter signals.

Chapter 1 presented an introduction to the important physical concepts, beginning with an introduction to the Earth's ionosphere and its composition. Section 1.2 described important parameters of lightning as it relates to VLF and optical phenomena, with an emphasis on in-cloud lightning. Next, the Earth-ionosphere waveguide was introduced, and the formation of this waveguide between the conducting Earth surface and the conducting lower ionosphere was described. In Section 1.4, Transient Luminous Events were introduced, including sprites, elves, and jets; it was shown that sprites are a product of the quasi-electrostatic (QE) field from lightning, while elves are a signature of the electromagnetic pulse. Section 1.5 discussed VLF signatures of lightning and the effects of propagation path on the observed sferic, and Section 1.6 introduced narrowband VLF transmitter signals and “Early VLF” perturbations to these transmitters.

Chapter 2 described the observational connections between sprites and Early VLF events, and between sprites and sferic bursts. In a study published by *Marshall et al. [2006]*, it was shown that over the course of four summers, about 48% of sprites had associated Early VLF events, while 60% of Early VLF events has associated sprites; this means that the two phenomena are strongly linked, but one can occur without the other, suggesting sometimes different mechanisms. Next, work published in *Marshall et al. [2007]* was summarized, in which sprites and sferic bursts were correlated. Again, it was shown that while sprites are commonly associated with much higher sferic burst energy than non-sprite CGs, a good number of sprites (about 22%) occur without any sferic burst activity.

These two correlations reinforce the overall picture of sprite production as first put forth by *Pasko et al. [1995]*. Sprites are produced by the QE field that is released by charge removal in a CG lightning stroke. The weak connection with Early VLF events suggests that the QE field cannot be solely responsible for Early VLF event production. It was shown in Section 2.3.3 that sferic bursts are the VLF signature of in-cloud lightning; when associated with a CG discharge, this IC activity serves to “tap” the thundercloud charge, contributing to the cumulative charge removal through continuing current. This enhances the QE field, leading to sprite production; hence the strong correlation between sferic bursts and sprites. However, a large number of sprites are produced when the impulsive charge moment (the charge moment in the first 2 ms) is large enough as to not require continuing current.

Chapter 2 concluded by introducing a new mechanism for Early VLF event production, through the EMP pulses emitted by successive in-cloud lightning components. It was proposed that these EMPs can create a cumulative disturbance in the lower ionosphere through changes in electron density due to electron impact ionization and dissociative attachment. This new mechanism suggests that Early/slow and Early/fast events are not distinct, but rather form a continuum of events based on the duration of the sferic burst activity.

Chapter 3 began the process of testing this hypothesis by modeling the EMP–ionosphere interaction. A 3D FDTD model was used, in which an EMP pulse is propagated upwards into a realistic ionosphere. Collision frequency, ionization and

attachment rates, and optical excitation rates are calculated self-consistently, and fields are updated to include self-absorption of the propagating wave. The model was used to simulate CG lightning as well as in-cloud lightning. Altitude, amplitude, dipole orientation, magnetic field orientation, and ionospheric profiles were varied to test their effects. It was shown that realistic single CG pulses can have a significant effect on the lower ionosphere, with electron density changes from a fraction of a percent up to tens of percent. Finally, sequences of in-cloud pulses were simulated to show that successive EMPs from sferic bursts can have a significant cumulative effect on the ionosphere, up to hundreds of percent increase in electron density.

To quantitatively test whether these simulated electron density changes could be detected as Early VLF events, Chapter 4 presented simulations using an FDFD model of the VLF transmitter signal propagation in the Earth-ionosphere waveguide. The modified electron density profiles from Chapter 3 were input into the model in 2D, and the resulting scattering pattern was computed. The scattered field observed on the ground at a particular location gives the Early VLF event “amplitude”. It was shown that only the largest individual CG strokes yield perturbations large enough to be observed, while the disturbances caused by sequences of pulses create perturbation magnitudes of the transmitter signals that are consistent with observations.

5.2 Suggestions for Future Research

In this section we describe some suggestions for improvements to the current work, and suggestions for future research.

5.2.1 Improving the EMP model

The EMP model in its current state works well for the limited applications described in this work, but is restricted by a number of features that could hinder future applications. The method used has great potential for modeling effects of both lightning and VLF transmitters on the lower ionosphere, as well as looking to higher altitudes

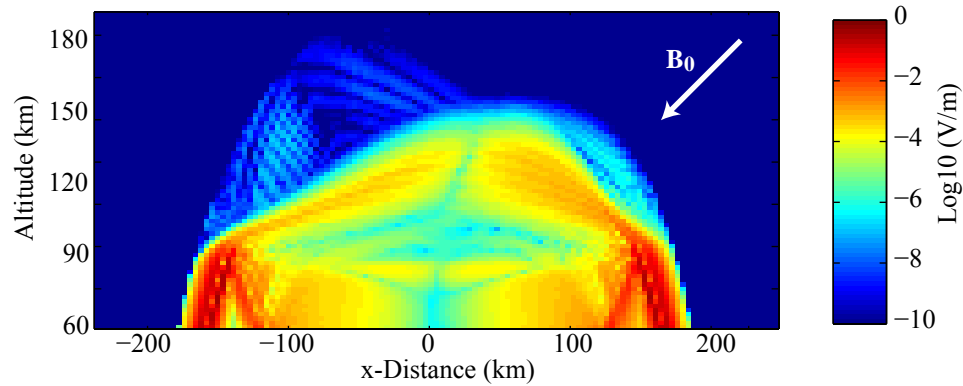


Figure 5.1: Snapshot of the Electric Field magnitude from the EMP model, from 60 to 185 km altitude. One can easily observe reflections from the ionosphere as well as propagation through the ionosphere, dispersion and guiding along the Earth’s magnetic field.

and transionospheric propagation into the magnetosphere. Figure 5.1 shows the simulated Electric field magnitude from 60 km to 185 km altitude, repeated from Figure 3.9, at a snapshot late in the simulation. In its current configuration, the model extends to higher altitudes simply to avoid reflections from an upper boundary; however, the fields at these higher altitudes could yield great insight into the process of transionospheric propagation. Three modifications to the model may vastly extend its uses:

1. *Incorporation of Total-Field/Scattered-Field.* Currently, we impose the input fields along the lower boundary at 60 km altitude and allows them to propagate upwards into the simulation space. Reflections from the lower ionosphere reach this lower boundary very quickly; the current technique is to replace the lower boundary input fields with a simple Absorbing Boundary Condition (ABC) after the pulse is completely within the space. This method limits the pulsewidth (corresponding to the parameter α) that can be simulated; longer pulses would not be completely in the space before the reflection reaches the boundary. This problem can be circumvented by lowering the boundary, but that in turn increases the computation time and simulation space. Note also that simulating lightning source pulses at an altitude above ground has the effect of further

increasing the pulse width, because the reflected pulse takes longer to enter the space.

A simple solution to this problem exists, but requires major changes to the code, and has not yet been incorporated. This improvement involves incorporating the Total-Field/Scattered-Field (TF/SF) technique to impose the input fields [Umashankar and Taflove, 1982]. In this method, the input fields are “added” to the standard update equations at a plane that is a few cells above the lower boundary. This plane is then transparent to reflected waves, and so input fields can continue to be driven while reflections pass through the plane. Then, a few cells below at the lower boundary, a simple ABC or PML can be easily incorporated. This improvement would eliminate any restrictions on the input pulse parameters and would allow us to limit the lower boundary of the numerical space to 70 km.

2. *Incorporation of Absorbing Boundary Conditions.* Currently, the model does not incorporate absorbing boundary conditions, except at the lower boundary as described above. The inclusion of ABCs on the side and top walls of the simulation space could greatly enhance the range of applications. In the model’s present state, calculated fields are only valid up until the time when reflections from the boundaries of the numerical space occur. Typically in the FDTD method, a Perfectly Matched Layer (PML) would be included at the boundaries to absorb outgoing waves. However, in an anisotropic medium such as a magnetized plasma, problems arise with the PML, as described by *Chevalier et al.* [2008] and in Section 4.3. In an anisotropic medium, the k -vector is not necessarily parallel to the direction of energy propagation (the group velocity vector, v_g). The PML is designed to absorb waves in the direction of k -propagation; however, cases arise (typically on walls parallel to \mathbf{B}_0) where \vec{v}_g points into the PML, but \vec{k} points *out of* the PML, and rather than decaying, the wave grows exponentially upon entering the PML.

For this reason no PML has been used in this code. A method has been developed by *Chevalier et al.* [2008] that incorporates information about the k -vector direction into the PML implementation, as described in Section 4.3. This method could potentially be used in our model as an effective ABC. Alternatively, it may be possible to use the Higdon operator [*Higdon*, 1986, 1987] as a simple ABC. This operator absorbs waves at particular incident angles, given a known source location; for the outgoing impulse EMP, one can easily define the incident angle at any point on the simulation space boundary.

3. *Inclusion of Chemical Effects.* In the same way that we calculate electron mobility, ionization and attachment rates self-consistently as the electric field changes, the model could be modified to calculate field-driven chemical reaction rates for updates of ion species densities, by including the atmospheric chemistry model developed by *Inan et al.* [2007b] and *Lehtinen and Inan* [2007]. Some of the appropriate reaction rates are catalogued in *Sentman et al.* [2008], wherein they were used to study chemical effects in sprite streamers. In this way, the EMP model could accurately track specific ion species and study the effects of the EMP on the ionospheric composition, such as ozone density.

5.2.2 Use of the EMP Model for Transionospheric Propagation

As mentioned at the beginning of this section, with the first two improvements described above, the EMP model could be used to study transionospheric propagation. Currently, this is a problem typically studied with full-wave methods [*Lehtinen and Inan*, 2009], where the ionosphere is stratified in altitude, but these methods cannot vary the ionosphere in 3D and are restricted to a single frequency. The EMP model presented in Chapter 3 self-consistently propagates waves with three components each of \vec{E} and \vec{H} into and through the ionosphere in the time domain. Using this complete description of the fields, one can gain insight into the ordinary and extraordinary modes propagating into the magnetosphere, as well as a measure of the amplitudes injected as a function of the source current amplitude and direction.

Unlike the *Lehtinen and Inan* [2009] full-wave code, our 3D model could also study the effect of previous electron density disturbances on transionospheric propagation of subsequent impulses.

5.2.3 Early VLF and TLEs with Photometric Imaging

One of the drawbacks of our observational work in Chapter 2 is that camera images do not always detect sprites, and much less often elves, which may be below the instrument detection threshold. This is plainly seen by the fact that elves are seen to outnumber sprites over 6:1 in satellite images [*Chen et al.*, 2008], but are rarely observed from the ground.

Photometric imaging can solve this problem from the ground, allowing for more accurate correlations between Early VLF events and TLEs. A photometric imaging instrument such as the Photometric Imager of Precipitation of Electron Radiation (PIPER) instrument developed at Stanford [*Marshall et al.*, 2008b] can easily detect all but the weakest elves, and with its low-resolution imaging capabilities, can unambiguously distinguish between elves, halos and sprites. With such observations, some of the outstanding questions from Chapter 2 can be answered: is there a TLE (either a sprite, halo, or elve) for *every* Early VLF event? Are there “flashing elves” (a concept introduced in Section 3.4) associated with spheric bursts? Using observations of elves in multiple wavelength bands, such a photometric imaging instrument can also measure the modified electron energy distribution, and thus be used to make estimates of the level of ionization associated with elves, using the same method as *Mende et al.* [2005a]. These estimates can then be compared with the results from Chapter 3.

Appendix A

EMP Model Formulation

This appendix presents the detailed methodology involved in the EMP model presented in Chapter 3. Some of the derivation is repeated here for continuity.

The EMP code self-consistently solves Maxwell’s equations and the Langevin equation, presented in Equations (3.4) to (3.6), and repeated here:

$$\nabla \times \vec{E}_w = -\mu_0 \frac{\partial \vec{H}_w}{\partial t} \quad (\text{A.1})$$

$$\frac{\partial \vec{J}}{\partial t} + \nu_e \vec{J} = \epsilon_0 \omega_p^2 \vec{E}_w + \vec{\omega}_b \times \vec{J} \quad (\text{A.2})$$

$$\nabla \times \vec{H}_w = \epsilon_0 \frac{\partial \vec{E}_w}{\partial t} + \vec{J} \quad (\text{A.3})$$

A.1 Input Fields

Rather than solving Equations (A.1) to (A.3) in a 3D space that includes the ground and the input current, the model solves the fields from a lower boundary (usually 60–70 km) to an upper boundary high above the ionospheric layers of interest (usually 175–200 km). The fields at the lower boundary are calculated analytically at each time step and used as an “input” to the model. This serves to reduce the size of the computation space and more realistically model the source current. The equations to solve at the boundary are radiation equations for a small dipole. These equations

are found in many textbooks, typically in frequency domain for a z -directed current. In our formulation, we need the time domain equations, which are derived from the Hertz vectors in [*Budden, 1961*, p. 43]:

$$E_r = \frac{1}{2\pi\epsilon_0} \sin \theta \left(\frac{[M]}{r^3} + \frac{1}{cr^2} \frac{\partial[M]}{\partial t} \right) \quad (\text{A.4})$$

$$E_\theta = \frac{1}{4\pi\epsilon_0} \cos \theta \left(\frac{[M]}{r^3} + \frac{1}{cr^2} \frac{\partial[M]}{\partial t} + \frac{1}{c^2 r} \frac{\partial^2[M]}{\partial t^2} \right) \quad (\text{A.5})$$

$$H_\phi = \frac{1}{4\pi\epsilon_0} \cos \theta \left(\frac{1}{cr^2} \frac{\partial[M]}{\partial t} + \frac{1}{c^2 r} \frac{\partial^2[M]}{\partial t^2} \right) \quad (\text{A.6})$$

$$E_\phi = H_r = H_\theta = 0$$

where $[M]$ denotes the “retarded” value of the dipole moment M , $d\mathbf{M}/\Delta t = i\mathbf{l}$, and i and \mathbf{l} and the current magnitude and current channel vector respectively; thus for a given $M(t)$, $[M] = M(t - r/c)$.

To solve for a general source dipole orientation (x , y and z components), we simply solve these equations for each component, and for the x and y components we apply a rotation to the results. Note also that cloud-to-ground (CG) discharges radiate primarily from the ground, and so the CG discharge is modeled here as a monopole on the ground, which has the same field pattern as a small dipole with no ground reflection. For in-cloud discharges we model a small dipole at some altitude and include an effective image dipole below ground.

For the simulations shown in this work, the current is modeled by

$$I(t) = I_0 \frac{2e^{\alpha t}}{1 + e^{2\alpha t}} = I_0 \cosh^{-1}(\alpha t)$$

where the parameter α controls the temporal width of the current pulse; this yields

$$\begin{aligned} M(t) &= \frac{Ih}{\alpha} \tan^{-1}(e^{\alpha t}) \\ \frac{\partial M(t)}{\partial t} &= Ih \frac{e^{\alpha t}}{1 + e^{2\alpha t}} \\ \frac{\partial^2 M(t)}{\partial t^2} &= Ih\alpha \frac{e^{\alpha t} - e^{3\alpha t}}{(1 + e^{2\alpha t})^2} \end{aligned}$$

Typical values of α are presented in Chapter 3; for reference, a pulse with $\alpha = 10^5$ s⁻¹ has a full-width at half-maximum (FWHM) of ~ 20 μ s.

A.2 Magnetic field Update Equations

Equation (A.1), the magnetic field update equation, is solved using standard second-order centered-differencing:

$$B_x|_{i,j+1/2,k+1/2}^{n+1/2} = B_x|_{i,j+1/2,k+1/2}^{n-1/2} + K_z \left(E_y|_{i,j+1/2,k+1}^n - E_y|_{i,j+1/2,k}^n \right) - K_y \left(E_z|_{i,j+1,k+1/2}^n - E_z|_{i,j,k+1/2}^n \right) \quad (\text{A.7})$$

$$B_y|_{i+1/2,j,k+1/2}^{n+1/2} = B_y|_{i+1/2,j,k+1/2}^{n-1/2} + K_x \left(E_z|_{i+1,j,k+1/2}^n - E_z|_{i,j,k+1/2}^n \right) - K_z \left(E_x|_{i+1/2,j,k+1}^n - E_x|_{i+1/2,j,k}^n \right) \quad (\text{A.8})$$

$$B_z|_{i+1/2,j+1/2,k}^{n+1/2} = B_z|_{i+1/2,j+1/2,k}^{n-1/2} + K_y \left(E_x|_{i+1/2,j+1,k}^n - E_x|_{i+1/2,j,k}^n \right) - K_x \left(E_y|_{i+1,j+1/2,k}^n - E_y|_{i,j+1/2,k}^n \right) \quad (\text{A.9})$$

where K_x , K_y , and K_z are the respective normalization coefficients in terms of c , Δt , Δx , Δy and Δz . Note that this method uses the normalized fields E and B rather than E and H . The superscript n refers to the time step; the subscripts (i, j, k) refer to the grid indices. Note that B and E are offset by half-steps in both space and time, according to the Yee algorithm [Yee, 1966].

A.3 Collision Frequency

After the magnetic field is updated, currents are calculated using Equation (A.2); but before updating currents the electron-neutral collision frequency ν_e must be updated. The collision frequency ν_e depends on the neutral density (i.e., altitude) as well as the “effective” electric field that is modified by the static magnetic field \mathbf{B}_0 . First, the electric field is split into perpendicular and parallel components. The parallel

component is found from

$$E_{\parallel} = \vec{E}_m \cdot \frac{\mathbf{B}_0}{B_0} = E_{xm}B_{0x} + E_{ym}B_{0y} + E_{zm}B_{0z}$$

where B_{0x} , B_{0y} and B_{0z} are the unit vector components of \mathbf{B}_0 , and E_{xm} , E_{ym} , and E_{zm} are the spatial-averaged field values of the wave electric field \vec{E}_w , since E and B components are offset in the grid; and the perpendicular component follows from

$$E_{\perp}^2 = |E_w|^2 - E_{\parallel}^2$$

The “effective electric field” of the incident wave that is applied to these confined electrons can be approximated, in phasor form, by [*Gurevich, 1978*, p.75]:

$$E_{\text{eff}}^2 = E_{\parallel}^2 + (\omega^2 + \nu_c^2) \left[\frac{E_{\perp-}^2}{(\omega - \omega_b)^2 + \nu_c^2} + \frac{E_{\perp+}^2}{(\omega + \omega_b)^2 + \nu_c^2} \right] \quad (\text{A.10})$$

where E_{\parallel} is the component of \vec{E}_w parallel to B_0 , $E_{\perp-}$ and $E_{\perp+}$ are the perpendicular components of the electric field which rotate with and against the electron gyromotion, and ν_c is a kinetically-calculated effective collision frequency [*Glukhov and Inan, 1996*], given by

$$\nu_c = \frac{1}{2} \sqrt{|E_w|N}$$

where N is the neutral density in units of cm^{-3} . In the simulations described here, the frequency ω (≤ 100 kHz) is always much less than the gyrofrequency ω_b (~ 0.7 – 1.8 MHz at 100 km altitude, depending on latitude), so that Equation (A.10) reduces to

$$E_{\text{eff}}^2 = E_{\parallel}^2 + E_{\perp}^2 \frac{\nu_c^2}{\omega_b^2 + \nu_c^2} \quad (\text{A.11})$$

where ω_b is the magnitude of the electron gyrofrequency, $\omega_b = |q|B_0/m_e$. Note that this equation is no longer frequency-dependent. Note that this collision frequency ν_c is not the same as the electron-neutral collision frequency ν_e in Equation (A.2); it is a kinetically-calculated “effective” collision frequency used only in Equation (A.11) to find the effective electric field E_{eff} . The electron-neutral collision frequency ν_e is

now given by

$$\nu_e = \frac{q}{m_e \mu_e}$$

where the electron mobility μ_e is found from E_{eff} :

$$\mu_e = \frac{1}{N} \times 10^y \quad \text{where} \quad y = a_0 + a_1 \log \frac{E_{\text{eff}}}{N} + a_2 \left(\log \frac{E_{\text{eff}}}{N} \right)^2$$

and the constants are $a_0 = 50.97$, $a_1 = 3.026$, and $a_2 = 8.4733 \times 10^{-2}$. The electron mobility was put into this analytical form by *Pasko et al.* [1997] using the data tabulated in *Davies* [1983].

A.4 Current J Update Equations

Equation (A.2) is actually solved as a velocity equation by factoring out qN_e , noting that $\omega_p^2 = q_e^2 N_e / m_e \epsilon_0$ and $\omega_b = q_e \mathbf{B}_0 / m_e$:

$$\frac{\partial \vec{v}}{\partial t} + \nu_e \vec{v} = \frac{e}{m_e} \vec{E}_w - \frac{e}{m_e} \vec{v} \times \mathbf{B}_0 \quad (\text{A.12})$$

This equation is solved in three steps, as described by *Buneman* [1993]. The three-step method involves first solving for the first part of the right side of the equation (“acceleration”, the part controlled by the wave electric field \vec{E}_w) in a *half time step*; then solving the second part of the right side (“magnetic rotation”, the part controlled by \mathbf{B}_0); then finally adding the second *half time step* of acceleration. In *Buneman* [1993] the equations do not include collisions, so in the method used here, an Exponential Time Differencing is implemented as described by *Huang and Li* [2005].

First, Equation (A.12), without the last (rotation) term, is multiplied by $e^{\nu_e t}$ and

integrated from zero to $\Delta t/2$, using partial fractions:

$$\begin{aligned} \int_0^{\Delta t/2} e^{\nu_e t} \frac{\partial \vec{v}}{\partial t} \Delta t + \int_0^{\Delta t/2} e^{\nu_e t} \nu_e \vec{v} \Delta t &= \int_0^{\Delta t/2} e^{\nu_e t} \frac{e}{m_e} \vec{E}_w \Delta t \\ \vec{v} e^{\nu_e t} \Big|_0^{\Delta t/2} - \int_0^{\Delta t/2} e^{\nu_e t} \nu_e \vec{v} \Delta t + \int_0^{\Delta t/2} e^{\nu_e t} \nu_e \vec{v} \Delta t &= e^{\nu_e t} \frac{e}{\nu_e m_e} \vec{E}_w \Big|_0^{\Delta t/2} \\ \vec{v}_1 e^{\nu_e \Delta t/2} - \vec{v}_0 &= \frac{e}{\nu_e m_e} \vec{E}_w (e^{\nu_e \Delta t/2} - 1) \end{aligned}$$

where \vec{v}_0 is the velocity at time t , and \vec{v}_1 is the velocity at time $t + \Delta t/2$. Solving for \vec{v}_1 we find:

$$\vec{v}_1 = \vec{v}_0 e^{-\nu_e \Delta t/2} + \frac{e}{m_e} \vec{E}_w \frac{1 - e^{-\nu_e \Delta t/2}}{\nu_e}$$

In each of the three dimensions, these are discretized and solved in the code as follows:

$$\begin{aligned} v_{1x} \Big|_{i,j,k}^n &= v_{0x} \Big|_{i,j,k}^n e^{-\nu_e \Delta t/2} - \frac{|q|}{m_e} E_{xm}^n \frac{1 - e^{-\nu_e \Delta t/2}}{\nu_e} \\ v_{1y} \Big|_{i,j,k}^n &= v_{0y} \Big|_{i,j,k}^n e^{-\nu_e \Delta t/2} - \frac{|q|}{m_e} E_{ym}^n \frac{1 - e^{-\nu_e \Delta t/2}}{\nu_e} \\ v_{1z} \Big|_{i,j,k}^n &= v_{0z} \Big|_{i,j,k}^n e^{-\nu_e \Delta t/2} - \frac{|q|}{m_e} E_{zm}^n \frac{1 - e^{-\nu_e \Delta t/2}}{\nu_e} \end{aligned}$$

Next, the magnetic rotation term $\vec{v} \times \mathbf{B}_0$ in (A.12) is solved using the method described by [Buneman \[1993\]](#):

$$\vec{v}_3 = \vec{v}_1 + 2 \frac{\vec{v}_1 + \vec{v}_1 \times \vec{B}'_0}{1 + B_0'^2} \times \vec{B}'_0 \quad (\text{A.13})$$

Note that $\vec{B}'_0 = q\vec{B}\Delta t/2m_e$, and $\vec{B} = \mathbf{B}_0 + \vec{B}_w$ includes the wave magnetic field as well as the static Earth's magnetic field. In our case, the Earth's magnetic field dominates, so $\vec{B}'_0 = q\mathbf{B}_0\Delta t/2m_e$. The EMP code now splits this into two ‘‘halves’’ of magnetic rotation, the first half including only the fractional component above; The

analytical equation then looks like

$$\vec{v}_2 = 2 \frac{\vec{v}_1 + \vec{v}_1 \times \vec{B}'_0}{1 + B_0'^2}$$

and the component update equations are

$$\begin{aligned} v_{2x} &= (v_{1x} + v_{1y}B'_{z0} - v_{1z}B'_{y0}) \frac{2}{1 + B_0'^2} \\ v_{2y} &= (v_{1y} + v_{1z}B'_{x0} - v_{1x}B'_{z0}) \frac{2}{1 + B_0'^2} \\ v_{2z} &= (v_{1z} + v_{1x}B'_{y0} - v_{1y}B'_{x0}) \frac{2}{1 + B_0'^2} \end{aligned}$$

where we have dropped the n superscript and (i, j, k) subscripts for brevity. The EMP code now combines the second-half of the magnetic rotation with the second half of acceleration, but here we will do them separately to illustrate the process. The second half of magnetic rotation takes v_{2x} , v_{2y} , and v_{2z} from above and uses them to complete equation (A.13):

$$\vec{v}_3 = \vec{v}_1 + \vec{v}_2 \times \vec{B}'_0$$

In [Buneman \[1993\]](#), where collisions were not considered, \vec{v}_3 above is used in the second half of the acceleration, which looks exactly like the first half. Hence, the update equation should look the same using our exponential time stepping:

$$\vec{v}_{\text{final}} = \vec{v}_3 e^{-\nu_e \Delta t / 2} + \frac{|q|}{m_e} \vec{E}_w \frac{1 - e^{-\nu_e \Delta t / 2}}{\nu_e}$$

Plugging in \vec{v}_3 and swapping the order of terms, we have

$$\vec{v}_{\text{final}} = \frac{e}{m_e} \vec{E}_w \frac{1 - e^{-\nu_e \Delta t / 2}}{\nu_e} + \left(\vec{v}_1 + \vec{v}_2 \times \vec{B}'_0 \right) e^{-\nu_e \Delta t / 2}$$

The update equations are thus

$$\begin{aligned} v_{x,\text{final}} &= v_{x1} e^{-\nu_e \Delta t/2} - \frac{|q|}{m_e} E_{xm} \frac{1 - e^{-\nu_e \Delta t/2}}{\nu_e} + (v_{y2} B'_{z0} - v_{z2} B'_{y0}) e^{-\nu_e \Delta t/2} \\ v_{y,\text{final}} &= v_{y1} e^{-\nu_e \Delta t/2} - \frac{|q|}{m_e} E_{ym} \frac{1 - e^{-\nu_e \Delta t/2}}{\nu_e} + (v_{z2} B'_{x0} - v_{x2} B'_{z0}) e^{-\nu_e \Delta t/2} \\ v_{z,\text{final}} &= v_{z1} e^{-\nu_e \Delta t/2} - \frac{|q|}{m_e} E_{zm} \frac{1 - e^{-\nu_e \Delta t/2}}{\nu_e} + (v_{x2} B'_{y0} - v_{y2} B'_{x0}) e^{-\nu_e \Delta t/2} \end{aligned}$$

Before the electric fields can be updated as usual, the velocity components must be converted to currents via $\vec{J} = eN_e\vec{v}$:

$$\begin{aligned} J_x|_{i,j,k}^n &= \frac{q}{2} \left(N_e|_{i,j,k}^n v_{x,\text{final}}|_{i,j,k}^n + N_e|_{i+1,j,k}^n v_{x,\text{final}}|_{i+1,j,k}^n \right) \\ J_y|_{i,j,k}^n &= \frac{q}{2} \left(N_e|_{i,j,k}^n v_{y,\text{final}}|_{i,j,k}^n + N_e|_{i,j+1,k}^n v_{y,\text{final}}|_{i,j+1,k}^n \right) \\ J_z|_{i,j,k}^n &= \frac{q}{2} \left(N_e|_{i,j,k}^n v_{z,\text{final}}|_{i,j,k}^n + N_e|_{i,j,k+1}^n v_{z,\text{final}}|_{i,j,k+1}^n \right) \end{aligned}$$

Note the spatial averaging of both N_e and \vec{v} to find values at the corresponding grid locations of \vec{J} .

A.5 Ionization and Attachment

Electron density is modified via impact ionization as described by [Papadopoulos et al. \[1993\]](#). With $x = E_{\text{eff}}/E_k$, the ionization rate is given by

$$\nu_i = 7.6 \times 10^{13} N x^2 f(x) e^{-4.7(\frac{1}{x}-1)}$$

where

$$f(x) = \frac{2}{3} (1 + 6.3e^{-2.6/x})$$

The breakdown field E_k is given by

$$E_k = 32 \times 10^5 \frac{N}{N_0} \sqrt{1 + \frac{\omega^2}{(1.6 \times 10^{-13} N)^2}} \quad (\text{A.14})$$

with $N_0 = 2.688 \times 10^{25} \text{ m}^{-3}$ and N is specified in units of m^{-3} . Note the dependence of the breakdown field on frequency; for our EMP modeling, the number density N is about 10^{19} m^{-3} at 100 km altitude, and so the term under the square-root sign involving frequency ω can be ignored below about 500 kHz.

Dissociative attachment to molecular oxygen is calculated as described by [Davies \[1983\]](#). The attachment rate is given by [\[Pasko et al., 1997\]](#):

$$\nu_\alpha = \frac{N}{N_0} (a_0 + a_1 x' + a_2 x'^2)$$

with $N_0 = 2.688 \times 10^{25} \text{ m}^{-3}$, $a_0 = -2.41 \times 10^8$, $a_1 = 211.92$, and $a_2 = -3.545 \times 10^{-5}$. This equation is valid for large values of ν_α ; for smaller values, a logarithmic expression has been found to be a better fit [\[Pasko, 1996\]](#), mainly because the expression above gives negative values for small E-fields. In the EMP code, we simply set the coefficient to zero if the equation yields a negative number; this fits the logarithmic model fairly well.

The electron density is updated from time step n to time step $n + 1$ using the simple expression

$$N_e|_{i,j,k}^{n+1} = e^{(\nu_i - \nu_\alpha)\Delta t} N_e|_{i,j,k}^n$$

A.6 Electric field Update Equations

Finally, we do the full step in electric field, following Equation (3.6):

$$E_x|_{i+1/2,j,k}^{n+1} = E_x|_{i+1/2,j,k}^n + K_y \left(B_z|_{i+1/2,j+1/2,k}^{n+1/2} - B_z|_{i+1/2,j-1/2,k}^{n+1/2} \right) - K_z \left(B_y|_{i+1/2,j,k+1/2}^{n+1/2} - B_y|_{i+1/2,j,k-1/2}^{n+1/2} \right) - \Delta t \cdot J_x \quad (\text{A.15})$$

$$E_y|_{i,j+1/2,k}^{n+1} = E_y|_{i,j+1/2,k}^n + K_z \left(B_x|_{i,j+1/2,k+1/2}^{n+1/2} - B_x|_{i,j+1/2,k-1/2}^{n+1/2} \right) - K_x \left(B_z|_{i+1/2,j+1/2,k}^{n+1/2} - B_z|_{i-1/2,j+1/2,k}^{n+1/2} \right) - \Delta t \cdot J_y \quad (\text{A.16})$$

$$E_z|_{i,j,k+1/2}^{n+1} = E_z|_{i,j,k+1/2}^n + K_x \left(B_y|_{i+1/2,j,k+1/2}^{n+1/2} - B_y|_{i-1/2,j,k+1/2}^{n+1/2} \right) - K_y \left(B_x|_{i,j+1/2,k+1/2}^{n+1/2} - B_x|_{i,j-1/2,k+1/2}^{n+1/2} \right) - \Delta t \cdot J_z \quad (\text{A.17})$$

Bibliography

- Aleksandrov, N. L., A. E. Bazelyan, E. M. Bazelyan, and I. V. Kochetov (1995), Modeling of long streamers in atmospheric-pressure air, *Plasma Phys. Rep.*, 21(1), 60–80.
- Armstrong, W. C. (1983), Recent advances from studies of the Trimpi effect, *Antarc. J. of USA*, 18, 281–283.
- Balay, S., K. Buschelman, W. Gropp, D. Kaushik, M. Knepley, L. McInnes, B. Smith, and H. Zhang (2001), PETSc web page, *Tech. Rep.*, Available at: <http://www.mcs.anl.gov/petsc>.
- Balay, S., K. Buschelman, V. Eijkhout, W. Gropp, D. Kaushik, M. Knepley, L. McInnes, B. Smith, and H. Zhang (2004), PETSc Users Manual, anl-95/11–Revision 2.1.5., *Tech. Rep.*, Argonne, IL: Argonne National Laboratory.
- Barrington-Leigh, C. P. (2000), Fast photometric imaging of high altitude optical flashes above thunderstorms, Ph.D. Thesis, Stanford University.
- Barrington-Leigh, C. P., U. S. Inan, M. Stanley, and S. A. Cummer (1999), Sprites triggered by negative lightning discharges, *Geophys. Res. Lett.*, 26(24), 3605–3608.
- Barrington-Leigh, C. P., U. S. Inan, and M. Stanley (2001), Identification of sprite and elves with intensified video and broadband array photometry, *J. Geophys. Res.*, 106(A2), 1741–1750.
- Beasley, W. H., M. A. Uman, D. M. Jordan, and C. Ganesh (1983), Positive cloud to ground lightning return strokes, *J. Geophys. Res.*, 88, 8475–8482.

- Bell, T. F., S. C. Reising, and U. S. Inan (1998), Intense continuing currents following positive cloud-to-ground lightning associated with red sprites, *Geophys. Res. Lett.*, *25*(8), 1285–1288.
- Berenger, J. P. (1994), A perfectly matched layer for the absorption of electromagnetic waves, *J. Comput. Phys.*, *114*, 185–200.
- Berger, K., R. B. Anderson, and H. Kroninger (1975), Parameters of lightning flashes, *Electra*, *80*, 223–237.
- Bittencourt, J. A. (2003), *Fundamentals of Plasma Physics*, J. Bittencourt.
- Boeck, W. L., O. H. Vaughan, R. Blakeslee, B. Vonnegut, and M. Brook (1992), Lightning induced brightening in the airglow layer, *Geophys. Res. Lett.*, *19*, 99–102.
- Budden, K. G. (1961), *The Wave-guide Mode Theory of Wave Propagation*, Prentice-Hall.
- Buneman, O. (1993), *Computer Space Plasma Physics: Simulation techniques and Software*, Chap. 3: TRISTAN: The 3D electromagnetic particle code, pp. 67–84, Terra Scientific Publishing Co.
- Chen, A. B., C.-L. Kuo, Y.-J. Lee, H.-T. Su, R.-R. Hsu, J.-L. Chern, H. U. Frey, S. B. Mende, Y. Takahashi, H. Fukunishi, Y.-S. Chang, T.-Y. Liu, and L.-C. Lee (2008), Global distributions and occurrence rates of transient luminous events, *J. Geophys. Res.*, *113*, A08,306, doi:10.1029/2008JA013101.
- Chern, J. L., R. R. Hsu, H. T. Su, S. B. Mende, H. Fukunishi, Y. Takahashi, and L. C. Lee (2003), Global survey of upper atmospheric transient luminous events on the ROCSAT-2 satellite, *J. Atmos. and Solar Terr. Phys.*, *65*(5), 647–659.
- Chevalier, M. W., and U. S. Inan (2006), A technique for efficiently modeling long-path propagation for use in both FDFD and FDTD, *IEEE Ant. and Wireless Prop. Lett.*, *5*, 525–528.

- Chevalier, T. W., U. S. Inan, and T. F. Bell (2008), Terminal impedance and antenna current distribution of a VLF electric dipole in the inner magnetosphere, *IEEE Trans. on Ant. and Prop.*, *56*(8), 2454–2468.
- Cho, M., and M. Rycroft (1998), Computer simulation of the electric field structure and optical emission from cloud-top to the ionosphere, *Jour. Atmos. and Solar Terr. Phys.*, *60*, 871–888.
- Cho, M., and M. J. Rycroft (2001), Non-uniform ionisation of the upper atmosphere due to the electromagnetic pulse from a horizontal lightning discharge, *J. Atmos. and Solar Terr. Phys.*, *63*, 559–580.
- Christian, H. J., R. J. Blakeslee, D. J. Boccippio, W. L. Boeck, D. E. Buechler, K. T. Driscoll, S. J. Goodman, J. M. Hall, W. J. Koshak, D. M. Mach, and M. F. Stewart (2003), Global frequency and distribution of lightning as observed from space by the optical transient detector, *J. Geophys. Res.*, *108*, 4005, doi:10.1019/2002JD002347.
- Corcuff, Y. (1998), VLF signatures of ionospheric perturbations caused by lightning discharges in an underlying and moving thunderstorm, *Geophys. Res. Lett.*, *25*(13), 2385–2388.
- Crary, J. H. (1961), The effect of the earth-ionosphere waveguide on whistlers, Ph.D. Thesis, Stanford University.
- Cummer, S. A., and U. S. Inan (1997), Measurement of charge transfer in sprite-producing lightning using elf radio atmospherics, *Geophys. Res. Lett.*, *24*, 1731–1734.
- Cummer, S. A., and U. S. Inan (2000), Modeling ELF radio atmospheric propagation and extracting lightning currents from ELF observations, *Radio Sci.*, *35*(2), 385–394.
- Cummer, S. A., and W. A. Lyons (2005), Implications of lightning charge moment changes for sprite initiation, *J. Geophys. Res.*, *110*(A04304), doi:10.1029/2004JA010812.

- Cummer, S. A., N. Jaugey, J. Li, W. A. Lyons, T. E. Nelson, and E. A. Gerken (2006), Submillisecond imaging of sprite development and structure, *Geophys. Res. Lett.*, *33*, L04,104, doi:10.1029/2005GL024969.
- Davies, D. K. (1983), Measurements of swarm parameters in dry air, in *Theoretical Notes*, Westinghouse R&D Center.
- Davies, K. (1990), *Ionospheric Radio*, Peter Peregrinus.
- Dowden, R. L. (1996), Comment on “VLF signatures of ionospheric disturbances associated with sprites” by Inan et al., *Geophys. Res. Lett.*, *23*(23), 3421–3422.
- Dowden, R. L., and C. D. D. Adams (1988), Phase and amplitude perturbations on subionospheric signals explained in terms of echoes from lightning-induced electron precipitation ionization patches, *J. Geophys. Res.*, *93*, 11,543.
- Dowden, R. L., and C. D. D. Adams (1989), Phase and amplitude perturbations on the NWC signal at Dunedin from lightning-induced electron precipitation, *J. Geophys. Res.*, *94*, 497.
- Dowden, R. L., J. B. Brundell, W. A. Lyons, and T. E. Nelson (1996), Detection and location of red sprites by VLF scattering of subionospheric transmissions, *Geophys. Res. Lett.*, *23*(14), 1737–1740.
- Ferguson, J. A., and F. P. Snyder (1987), The segmented waveguide program for long wavelength propagation calculations, *Tech. Rep. 1071*, Naval Ocean Systems Center, San Diego, CA.
- Franz, R. C., R. J. Nemzek, and J. R. Winckler (1990), Television image of a large upward electrical discharge above a thunderstorm system, *Science*, *249*, 48–51.
- Fukunishi, H., Y. Takahashi, M. Kubota, K. Sakanoi, U. S. Inan, and W. A. Lyons (1996), Elves: Lightning-induced transient luminous events in the lower ionosphere, *Geophys. Res. Lett.*, *23*, 2157–2160, doi:10.1029/96GL01979.

- Gerken, E. A., and U. S. Inan (2004), Comparison of photometric measurements and charge moment estimations in two sprite-producing storms, *Geophys. Res. Lett.*, *31*(L03107), doi:10.1029/2003GL018751.
- Glukhov, V. S., and U. S. Inan (1996), Particle simulation of the time-dependent interaction with the ionosphere of rapidly varying lightning EMP, *Geophys. Res. Lett.*, *23*(16), 2193–2196.
- Gurevich, A. V. (1978), *Nonlinear Phenomena in the Ionosphere*, Springer-Verlag.
- Haldoupis, C., T. Neubert, U. S. Inan, A. Mika, T. H. Allin, and R. A. Marshall (2004), Subionospheric early VLF signal perturbations observed in one-to-one association with sprites, *J. Geophys. Res.*, *109*(A10303), doi:10.1029/2004JA010651.
- Haldoupis, C., R. J. Steiner, A. Mika, S. Shalimov, R. A. Marshall, U. S. Inan, T. Bosinger, and T. Neubert (2006), “Early/slow” events: A new category of VLF perturbations observed in relation with sprites, *J. Geophys. Res.*, *111*, A11,321, doi:10.1029/2006JA011960.
- Hardman, S. F., C. J. Rodger, R. L. Dowden, and J. B. Brundell (1998), Measurements of the VLF scattering pattern of the structured plasma of red sprites, *IEEE Trans. on Ant. and Prop.*, *40*, 29–38.
- Helliwell, R. A. (1965), *Whistlers and Related Ionospheric Phenomena*, Stanford University Press.
- Higdon, R. L. (1986), Absorbing boundary conditions for difference approximations to the multi-dimensional wave equation, *Math. of Comp.*, *47*, 437–459.
- Higdon, R. L. (1987), Numerical absorbing boundary conditions for the wave equation, *Math. of Comp.*, *49*, 65–90.
- Huang, S. J., and F. Li (2005), FDTD implementation for magnetoplasma medium using exponential time differencing, *IEEE Microwave and Wireless Components Letters*, *15*(3), 183–185, doi:10.1109/LMWC.2005.844220.

- Inan, U. S., and A. S. Inan (2000), *Electromagnetic Waves*, Prentice-Hall.
- Inan, U. S., and J. V. Rodriguez (1993), Lightning-induced effects on VLF/LF radio propagation, *AGARD Conference Proceedings 529, ELF/VLF/LF Radio Propagation and Systems Aspects*, pp. 9–1.
- Inan, U. S., D. C. Shafer, W. P. Yip, and R. E. Orville (1988), Subionospheric VLF signatures of nighttime D region perturbations in the vicinity of lightning discharges, *J. Geophys. Res.*, *93*(A10), 11,455–11,472.
- Inan, U. S., T. F. Bell, and J. V. Rodriguez (1991), Heating and ionization of the lower ionosphere by lightning, *Geophys. Res. Lett.*, *18*(4), 705–708.
- Inan, U. S., J. V. Rodriguez, and V. P. Idone (1993), VLF signatures of lightning-induced heating and ionization of the nighttime D-region, *Geophys. Res. Lett.*, *20*(21), 2355–2358.
- Inan, U. S., T. F. Bell, V. P. Pasko, D. D. Sentman, E. M. Wescott, and W. A. Lyons (1995), VLF signatures of ionospheric disturbances associated with sprites, *Geophys. Res. Lett.*, *22*(24), 3461–3464.
- Inan, U. S., T. F. Bell, and V. P. Pasko (1996a), Reply to Comment by R. L. Dowden et al. on “VLF signatures of ionospheric disturbances associated with sprites”, *Geophys. Res. Lett.*, *423*(23), 3423–3424.
- Inan, U. S., V. P. Pasko, and T. F. Bell (1996b), Sustained heating of the ionosphere above thunderstorms as evidenced in “Early/fast” VLF events, *Geophys. Res. Lett.*, *23*(10), 1067–1070.
- Inan, U. S., W. A. Sampson, and Y. N. Taranenko (1996c), Space-time structure of optical flashes and ionization changes produced by lightning-EMP, *Geophys. Res. Lett.*, *23*(2), 133–136.
- Inan, U. S., A. Slingeland, V. P. Pasko, and J. V. Rodriguez (1996d), VLF and LF signatures of mesospheric/lower ionospheric response to lightning discharges, *J. Geophys. Res.*, *101*(A3), 5219–5238.

- Inan, U. S., C. P. Barrington-Leigh, S. Hansen, V. S. Glukhov, T. F. Bell, and R. Rairden (1997), Rapid lateral expansion of optical luminosity in lightning-induced ionospheric flashes referred to as ‘elves’, *Geophys. Res. Lett.*, *24*(5), 583–586.
- Inan, U. S., M. Golkowski, M. K. Casey, R. C. Moore, W. Peter, P. Kulkarni, P. Kossey, and E. Kennedy (2007a), Subionospheric VLF observations of transmitter-induced precipitation of inner radiation belt electrons, *Geophys. Res. Lett.*, *34*, L02,106, doi:10.1029/2006GL028494.
- Inan, U. S., N. G. Lehtinen, R. C. Moore, K. Hurley, S. Boggs, D. M. Smith, and G. J. Fishman (2007b), Massive disturbance of the daytime lower ionosphere by the giant gamma-ray flare from magnetar SGR 1806-20, *Geophys. Res. Lett.*, *34*, L08,103, doi:10.1029/2006GL029145.
- Johnson, M. P. (2000), VLF imaging of lightning-induced ionosphere disturbances, Ph.D. Thesis, Stanford University.
- Johnson, M. P., and U. S. Inan (2000), Spheric clusters associated with Early/fast VLF events, *Geophys. Res. Lett.*, *27*(9), 1391–1394.
- Johnson, M. P., U. S. Inan, S. J. Lev-Tov, and T. F. Bell (1999), Scattering pattern of lightning-induced ionospheric disturbances associated with Early/fast VLF events, *Geophys. Res. Lett.*, *26*(15), 2363–2366.
- Kitagawa, N., M. Brook, and E. J. Workman (1962), Continuing currents in cloud-to-ground lightning discharges, *J. Geophys. Res.*, *67*, 637–647.
- Krehbiel, P. R., J. A. Riouset, V. P. Pasko, R. J. Thomas, W. Rison, M. Stanley, and H. E. Edens (2008), Upward electrical discharges from thunderstorms, *Nature Geoscience*, *1*, 233–237.
- Kuo, C.-L., A. B. Chen, Y. J. Lee, L. Y. Tsai, R. K. Chou, R. R. Hsu, H. T. Su, L. C. Lee, S. A. Cummer, H. U. Frey, S. B. Mende, Y. Takahashi, and H. Fukushima (2007), Modeling elves observed by FORMOSAT-2 satellite, *J. Geophys. Res.*, *112*(A11312), doi:10.1029/2007JA012407.

- Lang, T., L. J. Miller, M. Weisman, S. A. Rutledge, L. J. Barker III, V. N. Bringi, V. Chandrasekar, A. Detwiler, N. Doesken, J. Helsdon, C. Knight, P. Krehbiel, W. A. Lyons, D. MacGorman, E. Rasmussen, W. Rison, W. D. Rust, and R. J. Thomas (2004), The severe thunderstorm electrification and precipitation study (steps), in *Bull. Amer. Meteor. Soc.*, vol. 85, pp. 1107–1112.
- Lehtinen, N. G., and U. S. Inan (2007), Possible persistent ionization caused by giant blue jets, *Geophys. Res. Lett.*, *34*, L08,804, doi:10.1029/2006GL029051.
- Lehtinen, N. G., and U. S. Inan (2009), Full-wave modeling of transionospheric propagation of VLF waves, *Geophys. Res. Lett.*, *36*, L03,104, doi:10.1029/2008GL036535.
- Lyons, W. A. (1994), Characteristics of luminous structures in the stratosphere above thunderstorms as imaged by low-light video, *Geophys. Res. Lett.*, *21*, 875–878.
- Lyons, W. A. (1995), The relationship of large luminous stratospheric events to the anvil structure and cloud-to-ground discharges of their parent mesoscale convective system, in *Preprints, Conf. on Cloud Physics*, pp. 541–546, Amer. Meteor. Soc.
- Lyons, W. A. (1996), Sprite observations above the U.S. high plains in relation to their parent thunderstorm systems, *J. Geophys. Res.*, *101*, 29,641–29,652.
- Lyons, W. A., M. Uliasz, and T. E. Nelson (1998), Large peak current cloud-to-ground lightning flashes during the summer months in the contiguous United States, *Mon. Wea. Rev.*, *126*, 2217–2233.
- Lyons, W. A., T. E. Nelson, E. R. Williams, S. A. Cummer, and M. A. Stanley (2003), Characteristics of sprite-producing positive cloud-to-ground lightning during the 19 July steps mesoscale convective systems, *Mon. Wea. Rev.*, *131*, 2417–2427.
- Marshall, R. A., and U. S. Inan (2006), High-speed measurements of small-scale features in sprites: sizes and lifetimes, *Radio Sci.*, *41* (RS6S43), doi:10.1029/2005RS003353.

- Marshall, R. A., U. S. Inan, and W. A. Lyons (2006), On the association of Early/fast very low frequency perturbations with sprites and rare examples of VLF backscatter, *Jour. Geophys. Res.*, *111*, D19108, doi:10.1029/2006JD007219.
- Marshall, R. A., U. S. Inan, and W. A. Lyons (2007), Very low frequency sferic bursts, sprites, and their association with lightning activity, *J. Geophys. Res.*, *112*, D22105, doi:10.1029/2007JD008857.
- Marshall, R. A., U. S. Inan, and T. W. Chevalier (2008a), Early VLF perturbations caused by lightning EMP-driven dissociative attachment, *Geophys. Res. Lett.*, *35*, L21807, doi:10.1029/2008GL035358.
- Marshall, R. A., R. T. Newsome, and U. S. Inan (2008b), Fast photometric imaging using orthogonal linear arrays, *IEEE Trans. on Geosci. and Remote Sensing*, *46*, 11, pp. 3885-3893.
- Mazur, V., E. Williams, R. Boldi, L. Maier, and D. E. Proctor (1997), Initial comparison of lightning mapping with operational time-of-arrival and interferometric systems, *Jour. Geophys. Res.*, *102*(D10), 11,071–11,085.
- Mazur, V., X. M. Shao, and P. R. Krehbiel (1998), “Spider” lightning in intracloud and positive cloud-to-ground flashes, *J. Geophys. Res.*, *103*(D16), 19,811–19,822.
- McHarg, M. G., H. C. Stenbaek-Nielsen, and T. Kammae (2007), Observations of streamer formation in sprites, *Geophys. Res. Lett.*, *34*, L06,804, doi:10.1029/2007GL027854.
- Mende, S. B., H. U. Frey, R. R. Hsu, H. T. Su, A. B. Chen, L. C. Lee, D. D. Sentman, Y. Takahashi, and H. Fukunishi (2005a), D region ionization by lightning-induced electromagnetic pulses, *Jour. Geophys. Res.*, *110*, A11,312, doi:10.1019/2005JA011064.
- Mende, S. B., H. U. Frey, H.-T. Su, R.-R. Hsu, A. B. Chen, H. Fukunishi, Y. Takahashi, T. Adachi, and L.-C. Lee (2005b), Global TLE observations with ISUAL, Presented at *Berkeley Special Seminar, Berkeley, CA*.

- Mika, A. (2007), Very low frequency EM wave studies of transient luminous events in the lower ionosphere, Ph.D. Thesis, University of Crete.
- Mika, A., C. Haldoupis, R. A. Marshall, T. Neubert, and U. S. Inan (2005), Subionospheric VLF signatures and their association with sprite observed during Eurosprite-2003, *J. Atmos. and Solar-Terr. Phys.*, *67*, 1580–1597.
- Mika, A., C. Haldoupis, T. Neubert, R. R. Su, H. T. Hsu, R. J. Steiner, and R. A. Marshall (2006), Early VLF perturbations observed in association with elves, *Ann. Geophys.*, *24*, 2179–2189.
- Moore, R. C., C. P. Barrington-Leigh, U. S. Inan, and T. F. Bell (2003), Early/fast VLF events produced by electron density changes associated with sprite halos, *J. Geophys. Res.*, *108*(A10), doi:10.1029/2002JA009816.
- Morgan, W. L., and B. M. Penetrante (1990), ELENDF: A time-dependent boltzmann solver for partially ionized plasmas, *Comp. Phys. Comm.*, *58*(1-2), 127–152.
- Moss, G. D., V. P. Pasko, N. Liu, and G. Veronis (2006), Monte Carlo model for analysis of thermal runaway electrons in streamer tips in transient luminous events and streamer zones of lightning leaders, *J. Geophys. Res.*, *111*(A02307), doi:10.1029/2005JA011350.
- Nagano, I., S. Yagitani, K. Miyamura, and S. Makino (2003), Full-wave analysis of elves created by lightning-generated electromagnetic pulses, *J. Atmos. Solar Terr. Phys.*, *65*(5), 615–625.
- Naidis, G. V. (2005), Dynamics of streamer breakdown of short non-uniform air gaps, *J. Phys. D: Appl. Phys.*, *38*, 3889–3893, doi:10.1088/0022-3727/38/21/009.
- Neubert, T., T. H. Allin, H. Stenbaek-Nielsen, and E. Blanc (2001), Sprites over Europe, *Geophys. Res. Lett.*, *28*(18), 3585–3588.
- Neubert, T., T. H. Allin, E. Blanc, T. Farges, C. Haldoupis, A. Mika, S. Soula, L. Knutsson, O. van der Velde, R. A. Marshall, U. Inan, G. Satori, J. Bor,

- A. Hughes, A. Collier, S. Laursen, and I. L. Rasmussen (2005), Co-ordinated observations of transient luminous events during the Eurosprite-2003 campaign, *J. Atmos. and Solar-Terr. Phys.*, *67*, 807–820, doi:10.1016/j.jastp.2005.02.004.
- Neubert, T., M. Rycroft, T. Farges, E. Blanc, O. Chanrion, E. Arnone, A. Odzimek, N. Arnold, C.-F. Enell, E. Turunen, T. Bosinger, A. Mika, C. Haldoupis, R. J. Steiner, O. van der Velde, S. Soula, P. Berg, F. Boberg, P. Thejll, B. Christiansen, M. Ignaccolo, M. Fullekrug, P. T. Verronen, J. Montanya, and N. Crosby (2008), Recent results from studies of electric discharges in the mesosphere, *Surv. Geophys.*, *29*, 71–137.
- Noble, C. M. M., W. H. Beasley, S. E. Postawko, and T. E. L. Light (2004), Coincident observations of lightning by the FORTE photodiode detector, the New Mexico Tech lightning mapping array and the NLDN during STEPS, *Geophys. Res. Lett.*, *31*, L07,106, doi:10.1029/2003GL018989.
- Ohkubo, A., H. Fukunishi, Y. Takahashi, and T. Adachi (2005), VLF/ELF sferic evidence for in-cloud discharge activity producing sprites, *Geophys. Res. Lett.*, *32*, L04,812.
- Orville, R. E. (1991), Calibration of a magnetic direction finding network using measured triggered lightning return stroke peak currents, *J. Geophys. Res.*, *96*, 17,135.
- Papadopoulos, D., G. Milikh, A. Gurevich, A. Drobot, and R. Shanny (1993), Ionization rates for atmospheric and ionospheric breakdown, *J. Geophys. Res.*, *98*(A10), 17,593–17,596.
- Pappert, R. A., and F. P. Snyder (1972), Some results of a mode-conversion program for VLF, *Radio Sci.*, *7*, 913.
- Pasko, V. P. (1996), Dynamic coupling of quasi-electrostatic thundercloud fields to the mesosphere and lower ionosphere: sprites and jets, Ph.D. Thesis, Stanford University.

- Pasko, V. P. (2008), Blue jets and gigantic jets: transient luminous events between thunderstorm tops and the lower ionosphere, *Plasma Phys. Control. Fusion*, *50*, 124,050, doi:10.1088/0741-3335/50/12/124050.
- Pasko, V. P., and U. S. Inan (1994), Recovery signatures of lightning-associated VLF perturbations as a measure of the lower ionosphere, *J. Geophys. Res.*, *99*(A9), 17,523–17,537.
- Pasko, V. P., U. S. Inan, Y. N. Taranenکو, and T. F. Bell (1995), Heating, ionization and upward discharges in the mesosphere due to intense quasi-electrostatic thundercloud fields, *Geophys. Res. Lett.*, *22*(4), 363–368.
- Pasko, V. P., U. S. Inan, T. F. Bell, and Y. N. Taranenکو (1997), Sprites produced by quasi-electrostatic heating and ionization in the lower ionosphere, *J. Geophys. Res.*, *102*(A3), 4529–4561.
- Pasko, V. P., U. S. Inan, and T. F. Bell (1998), Ionospheric effects due to electrostatic thundercloud fields, *J. Atmos. and Solar-Terr. Phys.*, *60*, 863–870.
- Pasko, V. P., U. S. Inan, and T. F. Bell (2001), Mesosphere-troposphere coupling due to sprites, *Geophys. Res. Lett.*, *28*(19), 3821–3824.
- Pasko, V. P., M. A. Stanley, J. D. Mathews, U. S. Inan, and T. G. Wood (2002), Electrical discharge from a thundercloud top to the lower ionosphere, *Nature*, *416*, 152–154.
- Peter, W. B. (2007), Quantitative measurement of lightning-induced electron precipitation using VLF remote sensing, Ph.D. Thesis, Stanford University.
- Peter, W. B., and U. S. Inan (2005), Electron precipitation events driven by lightning in hurricanes, *J. Geophys. Res.*, *110*, A05,305, doi:doi:10.1029/2004JA010899.
- Peter, W. B., and U. S. Inan (2007), A quantitative comparison of lightning-induced electron precipitation and VLF signal perturbations, *J. Geophys. Res.*, *112*, A12,212, doi:10.1029/2006JA012165.

- Peter, W. B., M. W. Chevalier, and U. S. Inan (2006), Perturbations of mid-latitude subionospheric VLF signals associated with lower ionospheric disturbances during major geomagnetic storms, *J. Geophys. Res.*, *111*, A03,301, doi:doi:10.1029/2005JA011346.
- Poulsen, W. L., T. F. Bell, and U. S. Inan (1990), Three-dimensional modeling of subionospheric VLF propagation in the presence of localized D region perturbations associated with lightning, *J. Geophys. Res.*, *95*(A3), 2355–2366.
- Poulsen, W. L., T. F. Bell, and U. S. Inan (1993a), The scattering of VLF waves by localized ionospheric disturbances produced by lightning-induced electron precipitation, *J. Geophys. Res.*, *98*(A9), 15,553–15,559.
- Poulsen, W. L., U. S. Inan, and T. F. Bell (1993b), A multiple-mode three-dimensional model of VLF propagation in the earth-ionosphere waveguide in the presence of localized D region disturbances, *J. Geophys. Res.*, *98*(A2), 1705–1717.
- Proctor, D. E. (1997), Lightning flashes with high origins, *J. Geophys. Res.*, *102*, 1693–1706.
- Proctor, D. E., R. Uytendogaardt, and B. M. Meredith (1988), VHF radio pictures of lightning flashes to ground, *Jour. Geophys. Res.*, *93*(D10), 12,683–12,727.
- Raizer, Y. P. (1991), *Gas Discharge Physics*, Springer-Verlag.
- Rakov, V. A., and M. A. Uman (1990), Long continuing current in negative lightning ground flashes, *J. Geophys. Res.*, *95*, 5455–5470.
- Rakov, V. A., and M. A. Uman (2003), *Lightning: Physics and Effects*, Cambridge University Press.
- Ratcliffe, J. A. (1959), *The Magnetio-Ionic Theory and its Applications to the Ionosphere*, Cambridge University Press.
- Reising, S. C., U. S. Inan, and T. F. Bell (1996), Evidence for continuing current in sprite-producing cloud-to-ground lightning, *Geophys. Res. Lett.*, *23*(24), 3639–3642.

- Rodger, C. J., and D. Nunn (1999), VLF scattering from red sprites: Application of numerical modeling, *Radio Sci.*, *34*(4), 923–932.
- Rodger, C. J., J. R. Wait, and R. L. Dowden (1998), Scattering of VLF from an experimentally described sprite, *J. Atmos. and Solar-Terr. Phys.*, *60*, 765–769.
- Rodger, C. J., N. R. Thomson, and J. R. Wait (1999), VLF scattering from red sprites: Vertical columns of ionization in the earth-ionosphere waveguide, *Radio Sci.*, *34*(4), 913–921.
- Rowland, H., R. Fernsler, J. Huba, and P. Bernhardt (1995), Lightning driven EMP in the upper atmosphere, *Geophys. Res. Lett.*, *22*, 361–364.
- Rowland, H. L., R. F. Fernsler, and P. A. Bernhardt (1996), Breakdown of the neutral atmosphere in the D region due to lightning driven electromagnetic pulses, *J. Geophys. Res.*, *101*(A4), 7935–7945.
- Rust, W. D., D. MacGorman, and R. T. Arnold (1981), Positive cloud to ground lightning flashes in severe storms, *Geophys. Res. Lett.*, *8*, 791–794.
- Rust, W. D., D. R. MacGorman, and W. L. Taylor (1985), Photographic verification of continuing current in positive cloud-to-ground flashes, *J. Geophys. Res.*, *90*, 6144–6146.
- Rycroft, M. J., R. G. Harrison, K. A. Nicoll, and E. A. Mareev (2008), An overview of Earth’s global electric circuit and atmospheric conductivity, *Space Sci. Rev.*, *137*(1), 83–105.
- São Sabbas, F. T., D. D. Sentman, E. M. Wescott, O. Pinto Jr., O. Mendes Jr., and M. J. Taylor (2003), Statistical analysis of space-time relationships between sprites and lightning, *Jour. Atmos. and Solar Terr. Phys.*, *65*, 525–535, doi:10.1016/S1364-6826(02)00326-7.
- Sentman, D. D., E. M. Wescott, D. L. Osborne, D. L. Hampton, and M. J. Heavner (1995), Preliminary results from the Sprites94 aircraft campaign: 1. Red sprites, *Geophys. Res. Lett.*, *22*(10), 1205–1208.

- Sentman, D. D., H. C. Stenbaek-Nielsen, M. G. McHarg, and J. S. Morrill (2008), Plasma chemistry of sprite streamers, *J. Geophys. Res.*, *113*, D11,112, doi:10.1029/2007JD008941.
- Shao, X. M., and P. R. Krehbiel (1996), The spatial and temporal development of intracloud lightning, *J. Geophys. Res.*, *101*(D21), 26,641–26,668.
- Sipler, D. P., and M. A. Biondi (1972), Measurements of O(¹D) quenching rates in the F region, *J. Geophys. Res.*, *77*, 6202.
- Smith, D. A., X. M. Shao, D. N. Holden, C. T. Rhodes, M. Brook, P. R. Krehbiel, M. Stanley, W. Rison, and R. J. Thomas (1999), A distinct class of isolated intracloud lightning discharges and their associated radio emissions, *J. Geophys. Res.*, *104*, 4189–4212.
- Smith, R. L., and J. J. Angerami (1968), Magnetospheric properties deduced fromOGO 1 observations of ducted and nonducted whistlers, *J. Geophys. Res.*, *73*(1), 1–20.
- Stanley, M., P. Krehbiel, M. Brook, C. Moore, W. Rison, and B. Abrahams (1999), High speed video of initial sprite development, *Geophys. Res. Lett.*, *26*(20), 3201–3204.
- Stanley, M. A. (2000), Sprites and their parent discharges, Ph.D. Thesis, New Mexico Institute of Mining and Technology.
- Su, H. T., A. B. Hsu, R. R. and Chen, Y. C. Wang, W. S. Hsiao, W. C. Lai, L. C. Lee, M. Sato, and H. Fukunishi (2003), Gigantic jets between a thundercloud and the ionosphere, *Nature*, *423*, 974–976.
- Taflove, A., and S. C. Hagness (2005), *Computational Electrodynamics: The Finite-Difference Time-Domain Method, Third Edition*, Artech House.
- Taranenko, Y. N. (1993), Interaction with the lower ionosphere of electromagnetic pulses from lightning: Heating, attachment, ionization, and optical emissions, Ph.D. Thesis, Stanford University.

- Taranenko, Y. N., U. S. Inan, and T. F. Bell (1993a), The interaction with the lower ionosphere of electromagnetic pulses from lightning: heating, attachment, and ionization, *Geophys. Res. Lett.*, *20*(15), 1539–1542.
- Taranenko, Y. N., U. S. Inan, and T. F. Bell (1993b), The interaction with the lower ionosphere of electromagnetic pulses from lightning: excitation of optical emissions, *Geophys. Res. Lett.*, *20*(23), 2675–2678.
- Thomas, R. J., P. R. Krehbiel, W. Rison, T. Hamlin, D. J. Boccippio, S. J. Goodman, and H. J. Christian (2000), Comparison of ground-based 3-dimensional lightning mapping observations with satellite-based LIS observations in Oklahoma, *Geophys. Res. Lett.*, *27*(12), 1703–1706.
- Thomas, R. J., P. R. Krehbiel, W. Rison, S. J. Hunyady, W. P. Winn, T. Hamlin, and J. Harlin (2004), Accuracy of the lightning mapping array, *J. Geophys. Res.*, *109*, D14,207, doi:10.1029/2004JD004549.
- Tolstoy, A. (1983), The influence of localized precipitation-induced D region ionization enhancements on subionospheric VLF propagation, Ph.D. Thesis, University of Maryland, College Park.
- Tolstoy, A., T. J. Rosenberg, U. S. Inan, and D. L. Carpenter (1986), Model predictions of subionospheric VLF signal perturbations resulting from localized, electron precipitation-induced ionization enhancement regions, *J. Geophys. Res.*, *91*, 13,473.
- Uman, M. A., and D. K. McLain (1970), Lightning return stroke current from magnetic and radiation field measurements, *J. Geophys. Res.*, *75*, 5143–5147.
- Umashankar, K., and A. Taflove (1982), A novel method to analyze electromagnetic scattering of complex objects, *IEEE Trans. Elec. Compat.*, *24*(4), 397–405.
- Valdivia, J. A., G. Milikh, and D. Papadopoulos (1997), Red sprites: Lightning as a fractal antenna, *Geophys. Res. Lett.*, *24*, 3169.

- van der Velde, O. A., A. Mika, S. Soula, C. Haldoupis, T. Neubert, and U. S. Inan (2006), Observations of the relationship between sprite morphology and in-cloud lightning processes, *J. Geophys. Res.*, *111*, D15,203, doi:10.1029/2005JD006879.
- Veronis, G., V. P. Pasko, and U. S. Inan (1999), Characteristics of mesospheric optical emissions produce by lightning discharges, *J. Geophys. Res.*, *104*(A6), 12,645–12,656.
- Voss, H. D., W. L. Imhof, M. Walt, J. Mobilia, E. E. Gaines, J. B. Reagan, and U. S. Inan (1984), Lightning induced electron precipitation, *Nature*, *312*, 740–742.
- Voss, H. D., M. Walt, W. L. Imhof, J. Mobilia, and U. S. Inan (1998), Satellite observations of lightning-induced electron precipitation, *J. Geophys. Res.*, *103*, 11,725–11,744.
- Wait, J. R. (1962), An analysis of VLF mode propagation for a variable ionosphere height, *J. Res. Natl. Bur. Stand.*, *66*, 453.
- Wescott, E. M., D. Sentman, D. Osborne, D. Hampton, and M. Heavner (1995), Preliminary results from the Sprites94 aircraft campaign: 2. Blue jets, *Geophys. Res. Lett.*, *22*(10), 1209–1212.
- Williams, E. R. (1998), The positive charge reservoir for sprite-producing lightning, *Jour. Atmos. and Solar Terr. Phys.*, *60*, 689–692.
- Yair, Y., C. Price, P. Israelevich, A. Devir, M. Moalem, B. Ziv, Z. Levin, and J. Joseph (2003), Sprites, elves and other transient luminous events (TLEs) observed from the space shuttle Columbia during the Mediterranean Israeli Dust Experiment, in *Proceedings of the IUGG meeting, Sapporo, Japan*, vol. 2, p. 195.
- Yair, Y., P. Israelevich, A. Devir, M. Meir, C. Price, J. Joseph, Z. Levin, B. Ziv, A. Sternlieb, and A. Teller (2004), New observations of sprites from the space shuttle, *J. Geophys. Res.*, *109*(D15201), doi:10.1029/2003JD004497.

- Yee, K. (1966), Numerical solution of initial boundary value problems involving Maxwell's Equations in isotropic media, *IEEE Trans. on Ant. and Prop.*, 14(3), 302–207.